https://doi.org/10.15388/vu.thesis.678
https://orcid.org/0000-0002-4543-721X

VILNIUS UNIVERSITY

Nikolajus Kozulinas

Application of Navier–Stokes Equations in Hemodynamics

DOCTORAL DISSERTATION

Natural Sciences,
Mathematics (N 001)

VILNIUS 2024

This dissertation was written between 2019 and 2023 at Vilnius university. The research was supported by the project "Multiscale Mathematical and Computer Modeling for Flows in Networks: Application to Treatment of Cardiovascular Diseases" (No. 09.3.3-LMT-K-712-17-0003)

Academic supervisor:
Prof. Habil. Dr. Konstantinas Pileckas (Vilnius University, Natural Sciences, Mathematics - N 001).
Academic consultant:
Assoc. Prof. Dr. Kristina Kaulakytė (Vilnius University, Natural Sciences, Mathematics - N 001).

This doctoral dissertation will be defended in a public meeting of the Dissertation Defence Panels (Vilnius University).

Dissertation Defence Panel:

Chairman - Prof. Dr. Artūras Štikonas (Vilnius University, Natural Sciences, Mathematics - N 001).
Members:
Prof. Habil. Dr. Raimondas Čiegis (Vilnius Tech, Natural Sciences, Mathematics - N 001),
Prof. Dr. Pranas Katauskis (Vilnius University, Natural Sciences, Mathematics - N 001),
Prof. Habil. Dr. Antanas Laurinčikas (Vilnius University, Natural Sciences, Mathematics - N 001).
Prof. Dr. Igor Pažanin (University of Zagreb, Croatia, Natural Sciences, Mathematics - N 001).

The dissertation shall be defended at a public meeting of the Dissertation Defence Panel at 2 p.m. on the 22nd of November 2024 in Room 201 of the Faculty of Mathematics and Informatics, Vilnius University.
Address: Naugarduko st. 24, Vilnius, Lithuania.
Tel.: +370 5 219 3050; e-mail: mif@mif.vu.lt
The text of this dissertation can be accessed at the Library of Vilnius University, as well as on the website of Vilnius University:
www.vu.lt/lt/naujienos/ivykiu-kalendorius.

https://doi.org/10.15388/vu.thesis.678
https://orcid.org/0000-0002-4543-721X

VILNIAUS UNIVERSITETAS

Nikolajus Kozulinas

Navjė ir Stokso lygčių taikymai hemodinamikoje

DAKTARO DISERTACIJA

Gamtos mokslai,
matematika (N 001)

VILNIUS 2024

Disertacija rengta 2019–2023 metais Vilniaus universitete. Moksliniai tyrimai buvo remiami iš projekto „Daugiaskalis matematinis ir kompiuterinis srautų modeliavimas tinkluose: taikymai širdies ir kraujagyslių ligų gydymui“ (Nr. 09.3.3-LMT-K-712-17-0003)

Mokslinis vadovas:
prof. habil. dr. Konstantinas Pileckas (Vilniaus universitetas, gamtos mokslai, matematika - N 001).
Mokslinė konsultantė:
doc. dr. Kristina Kaulakytė (Vilniaus universitetas, gamtos mokslai, matematika - N 001).

Gynimo taryba:
Pirmininkas - Prof. dr. Artūras Štikonas (Vilniaus universitetas, gamtos mokslai, matematika N001);
Nariai:
Prof. habil. dr. Raimondas Čiegis (Vilnius Tech, gamtos mokslai, matematika - N 001);
Prof. dr. Pranas Katauskis (Vilniaus universitetas, gamtos mokslai, matematika - N 001);
Prof. habil. dr. Antanas Laurinčikas (Vilniaus universitetas, gamtos mokslai, matematika - N 001);
Prof. dr. Igor Pažanin (Zagrebo Universitetas, Kroatija, gamtos mokslai, matematika - N 001).

Disertacija ginama viešame Gynimo tarybos posėdyje 2024 m. lapkričio mėn. 22 d. 14 val. Vilniaus universiteto Matematikos ir informatikos fakulteto 201 auditorijoje. Adresas: Naugarduko g. 24, Vilnius, Lietuva, tel. +370 5 219 3050; el. paštas mif@mif.vu.lt.
Disetraciją galima peržiūrėti Vilniaus universiteto bibliotekoje ir VU interneto svetainėje adresu:
www.vu.lt/lt/naujienos/ivykiu-kalendorius

Contents

Introduction

The Navier–Stokes equations, named in honor of Claude-Louis Navier (1785–1836) and George Gabriel Stokes (1819–1903), were derived in the early 19^{th} century. Navier initially presented an original but not well-grounded justification in 1822. Subsequently, the equations underwent rediscovery by various mathematicians: Augustin-Louis Cauchy in 1823, Simeon Denis Poisson in 1829, Adhemar Jean Claude Barre de Saint-Venant in 1837, and finally Stokes in 1845 (see [20]). These equations represent a set of partial differential equations widely used in fluid mechanics to describe the dynamics of incompressible viscous fluids, including water, oil, and blood among others. The Navier–Stokes equations have the following form:

$$\begin{cases} \rho \mathbf{u}_t - \mu \Delta \mathbf{u} + \rho(\mathbf{u}\cdot\nabla)\mathbf{u} + \nabla \tilde{p} &= \rho \mathbf{f}, \\ \text{div } \mathbf{u} &= 0, \end{cases}$$

where $\mathbf{u} = \mathbf{u}(x,t) = (u_1(x,t), \ldots, u_n(x,t))$ and $\tilde{p} = \tilde{p}(x,t)$ are the unknown velocity and pressure, respectively, $\mathbf{f} = \mathbf{f}(x,t) = (f_1(x,t), \ldots, f_n(x,t))$ is external force vector, $x = (x_1, ..., x_n)$ is a space variable, t is time variable, ρ is a constant density of the fluid, μ is a constant dynamic viscosity of a fluid.

Within this thesis we consider in the domain Ω the time-periodic Navier–Stokes problem expressed in non-dimensional form:

$$\begin{cases} \mathbf{u}_t - \nu \Delta \mathbf{u} + (\mathbf{u}\cdot\nabla)\mathbf{u} + \nabla p &= \mathbf{f}, \\ \text{div } \mathbf{u} &= 0, \\ \mathbf{u}|_{\partial\Omega} &= 0, \\ \mathbf{u}(x,0) &= \mathbf{u}(x,T), \quad 0 < T < \infty, \end{cases}$$

where $p = \frac{\tilde{p}}{\rho}$ and $\nu = \frac{\mu}{\rho}$ is the constant kinematic viscosity of the fluid obtained after we divide the Navier–Stokes equations in general case by ρ.

In addition to the theoretical significance of the Navier–Stokes equations, we can apply them in different practical problems. These equations serve

as the foundation for modeling diverse engineering and biological systems that involve fluid dynamics. Given our focus on the application of Navier–Stokes equations in medicine, particularly in the modeling of blood circulation systems and cardiac dynamics, we concentrate our interest in the development of simplified theoretical models. These models aim to characterize flow within thin infinite cylinders, offering a framework for simulating blood flow in small and ultra-small vessels. Furthermore, these models serve as a stepping stone for the representation of more complicated systems, such as the human heart, allowing us to advance our understanding of blood circulation in both theoretical and practical contexts.

It is well known, that full 3D computations of the blood circulatory system are presently time-consuming and realizable only for limited segments, so a modern approach involves the creation of hybrid-dimensional models. These models merge 1D reductions in regular zones, typically modelled in straight vessels, with 3D analyses in small areas showing a singular behavior. This method, rooted in the asymptotic partial decomposition of a domain, was initially proposed by G. Panasenko and further advanced in subsequent works such as [67], [59], [69], [70], and [71]. The adoption of these hybrid-dimensional models results in a substantial reduction in computational demands.

Of particular significance within previously mentioned models are the 1D Poiseuille-type flows in straight vessels. Note, that the steady-state Poiseuille flow in an infinite straight pipe

$$\Pi = \{x = (x', x_n) \in \mathbb{R}^n : \, x' \in \sigma \subset \mathbb{R}^{n-1}, \, -\infty < x_n < \infty, n = 2, 3\}$$

of a constant cross section σ was described by Jean Louis Poiseuille in 1841 (see [72]). Poiseuille flows are important in the study of fluid motion in different networks of pipes, where these flows can be attained at very large distances (see [8]). In order to compute the blood flow velocity in the blood vessels considered as cylinders, it becomes necessary to prescribe a flow rate (flux) condition. Since in such case one usually does not have data defined by smooth functions, it is important to study nonstationary Poiseuille-type solutions assuming minimal regularity of data. Within the scope of this thesis we prove the existence and the uniqueness of the solution of time-periodic Navier–Stokes equations under minimally regular flow rate.

Moreover, the Navier–Stokes equations provide a framework for modeling fluid motion in domains featuring moving walls. An approach being used to describe this concept is Fluid-Structure Interaction (FSI), which involves the interaction between an elastic and movable structure and the fluid flow within or surrounding it. The role of FSI is particularly significant in accurately modeling blood flow within arteries considered as cylinders. The corresponding mathematical model is represented by the FSI problem, coupling two media with different, often high contrast physical characteristics. These problems attracted the interest of the mathematical community due to their connection with the blood flow models (see [22], [36] and [37]). The existence of a solution for FSI problem in an elastic pipe was studied in [16], [17] and [54].

In this thesis we consider the model of Navier–Stokes fluid motion in a pipe surrounded by an elastic wall which was developed by G. Panasenko and R. Stavre in [66]. Taking into account that physical properties of the wall are constant in time and simplifying the functions which describe the velocity of the fluid and the displacement of the wall we derive the 4^{th} order PDE which depends only on one space variable and time. Subsequently, we make a comparative analysis of a numerical solution to the full Navier–Stokes equations coupled with a moving wall and the derived 4^{th} order simplified PDE in two geometries: a cylinder and a Y-shaped network of cylinders. Remarkably, in the case when the difference of prescribed velocities between inlet and outlet of the cylinder is small, the solutions on cross sections in the middle of a cylinder obtained from the both approaches do not have significant difference. Notably, the solution of the 4^{th} order PDE demands less computational time, resulting in resource savings.

Finally, for the computation of the blood flow velocity within the left atrial appendage (LAA) of the human heart, with the aim of identifying stagnation zones which are linked to thrombosis according to the hypothesis of medical doctors, we develop a fully coupled FSI model, where the blood flow is described by Navier–Stokes equations with the moving heart wall (myocardium) considered as a shell. The human heart left arium (LA) fluid domain is obtained from cross sectional computed tomography (CT) scans of the human chest, while the boundary conditions for Navier–Stokes fluid

motion are formulated by using measurements of blood flow velocity on mitral valve zone by echocardiography. As a result, this model is patient-specific.

Actuality and literature review

The Poiseuille type solutions can be defined also in the nonstationary case (see [74], [75], [76], [77], [78], [79], [33] by K. Pileckas and [86] by S. S. Sritharan). Moreover, in [69] by K. Pileckas and G. Panasenko the behaviour of the nonstationary Poiseuille flow was studied in a thin cylinder (with the cross section of radius ε) and the asymptotics of it as $\varepsilon \to 0$ was found. In the time-periodic case such flows are usually called Womersley flows (see [99]). Results concerning the existence of time dependent Poiseuille flows lead to inverse problems. Such problems were studied by different authors, starting by J. R. Cannon (see [18], [19]) and then by many other authors. Particularly, H. Beirão da Veiga in [9] described a fully developed, time-periodic motion of a Navier–Stokes fluid within an infinite straight cylinder of constant cross section σ and proved the existence and uniqueness of the solution when the prescribed flow rate is sufficiently smooth. Furthermore, in [29] G. P. Galdi and A. M. Robertson presented a simpler than in [9] proof of the existence and uniqueness of the solution, moreover, they found the relation between the flow rate and the pressure slope.

It is known, that in practic applications of the Navier–Stokes equations the flow is often not defined by smooth functions, i.e. with minimal data regularity. The nonstationary Poiseuille-type solution, characterized by a prescribed initial condition and a given flow rate $F(t)$ belonging solely to $L^2(0,T)$, was investigated by K. Pileckas and R. Čiegis in [80]. The objective of Chapter 3 in this thesis is to extend the results of [80] to the time-periodic case, and to prove the uniqueness and the existence of a solution within the class of very weak solutions introduced in [80].

The interaction between a fluid and a deformable structure arises in many areas of real life, such as engineering and biology. The corresponding mathematical models are represented by the Fluid-Structure Interaction (FSI) problems, coupling two domains: liquid and solid. In [22], [36], [37] the existence of a solution for FSI problem for a fluid flow covered by a solid wall was proved. In [16], [17], [54] viscous flows in a pipe with elastic wall

was modeled either by a two-dimensional shell or a full-dimensional elasticity or visco-elasticity equations are studied. The goal of Chapter 4 is to study the model described in [60], [61], [62], [63], [64] and finalized in [65] and [66] and reduce it to a 4^{th} order PDE which describes the fluid flow in a pipe surrounded by an elastic wall. The developed FSI model for the solution to the Navier–Stokes equations in a cylinder interacting with its elastic wall described in Chapter 4 helps us in the computation of the blood velocity within the human heart LAA in Chapter 5.

It is well-known that atrial fibrillation is a key factor of thrombi formation within the human heart LAA (see [11]). Moreover, the lower blood flow velocity in LAA, the higher risk of stroke caused by a developed thrombus (see [47]). In order to explore stagnation zones within LAA, we need to compute the blood velocity in the whole left atrium in tandem with the motion of the heart wall. Two main directions are developed in this context: the first one is related to the detailed mathematical modeling of the coagulation process (coagulation cascade of reactions) combined with the hemodynamics (see [5], [13], [25], [26], [41], [48], [81], [89], [90], [91], [92], [93], [100], [102]); while the second one is the direct computer simulation of the blood flow in the patient-specific LAA with detection of stagnation zones as the probable places of thrombogenesis (see [2], [38], [58]), particularly [34] by M. García-Villalba *et al.* declares that in order to detect the stagnation zones in LAA blood flow kinetic energy (depending on the square of the velocity magnitude) can be computed. In Chapter 5 we develop a model of the LA (left atrium) for the computation of blood velocity which involves a numerical solution of the time-periodic Navier–Stokes equations, fully coupled with the FSI which demands less computational time comparing to [34].

Aims and problems

This thesis contains three different aims and problems which are related to hemodynamics.

I. **Time-periodic Navier–Stokes problem.** To prove the existence and uniqueness of the solution of time-periodic Navier–Stokes problem in an infinite cylinder with a prescribed time-periodic flow rate $F(t) \in L^2(0, 2\pi)$ under minimal regularity of data.

II. **FSI problem.** To reduce the FSI model into a 4^{th} order simplified PDE when the physical properties of the shell are constant in time and the functions which describe the velocity of the fluid and the displacement of the wall are simplified. To compute blood flow velocity in a single vessel considered as cylinder and a Y-shaped network of vessels considered as connected cylinders utilizing two approaches: the FSI model containing numerical solution of non-stacionary Navier–Stokes equations with a moving wall and the derived less time consumable 4^{th} order PDE in order to compare the obtained results from each model.

III. **The model of human heart left atrial appendage.** The third set of aims involves the study of the patient-specific human heart left atrium:
   a) Image processing, cleaning, geometry creation, and formulation of boundary conditions,
   b) Development of a numerical fully coupled LA model,
   c) Computation of blood flow velocity within the LAA.

Methods

Since this thesis includes several distinct tasks, the approaches for each task are different.

Chapter 2 is devoted to notation.

In Chapter 3 we prove the existence and uniqueness of a solution to the inverse time-periodic problem for the heat equation where the right hand side is unknown. We use methods of functional analysis, properties of Sobolev spaces, partial differential equations theory, theory of integral equations and Galerkin approximations.

In Chapter 4 we use an asymptotically developed FSI model from [66] and we derive the 4^{th} order PDE using mathematical analysis. For blood flow velocity computation in the non-stacionary Navier–Stokes model with a moving wall we utilize COMSOL Multiphysics code, and for the numerical solution of the derived 4^{th} order PDE we use MATLAB code developed by V. Šumskas in [87].

In Chapter 5 we compute blood flow velocity in human heart LA. Firstly, we receive a patient-specific cross section computed tomography (CT) pictures from medical doctors for image cleaning and geometry creation we use 3D Slicer (open source program) and Solidworks respectively. Then, for mesh simplification we used MeshLab (open source program). And finally, for blood flow velocity computation in the left atrium (LA) we used COMSOL Multiphysics code.

Novelty

To the best of our knowledge, all the results of this thesis are new.

In Chapter 3 the existence and uniqueness of the solution of time-periodic Navier–Stokes problem in an infinite cylinder with a prescribed flow rate $F(t) \in L^2(0, 2\pi)$ under minimal regularity of data was proven for the first time.

In Chapter 4 we simplify the FSI model developed by G. Panasenko and R. Stavre (see [66]) in 2020 to a less computation-time consumable 4^{th} order PDE. When the difference in inlet and outlet boundary conditions is small, the results obtained both from the numerical solution of non-stacionary Navier–Stokes equations in a cylinder with a moving wall (FSI model) and the derived 4^{th} order PDE are remarkably similar.

In Chapter 5 we compute blood flow velocity in the human heart left atrium (LA) and subsequently in the left atrial appendage (LAA). A. Quarteroni and his team in [15] propose a non-patient-specific mathematical and numerical model for the simulation of the heart function that couples cardiac electrophysiology, active and passive mechanics and hemodynamics, and includes reduced models for cardiac valves and the circulatory system. In this thesis we select two real-life patients with atrial fibrillation diagnosis: the first one who has experienced a stroke and the second one who has not. Our developed model shows that a patient who has experienced a stroke has a lower blood flow velocity in the LAA comparing with the second one. Moreover, in [12] by G. M. Bosi *et al.* for blood flow velocity computation in LAA in order to find stagnation zones the myocardium was considered as a hard wall, but since in the real life the wall of the heart is moving, we utilize an FSI model to obtain more realistic results. Additionally, recent

work [34] by M. García-Villalba *et al.* reveals that, in order to determine blood flow kinetic energy (dependent on the square of velocity magnitude), computations required 20 heartbeats until the model has stabilized, i.e. the computed blood flow velocity in the first 20 heartbeats was wrong; or, for example, in [12] by G. M. Bosi *et al.* computation required 10 heartbeats. In contrast, our LA model achieves stability after 3 heartbeats, resulting in significant computational time savings.

Structure of the dissertation and main results

The dissertation consists of five Chapters, Conclusions, Bibliography, Summary in Lithuanian language and Curriculum Vitae of the author.

Chapter 1 is an introduction to the research field, including the history, actuality of problems, methods and a brief description of results.

Chapter 2 outlines the notation and auxiliary results.

Chapter 3 delves into the theoretical analysis of time-periodic Navier–Stokes equations in a thin infinite cylinder with prescribed flow rate under minimal regularity of data.

In Chapter 4 we study the Poiseuille-type approximations for axisymmetric flow in a thin tube with thin stiff elastic wall. In this Chapter, our focus will be on a comparative analysis of numerical solutions to the non-stacionary Navier–Stokes problem in a cylinder with a moving wall (FSI model) and to the elastic wall Poiseuille equation (EWPE), i.e. we derive the 4^{th} order simplified PDE.

In Chapter 5 we develop a model which allows to compute blood flow velocity in human heart LAA. We conduct a comparative analysis of two patients both diagnosed with atrial fibrillation, with one having experienced a stroke and the other not.

Dissemination

The results of this thesis were presented at the following international seminars and conferences:

1. Eighth European Congress of Mathematics, University of Primorska, Portorož, Slovenia, 22-06-2021;

2. ICNAAM-2021 Conference, Rhodes, Greece, 22-09-2021;
3. Mathematical Modeling in Hemodynamics, Faculté des Sciences et Techniques, Université Jean Monnet, 08-12-2021;
4. MMA-2023 Conference, Jūrmala, Latvia, 06-06-2023;
5. MMA-2024 Conference, Pärnu, Estonia, 30-05-2024.

Furthermore, yearly results were disseminated during presentations at conferences organized by the Lithuanian Mathematical Society from 2020 to 2024.

Contributing talks were given at the seminars at the Department of Differential Equations (VU) on 25-04-2024, at the Department of Applied Mechanics (Vilnius TECH) on 11-05-2023 and at the Department of Mathematical Modelling (Vilnius TECH) on 12-03-2024.

Publications

The results of this thesis are published in the following papers:

1. K. Kaulakytė; N. Kozulinas; K. Pileckas. Time-periodic Poiseuille-type solution with minimally regular flow rate. *Nonlinear Analysis: Modelling and Control*, **26** (5) (2021) https://doi.org/10.15388/namc.2021.26.24502
2. K. Kaulakytė, N. Kozulinas, G. Panasenko, K. Pileckas, V. Šumskas. Poiseuille-Type Approximations for Axisymmetric Flow in a Thin Tube with Thin Stiff Elastic Wall. *Mathematics*, **11**(9), 2106 (2023) https://doi.org/10.3390/math11092106
3. A. Aidietis, S. Aidietienė, O. Ardatov, S. Borodinas, R. Katkus, K. Kaulakytė, N. Kozulinas, G. Panasenko, K. Pileckas, G. Račkauskas. Efficient Computation of Blood Velocity in the Left Atrial Appendage: A Practical Perspective. *In preparation.*

Chapter 2

Notation

Let V be a Banach space, with the norm of an element u denoted as $\|u\|_V$. Bold letters denote vector-valued functions, and for the spaces of scalar, vector-valued, and tensor-valued functions we use different notation. A vector-valued function $\mathbf{u} = (u_1, \ldots, u_n)$ belongs to a space V if $u_i \in V$ for $i = 1, \ldots, n$, and $\|\mathbf{u}\|_V = \sum_{i=1}^{n} \|u_i\|_V$. The dual space V^* of V is the Banach space consisting of all linear continuous functionals

$$f : v \mapsto \langle f, v \rangle,$$

where $\langle f, v \rangle$ denotes the value of the functional f at v. Alternatively, we may write

$$f : v \mapsto f(v),$$

omitting duality pairing notation.

A sequence $\{v_j\} \subset V$ *converges strongly* to $v \in V$, denoted as $v_j \to v$, if

$$\lim_{j \to \infty} ||v_j - v||_V = 0,$$

and $\{v_j\} \subset V$ *converges weakly* to $v \in V$, denoted as $v_j \rightharpoonup v$, if

$$\lim_{j \to \infty} \langle f, v_j \rangle = \langle f, v \rangle \quad \forall f \in V^*.$$

Let $\mathcal{D} \subset V$ be a linear subset of V. The closure of $\mathcal{D}$ in the norm $|| \cdot ||_V$ is denoted by $\overline{\mathcal{D}}^{||\cdot||_V}$. If $\overline{\mathcal{D}}^{||\cdot||_V} = V$, then $\mathcal{D}$ is called *dense* in V.

For function spaces we use standard notation. Let Ω be an arbitrary domain in $\mathbb{R}^n$. The set $C^\infty(\Omega)$ represents all infinitely differentiable functions defined on Ω, and $C_0^\infty(\Omega)$ is the subset of functions from $C^\infty(\Omega)$ with

compact support in Ω. For given non-negative integers k and $q \geqslant 1$, $L^q(\Omega)$ and $W^{k,q}(\Omega)$ denote Lebesgue and Sobolev spaces respectively with the norms

$$\|u\|_{L^q(\Omega)} = \left(\int\limits_{\Omega} |u|^q \, \mathrm{d}x \right)^{\frac{1}{q}} \text{ and } \|u\|_{W^{k,q}(\Omega)} = \left(\sum_{|\alpha|=0}^{k} \int\limits_{\Omega} |D^\alpha u(x)|^q \, \mathrm{d}x \right)^{\frac{1}{q}},$$

where $D^\alpha u = \dfrac{\partial^{|\alpha|} u}{\partial x_1^{\alpha_1} \dots \partial x_n^{\alpha_n}}$, $|\alpha| = \sum\limits_{j=1}^{n} \alpha_j$.

For $1 < q < \infty$ the space $L^q(\Omega)$ is reflexive. In the case $q = 2$, the space $L^2(\Omega)$ becomes Hilbert space with the inner product

$$(u, v)_{L^2(\Omega)} = \int\limits_{\Omega} u(x) v(x) \mathrm{d}x.$$

Let u and v be locally summable functions in Ω. Then for $D^\alpha u = v$ the following inequality holds for all test functions $\eta \in C_0^\infty(\Omega)$:

$$\int\limits_{\Omega} u D^\alpha \eta \mathrm{d}x = (-1)^{|\alpha|} \int\limits_{\Omega} v \eta \mathrm{d}x.$$

Let $\partial\Omega$ be a partial C^1 class boundary of $\Omega \subset \mathbb{R}^n$, $u(x), v(x) \in W^{1,2}(\Omega)$. Then for integration by parts we use the following formula:

$$\int\limits_{\Omega} \frac{\partial u(x)}{\partial x_k} v(x) \mathrm{d}x = - \int\limits_{\Omega} u(x) \frac{\partial v(x)}{\partial x_k} \mathrm{d}x + \int\limits_{\partial\Omega} u(x) v(x) \cos(\mathbf{n}, x_k) \mathrm{d}S,$$

where $\mathbf{n} = (n_1, ..., n_n)$ is unit vector of external normal to $\partial\Omega$ boundary, $(\mathbf{n}, x_k)$ is an angle between the normal $\mathbf{n}$ and axis x_k.

$\mathring{W}^{k,q}(\Omega)$ is the closure of $C_0^\infty(\Omega)$ in the norm of $W^{k,q}(\Omega)$.

$L^\infty(\Omega)$ is the space of all essentially bounded function with the norm

$$\|u\|_{L^\infty(\Omega)} = \operatorname*{ess\,sup}_{x \in \Omega} |u(x)|.$$

The space $L^q(0, T; V)$ is the space of functions u such that $u(\cdot, t) \in V$ for almost all $t \in [0, T]$ and the norm

$$\|u\|_{L^q(0,T;V)} = \Big(\int\limits_0^T \|u(\cdot, t)\|_V^q \, \mathrm{d}t \Big)^{\frac{1}{q}} < \infty, \quad 1 \leqslant q < \infty.$$

The definitions of other specific function spaces will be provided in the Chapters where they are introduced for the first time.

Consider a positive number T. The notation $V_{\wp}$ signifies that elements of the space V are T-periodic functions, i.e., $u(\cdot,t)=u(\cdot,t+T)$. Without loss of generality, we may assume that $T=2\pi$. Define $C^{\infty}_{\wp}(0,T;V)$ as the set of 2π-periodic smooth functions $u\in C^{\infty}(\mathbb{R})$ such that $u(t)=u(t+2\pi)$ for all $t\in[0,2\pi]$. Two additional spaces of periodic functions, $L^2_{\wp}(0,2\pi)$ and $W^{1,2}_{\wp}(0,2\pi)$, are introduced. These spaces are constructed through the inner product of $L^2(0,2\pi)$ and $W^{1,2}(0,2\pi)$, respectively.

Let $D(\Omega)$ be the Hilbert space of vector functions formed as the closure of $C_0^{\infty}(\Omega)$ in the Dirichlet norm $\|\mathbf{u}\|_{D(\Omega)}=\|\nabla\mathbf{u}\|_{L^2(\Omega)}$ generated by the scalar product

$$[\mathbf{u},\mathbf{v}]=\int\limits_{\Omega}\nabla\mathbf{u}\cdot\nabla\mathbf{v}\,\mathrm{d}x,$$

where $\nabla\mathbf{u}\cdot\nabla\mathbf{v}=\sum\limits_{j=1}^{n}\nabla u_j\cdot\nabla v_j=\sum\limits_{j=1}^{n}\sum\limits_{k=1}^{n}\dfrac{\partial u_j}{\partial x_k}\dfrac{\partial v_j}{\partial x_k}$.

Let $\{u_m\}_{m=1}^{\infty}$, $u\in W^{k,p}(\Omega)$. We say u_m strongly converges to u in $W^{k,p}(\Omega)$, written

$$u_m\to u\ \text{ in }\ W^{k,p}(\Omega),$$

provided

$$\lim_{m\to\infty}||u_m-u||_{W^{k,p}(\Omega)}=0.$$

In this thesis the following inequalities are used:

Lemma 2.0.1. *(Cauchy's inequality)*

$$ab\leqslant\varepsilon a^2+\frac{1}{4\varepsilon}b^2\quad\forall\varepsilon>0,\quad\forall a,b>0. \tag{2.1}$$

Lemma 2.0.2. *(Hölder inequality)*

$$\begin{aligned}\int\limits_{\Omega}|f(x)g(x)|\mathrm{d}x\leqslant\left(\int\limits_{\Omega}|f(x)|^q\mathrm{d}x\right)^{\frac{1}{q}}\left(\int\limits_{\Omega}|g(x)|^q\mathrm{d}x\right)^{\frac{1}{q}}\\ =||f||_{L_2(\Omega)}||g||_{L_2(\Omega)}.\end{aligned} \tag{2.2}$$

For $q=2$ (2.2) is called *Cauchy–Schwarz inequality.*

Lemma 2.0.3. *(Poincaré–Friedrich's inequality) The following inequality*

$$\|u\|^2_{L^2(\Omega)}\leqslant c\|\nabla u\|^2_{L^2(\Omega)}, \tag{2.3}$$

holds with the constant c in any bounded domain Ω for $u\in\mathring{W}^{1,2}(\Omega)$.

Chapter 3

Time-periodic Poiseuille-type solution with minimally regular flow rate

3.1 Introduction

The steady state Poiseuille flow in an infinite straight pipe $\Pi = \{x = (x', x_n) \in \mathbb{R}^n : \ x' \in \sigma \subset \mathbb{R}^{n-1}, \ -\infty < x_n < \infty, n = 2, 3\}$ of constant cross section σ was invented by Jean Louis Poiseuille in 1841 (see [72], [8], [46]). The Poiseuille flow is described by the fact that the associated velocity field has only one nonzero component $U(x')$ directed along the x_n-axis of Π which depends only on $x' \in \sigma$ and the pressure function $p = p(x_n)$ is linear. The Poiseuille-type solutions can be extended to the nonstationary case, as demonstrated by K. Pileckas (see [74], [75], [76], [77], [78], [79], [33]) and S. S. Sritharan in [86]. Moreover, in [69] by K. Pileckas and G. Panasenko the behaviour of the nonstationary Poiseuille flow was studied in a thin cylinder (with the cross section of radius ε) and the asymptotics of it as $\varepsilon \to 0$ was found.

In practical applications, the primary focus lies in situations where U (the velocity of fluid at cross section σ) is independent of time (referred to as steady flow) but, more generally, U shows periodic behavior with respect to time (called time-periodic flow or Womersley's flow (see [99])). Within the scope of this Chapter, our attention is directed toward the time-periodic flow under the minimal regularity of data, i.e. $F(t)$ belonging only to $L^2(0, T)$. It is worth noting that Poiseuille flow is significant in the study of fluid motion within "bent" pipes or pipes with varying cross sectional areas.

Typically, there are two methods to determine Poiseuille flow. These approaches involve prescribing either the axial pressure slope (further denoted as $q(t)$) or the flow rate (represented as $\int_\sigma U(x',t)\,\mathrm{d}x' = F(t)$). In the first case, the problem simplifies to solving a Poisson equation for $U = U(x')$ with a constant forcing term q, in the steady-state case, or a heat equation for $U = U(x',t)$ with a prescribed time-periodic forcing term $q(t)$ in the time-periodic case. Conversely, when we prescribe the flow rate $F(t)$, the challenge is to solve the inverse problem for both unknown $U(x',t)$ and $q(t)$, making the problem notably more complex, particularly in the time-periodic case. This complexity has been highlighted in [9] by H. Beirao da Veiga where it is demonstrated that the task of determining $U(x',t)$ and $q(t)$ can be reduced to solving a non-standard parabolic equation that includes a non-local term of the solution. The presence of this term arises from the fact that the relationship between $F(t)$ and $q(t)$ depends on the velocity field $U(x',t)$. Furthermore, in [29] by G. P. Galdi and A. M. Robertson a fully developed, time-periodic fluid flow in an infinite straight pipe of constant cross section σ was studied. Moreover, in [29], authors established a relationship between the axial pressure slope and the flow rate, they showed that the Fourier coefficients of the flow rate (flux) are related by an invertible, linear transformation depending only on cross section σ. One major consequence of this result is that the existence of a time-periodic Poiseuille flow with a prescribed flow rate can be reduced to the resolution of the problem with a suitable prescribed pressure gradient.

However, in the papers mentioned above the Poiseuille type solutions were studied in the case when data is sufficiently regular, i.e. $F \in W^{1,2}(\sigma)$. In real applications one usually does not have data defined by smooth functions, and it is important to study the case of minimal regularity of data. The nonstationary Poiseuille type solution with a prescribed initial condition and given flow rate (flux) $F(t)$ belonging only to $L^2(0,T)$ was studied by K. Pileckas and R. Čiegis in [80] where a new class of weak solutions was introduced and the existence and uniqueness of a solution in such class was proved.

The goal of this Chapter is to extend the result obtained in [80] to the case of time-periodic Poiseuille type solutions.

3.2 Problem formulation

Let us consider the time-periodic Navier–Stokes problem describing the motion of a viscous incompressible fluid in the infinite cylinder Π:

$$\begin{cases} \mathbf{u}_t - \nu\Delta\mathbf{u} + (\mathbf{u}\cdot\nabla)\mathbf{u} + \nabla p &= 0, \quad (x,t) \in \Pi \times (0,2\pi), \\ \text{div } \mathbf{u} &= 0, \quad (x,t) \in \Pi \times (0,2\pi), \\ \mathbf{u}|_{\partial\Pi\times(0,2\pi)} &= 0, \\ \mathbf{u}(x,0) &= \mathbf{u}(x,2\pi), \end{cases} \tag{3.1}$$

where $\mathbf{u}$ is the fluid velocity, p is the pressure function and $\nu > 0$ is the constant kinematic viscosity of the fluid.

We look for the solution $\mathbf{u}$ of (3.1) satisfying the additional condition of prescribed flow rate (flux) $F(t)$:

$$\int\limits_{\sigma} u_n(x,t)\,\mathrm{d}x' = F(t), \tag{3.2}$$

where $F(0) = F(2\pi)$. Without loss of generality we have supposed that the period is equal to 2π.

We look for the solution $(\mathbf{u}(x,t), p(x,t))$ of the problem (3.1) in the following expression

$$\mathbf{u}(x,t) = (0,\ldots,0,U_n(x',t)), \qquad p(x,t) = -q(t)x_n + p_0(t), \tag{3.3}$$

with an arbitrary function $p_0(t)$. Putting (3.3) into (3.1), we obtain the following problem on the cross section σ:

$$\begin{gathered} U_t(x',t) - \nu\Delta' U(x',t) = q(t), \\ U(x',t)\big|_{\partial\sigma} = 0, \quad U(x',0) = U(x',2\pi), \end{gathered} \tag{3.4}$$

where $U(x',t) = U_n(x',t)$ and $q(t)$ are unknown functions, Δ' is the Laplace operator with respect to x'. The nonlinear term vanishes because of the structure of Poiseuille flow (see 3.3).

The Poiseuille flow can be uniquely determined either prescribing the pressure slope $q(t)$ or the flow rate (flux) $F(t)$. In the first case the problem will be reduced to the standard time-periodic problem for the heat equation for unknown velocity $U = U(x',t)$ with time-periodic forcing $q(t)$. Problems of such type are well studied (see, e.g., [44]). However, in the real world applications the pressure is unknown, and only the flow rate (flux) of the

fluid is given. Therefore, it is necessary to study the Poiseuille flow with prescribed flow rate (flux) condition

$$\int_\sigma U(x',t)\,\mathrm{d}x' = F(t), \quad F(0) = F(2\pi). \tag{3.5}$$

In this case the solution of the problem (3.4), (3.5) is a pair of functions $(U(x',t), q(t))$ and one has to solve for $U(x',t)$ and $q(t)$ more complicated *inverse* parabolic problem: *for given $F(t)$ to find a pair of functions $(U(x',t), q(t))$ solving the problem* (3.4) *with $U(x',t)$ satisfying the flux condition* (3.5).

Thus, in the second case the relation between $q(t)$ and $F(t)$ depends on the solution of the inverse problem (in the stationary case the flux F and the pressure gradient q are proportional and the problem remains very simple). The solvability of the time-periodic problem with the assumption that the flux $F(t)$ is from the Sobolev space $W^{1,2}(0,2\pi)$ was proved by H. Beirão da Veiga [9] and in [29] an elementary relationship between the pressure drop $q(t)$ and the flux $F(t)$ was found. However, in applications and numerical computations usually data is not regular. Therefore, in this Chapter we study the problem (3.4), (3.5) assuming **only** that $F \in L^2(0,2\pi)$, i.e. the better smothness is unknown.

The problem (3.4), (3.5) can be reduced to the case when all involved functions have zero mean values. Let us denote by $\bar{H} = \frac{1}{2\pi}\int_0^{2\pi} H(t)\mathrm{d}t$ the mean value of a function H. Let $(\bar{U}, \bar{q})$ be a solution of the following problem on σ (the stationary Poiseuille solution corresponding to the flux $\bar{F}$)

$$\begin{cases} -\nu\Delta'\bar{U}(x') &= \bar{q}, \\ \bar{U}(x')|_{\partial\sigma} &= 0, \\ \displaystyle\int_\sigma \bar{U}(x')\mathrm{d}x' &= \bar{F}. \end{cases} \tag{3.6}$$

The solution $\bar{U}(x')$ of (3.6) can be represented in the form $\bar{U}(x') = \dfrac{\bar{F}}{\kappa_0}U_0(x')$ where

$$\begin{cases} -\nu\Delta' U_0(x') &= 1, \\ U_0(x')|_{\partial\sigma} &= 0, \end{cases} \tag{3.7}$$

and

$$\bar{q} = \frac{\bar{F}}{\kappa_0}, \quad \kappa_0 = \int_\sigma U_0(x')\mathrm{d}x' = \nu\int_\sigma |\nabla' U_0(x')|^2\mathrm{d}x' > 0. \tag{3.8}$$

We look for the solution (U,q) in the form

$$U(x',t)=V(x',t)+\bar{U}(x'),\quad q(t)=s(t)+\bar{q}. \tag{3.9}$$

Then obviously, $\bar{V}(x')=0$, $\bar{s}=0$ and (V,s) is the solution of the problem

$$\left\{\begin{array}{rcl} V_t(x',t)-\nu\Delta' V(x',t) &=& s(t),\\ V(x',t)|_{\partial\sigma} &=& 0,\\ V(x',0) &=& V(x',2\pi),\\ \displaystyle\int_\sigma V(x',t)\mathrm{d}x' &=& \widetilde{F}(t), \end{array}\right. \tag{3.10}$$

where $\widetilde{F}(t)=F(t)-\bar{F}$. So, $\bar{\widetilde{F}}=0$ and without loss of generality, we assume that $\bar{F}=0$.

Below we deal with a weak solution of the problem (3.4), (3.5) which is reduced to the case when involved functions have zero mean value and so we will study only this case.

The rest of the Chapter 3 is organized in the following way. In the Section 3.3 function spaces are defined and the main result is formulated. In the Section 3.4 the Galerkin approximations of the solution are constructed and in the Section 3.5 a priori estimates for these approximations are proved. In the Section 3.6 the main result of this Chapter, that is the existence and the uniqueness of the solution, is proved.

3.3 Notation and formulation of the main result

3.3.1 Function spaces

Hereby we define the spaces and notation needed for this Chapter.

Let us consider the set of smooth periodic functions $C^\infty_\wp(0,2\pi)=\{h\in C^\infty(\mathbb{R}^1): h(t)=h(t+2\pi)\ \forall t\in\mathbb{R}^1\}$.

Let $L^2(0,2\pi)$ be a Lebesgue space on the interval $(0,2\pi)$. We extend the functions from $L^2(0,2\pi)$ to the whole line $\mathbb{R}^1$ by putting $f(t+2\pi)=f(t)$ for any t. To emphasize that functions are periodically extended to $\mathbb{R}^1$ we use the notation $L^2_\wp(0,2\pi)$. Let $L^2_\sharp(0,2\pi)=\{h\in L^2_\wp(0,2\pi):\int_0^{2\pi}h(t)\mathrm{d}t=0\}$. Clearly, $L^2_\sharp(0,2\pi)$ is a closure of $C^\infty_\sharp(0,2\pi)=\{h\in C^\infty_\wp(0,2\pi):\int_0^{2\pi}h(t)\mathrm{d}t=0\}$ in $L^2(0,2\pi)$-norm and it is a proper subspace of $L^2_\wp(0,2\pi)$.

Denote by $W^{1,2}_{\wp}(0,2\pi)$ be the closure of the set $C^{\infty}_{\wp}(0,2\pi)$ in $W^{1,2}$-norm. Since function f from $W^{1,2}_{\wp}(0,2\pi)$ coincides with a continuous function on a set whose complement is of measure zero, we may assume that $f(0)=f(2\pi)$.

Let $W^{-1,2}_{\wp}(0,2\pi)$ be dual of $W^{1,2}_{\wp}(0,2\pi)$, i.e.,

$W^{-1,2}_{\wp}(0,2\pi)=\left(W^{1,2}_{\wp}(0,2\pi)\right)^*$.

For any function $f\in L^2_{\wp}(0,2\pi)$ denote by $S_f(t)$ its primitive:

$$S_f(t)=-\int\limits_{t}^{t_0+2\pi} f(\tau)\mathrm{d}\tau,\quad \text{where } t_0\in[0,2\pi), t\in[t_0,t_0+2\pi]. \tag{3.11}$$

Clearly, $\dfrac{dS_f(t)}{dt}=f(t),\ \ S_f(t_0+2\pi)=0.$

If $f\in L^2_{\sharp}(0,2\pi)$, then $S_f(t_0)=-\int\limits_{t_0}^{t_0+2\pi} f(\tau)\mathrm{d}\tau=-\int\limits_{0}^{2\pi} f(t)\mathrm{d}t=0.$

Moreover,

$$\int\limits_0^{2\pi}|S_f(t)|^2\mathrm{d}t\leqslant 2\pi\int\limits_0^{2\pi}\int\limits_t^{t_0+2\pi}|f(\tau)|^2\mathrm{d}\tau\mathrm{d}t\leqslant 4\pi^2\int\limits_{t_0}^{t_0+2\pi}|f(\tau)|^2\mathrm{d}\tau=4\pi^2\int\limits_0^{2\pi}|f(\tau)|^2\mathrm{d}\tau,$$

and $S_f(t)$ is a periodic function:

$$\begin{aligned}S_f(t+2\pi)=-\int\limits_{t+2\pi}^{t_0+2\pi} f(\tau)\mathrm{d}\tau=-\int\limits_{t}^{t_0} f(\tau)\mathrm{d}\tau=-\int\limits_{t}^{t_0+2\pi} f(\tau)\mathrm{d}\tau+\int\limits_{t_0}^{t_0+2\pi} f(\tau)\mathrm{d}\tau\\ =S_f(t)-S_f(t_0)=S_f(t).\end{aligned}$$

Thus, $S_f\in L^2_{\wp}(0,2\pi)$. Note that functions $S_f(t)$ defined by (3.11) with various t_0 differ from each other by a constant.

Note that the L^2-limit of a sequence $\{S_{f_n}\}\subset C^{\infty}_{\wp}(0,2\pi)$ is not necessary a primitive of some function from $L^2_{\sharp}(0,2\pi)$. In the lemma below we prove that an element $h\in W^{-1,2}_{\wp}(0,2\pi)$ possesses a primitive in the distributional sense.

Lemma 3.3.1. *Any functional $h\in W^{-1,2}_{\wp}(0,2\pi)$ can be represented in the form*

$$\langle h,\eta\rangle=\int\limits_0^{2\pi}H(t)\eta'(t)\mathrm{d}t\quad\forall\eta\in W^{1,2}_{\wp}(0,2\pi) \tag{3.12}$$

with a uniquely determined $H\in L^2_{\sharp}(0,2\pi)$.

Proof. Obviously the functional given by the formula (3.12) obeys the estimate

$$\big|\langle h,\eta\rangle\big| \leqslant \|H\|_{L^2_\sharp(0,2\pi)}\|\eta\|_{W^{1,2}_\wp(0,2\pi)}$$

and hence $h \in W^{-1,2}_\wp(0,2\pi)$.

Let us take an arbitrary functional $h \in W^{-1,2}_\wp(0,2\pi)$ and show that it can be represented in the form (3.12).

Consider the operator $\partial : \eta \in W^{1,2}_\wp(0,2\pi) \mapsto \eta' \in L^2_\sharp(0,2\pi)$ (due to periodicity $\int_0^{2\pi}\eta'(t)\mathrm{d}t = \eta(2\pi)-\eta(0)=0$). Since for any $\varphi \in L^2_\sharp(0,2\pi)$ the equality $\varphi = \eta'$ holds with

$$\eta(t) = -\int_t^{2\pi}\varphi(\tau)\mathrm{d}\tau \in W^{1,2}_\wp(0,2\pi), \tag{3.13}$$

we have $\mathcal{R}(\partial) = L^2_\sharp(0,2\pi)$ and the operator ∂ is an isomorphism from $W^{1,2}_\wp(0,2\pi)$ to $L^2_\sharp(0,2\pi)$, where the bounded operator $\partial^{-1} : L^2_\sharp(0,2\pi) \mapsto W^{1,2}_\wp(0,2\pi)$ is given by (3.13).

Since $V \in L^2_\sharp(0,2\pi;L^2(\sigma))$, S_V is a primitive of V, i.e. $(S_V)_t = V$, and we have the following inclusions $S_V \in L^2_\wp\big(0,2\pi;L^2(\sigma)\big)$, $(S_V)_t \in L^2_\sharp\big(0,2\pi;L^2(\sigma)\big)$. $S_V \in L^2_\wp\big(0,2\pi;\mathring{W}^{1,2}(\sigma)\big)$. The condition that $V|_{\partial\sigma} = 0$ is understood in the usual sense of traces (see [1]). If $S_V \in L^2\big(0,2\pi;\mathring{W}^{1,2}(\sigma)\big)$, then $S_V = -\int_t^{2\pi}V(\cdot,\tau)\mathrm{d}\tau \in \mathring{W}^{1,2}(\sigma)$ for a.a. $t \in (0,2\pi)$ and $\int_t^{2\pi}V(x',\tau)\mathrm{d}\tau|_{\partial\sigma} = 0$ in the sense of traces for such t. But then also $V(x',t)_{\partial\sigma} = 0$ in the sense of traces for a.a. $t \in (0,2\pi)$.

For $\varphi \in L^2_\sharp(0,2\pi)$ define the functional $M(\varphi) = \langle h, \partial^{-1}\varphi\rangle$. Clearly,

$$|M(\varphi)| \leqslant c\|h\|_{W^{-1,2}_\wp(0,2\pi)}\|\partial^{-1}\varphi\|_{W^{1,2}_\wp(0,2\pi)} \leqslant c\|h\|_{W^{-1,2}_\wp(0,2\pi)}\|\varphi\|_{L^2_\sharp(0,2\pi)}.$$

Hence there exists a uniquely defined $H \in L^2_\sharp(0,2\pi)$ such that $M(\varphi) = \int_0^{2\pi}H(\tau)\varphi(\tau)\mathrm{d}\tau \quad \forall\varphi \in L^2_\sharp(0,2\pi)$. Thus,

$$\langle h,\eta\rangle = \langle h,\partial^{-1}\varphi\rangle = \int_0^{2\pi}H(\tau)\varphi(\tau)\mathrm{d}\tau = \int_0^{2\pi}H(\tau)\eta'(\tau)\mathrm{d}\tau \quad \forall\eta \in W^{1,2}_\wp(0,2\pi)$$

and $\langle h,\eta\rangle$ is represented in the form (3.12). □

Remark 3.3.2. Note that if the functional h can be represented by $L^2_\sharp(0,2\pi)$ function, that is $\langle h,\eta\rangle = \int_0^{2\pi}H(t)\eta(t)\mathrm{d}t$ with $H \in L^2_\sharp(0,2\pi)$ and arbitrary

$\eta \in W^{1,2}_{\wp}(0,2\pi)$, then $H(t) = -\int_t^{2\pi} h(\tau)\mathrm{d}\tau$. Therefore, also in the case of a general functional h for the distributional primitive H we will use the notation $H(t) = S_h(t)$.

3.3.2 Formulation of the main result

Definition of a weak solution. *Let $F \in L^2_\sharp(0,2\pi)$. By a weak solution of the problem* (3.10) *we understand a pair (V,s) such that $V \in L^2_\sharp(0,2\pi;L^2(\sigma))$. $s \in W^{-1,2}_{\wp}(0,2\pi)$, $V(x',t)$ satisfies the flux condition*

$$\int_\sigma V(x',t)\mathrm{d}x' = F(t) \tag{3.14}$$

and the pair (V,s) satisfies the integral identity

$$\begin{aligned}\int_0^{2\pi}\int_\sigma V(x',t)\eta_t(x',t)\mathrm{d}x'\mathrm{d}t + \nu\int_0^{2\pi}\int_\sigma \nabla' S_V(x',t)\cdot\nabla'\eta_t(x',t)\mathrm{d}x'\mathrm{d}t \\ = \int_0^{2\pi} S_s(t)\int_\sigma \eta_t(x',t)\mathrm{d}x'\mathrm{d}t\end{aligned} \tag{3.15}$$

for any test function $\eta \in L^2_\wp(0,2\pi;\mathring{W}^{1,2}(\sigma))$ such that $\eta_t \in L^2_\sharp(0,2\pi;W^{1,2}(\sigma))$.

For a regular solution (V,s), taking into account that $\nabla V = (\nabla S_V)_t$, $s = S_s'$, the identity (3.15) can be easily obtained multiplying the equation $(3.10)_1$ by η, integrating over σ and over the interval $(0,2\pi)$, and integrating by parts with respect to x' and t. On the other hand, by uniqueness of such weak solution (V,s) (see Theorem 3.3.1 below), it follows that for $F \in W^{1,2}_\sharp(0,2\pi)$ the solution (V,s) coincides with the regular one, that is $V \in L^2_\sharp(0,2\pi;\mathring{W}^{1,2}(\sigma)\cap W^{2,2}(\sigma))$, $V_t \in L^2_\sharp(0,2\pi;L^2(\sigma))$, $s \in L^2_\sharp(0,2\pi)$. Thus, the proposed definition is an extension of the concept of weak solutions.

Theorem 3.3.1. *Let $F \in L^2_\sharp(0,2\pi)$. Then the problem* (3.10) *admits a unique weak solution (V,s). There holds the estimate*

$$\begin{aligned}\int_0^{2\pi}\int_\sigma |V(x',t)|^2\mathrm{d}x'\mathrm{d}t + \int_0^{2\pi}\int_\sigma \left|\nabla' S_V(x',t)\right|^2\mathrm{d}x'\mathrm{d}t \\ + \int_0^{2\pi}|S_s(\tau)|^2\mathrm{d}\tau \leqslant c\int_0^{2\pi}|F(\tau)|^2\mathrm{d}\tau,\end{aligned} \tag{3.16}$$

where the constant c depends only on σ.

Remark 3.3.3. Since $\int_0^{2\pi} \eta'(t)\mathrm{d}t = 0$ for $\eta \in W^{1,2}_{\wp}(0,2\pi)$ and all primitives of the function $V(x',t)$ differ from each other by a function independent of t, the integral identity (3.15) remains valid for any primitive function S_V and we can assume, for example, that S_V is taken to be zero at the point $t = 2\pi$.

Theorem 3.3.1 will be proved applying some version of Galerkin approximations (see Sections 3 and 4). Notice that in order to get the estimates of the approximate solutions $\left(V_\alpha^{(N)}(x',t), s_\alpha^{(N)}(t)\right)$ we have used primitive functions defined over the integrals $\int_t^{t_*+2\pi} ...$, with specially chosen points $t_* = t_*(\alpha, N) \in [0, 2\pi)$ and $t \in (t_*, t_* + 2\pi)$. Thus, the estimate (3.16) is valid only for the primitive function S_V obtained as a limit of the sequence $\left\{S_{V_\alpha^{(N)}}\right\}$.

3.4 Construction of Galerkin approximations

Let $u_k(x') \in \mathring{W}^{1,2}(\sigma)$ and λ_k be eigenfunctions and eigenvalues of the Laplace operator:

$$\left\{ \begin{array}{rcl} -\nu\Delta' u_k(x') & = & \lambda_k u_k(x'), \\ u_k(x')\big|_{\partial\sigma} & = & 0. \end{array} \right. \tag{3.17}$$

Note that $\lambda_k > 0$ and $\lim\limits_{k\to\infty} \lambda_k = \infty$. The eigenfunctions $u_k(x')$ are orthogonal in $L^2(\sigma)$ and we assume that $u_k(x')$ are normalized in $L^2(\sigma)$. Then

$$\nu \int\limits_\sigma |\nabla' u_k(x')|^2 \,\mathrm{d}x' = \lambda_k, \quad \int\limits_\sigma \nabla' u_k(x') \cdot \nabla' u_l(x') \,\mathrm{d}x' = 0, \quad k \neq l.$$

Moreover, $\{u_k(x')\}$ is a basis in $L^2(\sigma)$ and $\mathring{W}^{1,2}(\sigma)$ (see [56]).

We look for an approximate solution of the problem (3.10) in the form

$$V^{(N)}(x',t) = \sum_{k=1}^{N} w_k^{(N)}(t) u_k(x'). \tag{3.18}$$

The coefficients $w_k^{(N)}(t)$ and the function $s^{(N)}(t)$ are obtained by solving the following problems

$$\begin{aligned}
&\int_\sigma V_t^{(N)}(x',t)u_k(x')\mathrm{d}x' + \nu \int_\sigma \nabla' V^{(N)}(x',t)\cdot\nabla' u_k(x')\mathrm{d}x' \\
&\qquad = s^{(N)}(t)\int_\sigma u_k(x')\mathrm{d}x', \quad k=1,2,\dots,N, \\
&\qquad w_k^{(N)}(0) = w_k^{(N)}(2\pi), \quad k=1,\dots,N, \\
&\qquad \int_\sigma V^{(N)}(x',t)\,\mathrm{d}x' = F(t),
\end{aligned} \tag{3.19}$$

which in virtue of the orthonormality of functions $u_k(x')$ are equivalent to the ordinary differential equations for the functions $w_k^{(N)}(t)$:

$$\begin{cases}
(w_k^{(N)}(t))' + \lambda_k w_k^{(N)}(t) &= \beta_k s^{(N)}(t), \quad t\in(0,2\pi), \\
w_k^{(N)}(0) &= w_k^{(N)}(2\pi),
\end{cases} \tag{3.20}$$

where $\beta_k = \int_\sigma u_k(x')\mathrm{d}x'$.

Note that $\sum_{k=1}^\infty \beta_k u_k(x') = 1$ and $\sum_{k=1}^\infty \beta_k^2 = |\sigma|$.

The solution of the problem (3.20) has the form (see [57])

$$w_k^{(N)}(t) = \beta_k \int_0^{2\pi} G_k(t,\tau)s^{(N)}(\tau)\mathrm{d}\tau, \tag{3.21}$$

where

$$G_k(t,\tau) = \begin{cases}
\dfrac{e^{-\lambda_k(t-\tau)}}{1-e^{-2\pi\lambda_k}}, & 0\leqslant\tau\leqslant t\leqslant 2\pi, \\[2ex]
\dfrac{e^{-\lambda_k(t-\tau+2\pi)}}{1-e^{-2\pi\lambda_k}}, & 0\leqslant t\leqslant\tau\leqslant 2\pi.
\end{cases}$$

Indeed, if we substitute (3.21) into $(3.20)_1$ we get

$$\left(\beta_k\int_0^{2\pi} G_k(t,\tau)s^{(N)}(\tau)\mathrm{d}\tau\right)' + \lambda_k\beta_k\int_0^{2\pi} G_k(t,\tau)s^{(N)}(\tau)\mathrm{d}\tau = \beta_k s^{(N)}(t), \quad t\in(0,2\pi),$$

dividing the obtained expression by β_k, separating $e^{-\lambda_k t}$ and $e^{\lambda_k \tau}$ we get

$$\begin{aligned}
&\left[e^{-\lambda_k t}\left(\int_0^t \frac{e^{\lambda_k \tau}}{1-e^{-2\pi\lambda_k}} s^{(N)}(\tau)\mathrm{d}\tau + \int_t^{2\pi} \frac{e^{\lambda_k(\tau-2\pi)}}{1-e^{-2\pi\lambda_k}} s^{(N)}(\tau) d\tau\right)\right]' \\
&\quad +\lambda_k\left(\int_0^t \frac{e^{-\lambda_k(t-\tau)}}{1-e^{-2\pi\lambda_k}} s^{(N)}(\tau)\mathrm{d}\tau + \int_t^{2\pi} \frac{e^{-\lambda_k(t-\tau+2\pi)}}{1-e^{-2\pi\lambda_k}} s^{(N)}(\tau)\mathrm{d}\tau\right) \\
&= -\lambda_k e^{-\lambda_k t}\left(\int_0^t \frac{e^{\lambda_k \tau}}{1-e^{-2\pi\lambda_k}} s^{(N)}(\tau)\mathrm{d}\tau + \int_t^{2\pi} \frac{e^{\lambda_k(\tau-2\pi)}}{1-e^{-2\pi\lambda_k}} s^{(N)}(\tau)\mathrm{d}\tau\right) \\
&\qquad +\frac{1}{1-e^{-2\pi\lambda_k}} s^{(N)}(t) - \frac{e^{-2\pi\lambda_k}}{1-e^{-2\pi\lambda_k}} s^{(N)}(t) \\
&\quad +\lambda_k\left(\int_0^t \frac{e^{-\lambda_k(t-\tau)}}{1-e^{-2\pi\lambda_k}} s^{(N)}(\tau)\mathrm{d}\tau + \int_t^{2\pi} \frac{e^{-\lambda_k(t-\tau+2\pi)}}{1-e^{-2\pi\lambda_k}} s^{(N)}(\tau)\mathrm{d}\tau\right) \\
&\qquad = s^{(N)}(\tau), \quad t \in (0, 2\pi),
\end{aligned}$$

Moreover, since

$$w_k^{(N)}(0) = \beta_k \int_0^{2\pi} \frac{e^{-\lambda_k(0-\tau+2\pi)}}{1-e^{-2\pi\lambda_k}} s^{(N)}(\tau)\mathrm{d}\tau,$$

and

$$w_k^{(N)}(2\pi) = \beta_k \int_0^{2\pi} \frac{e^{-\lambda_k(2\pi-\tau)}}{1-e^{-2\pi\lambda_k}} s^{(N)}(\tau)\mathrm{d}\tau,$$

we get that $w_k^{(N)}(0) = w_k^{(N)}(2\pi)$.

Substituting the expression (3.21) into (3.18) we obtain

$$V^{(N)}(x', t) = \sum_{k=1}^{N} \beta_k \int_0^{2\pi} G_k(t, \tau) s^{(N)}(\tau)\mathrm{d}\tau\, u_k(x').$$

Now the flux condition yields

$$\begin{aligned}
F(t) = \int_\sigma V^{(N)}(x', t)\mathrm{d}x' &= \sum_{k=1}^{N} \beta_k \int_0^{2\pi} G_k(t, \tau) s^{(N)}(\tau)\mathrm{d}\tau \int_\sigma u_k(x')\mathrm{d}x' \\
&= \sum_{k=1}^{N} \beta_k^2 \int_0^{2\pi} G_k(t, \tau) s^{(N)}(\tau)\mathrm{d}\tau.
\end{aligned}$$

Thus for the function $s^{(N)}$ we derived Fredholm integral equation of the first kind:

$$\int_0^{2\pi} \sum_{k=1}^{N} \beta_k^2 G_k(t,\tau) s^{(N)}(\tau) \mathrm{d}\tau = F(t). \tag{3.22}$$

It is well known (see, e.g., [45], [84]) that such equations, in general, are ill-posed in L^2 setting. In order to regularize the equation (3.22), we consider the following Fredholm integral equation of the second kind:

$$\alpha s_\alpha^{(N)}(t) + \int_0^{2\pi} \sum_{k=1}^{N} \beta_k^2 G_k(t,\tau) s_\alpha^{(N)}(\tau) \mathrm{d}\tau = F(t), \tag{3.23}$$

where later α will tend to 0, i.e., instead of the problem (3.19), (3.22), we study the regularized problem

$$\begin{gathered}
\int_\sigma (V_\alpha^{(N)})_t(x',t) u_k(x') \mathrm{d}x' + \nu \int_\sigma \nabla' V_\alpha^{(N)}(x',t) \cdot \nabla' u_k(x') \mathrm{d}x' \\
= s_\alpha^{(N)}(t) \int_\sigma u_k(x') \mathrm{d}x', \quad k = 1,2,\ldots,N, \\
V_\alpha^{(N)}(x',0) = V_\alpha^{(N)}(x',2\pi), \\
\alpha s_\alpha^{(N)}(t) + \int_0^{2\pi} \sum_{k=1}^{N} \beta_k^2 G_k(t,\tau) s_\alpha^{(N)}(\tau) \mathrm{d}\tau = F(t),
\end{gathered} \tag{3.24}$$

where

$$V_\alpha^{(N)}(x',t) = \sum_{k=1}^{N} w_{k,\alpha}^{(N)}(t) u_k(x'),$$

$$w_{k,\alpha}^{(N)}(t) = \beta_k \int_0^{2\pi} G_k(t,\tau) s_\alpha^{(N)}(\tau) \mathrm{d}\tau,$$

Lemma 3.4.1. *Let $F \in L^2_\sharp(0,2\pi)$. Then the equation* (3.23) *admits a unique solution $s_\alpha^{(N)} \in L^2_\sharp(0,2\pi)$.*

Proof. First we show that the equation (3.23) is well defined in the space $L^2_\sharp(0,2\pi)$. Obviously, if F is periodic and $s_\alpha^{(N)}$ is the solution of (3.23) , then $s_\alpha^{(N)}$ also is a periodic function. Assume that mean value $\bar{F}=0$. Then

$$\overline{\alpha\bar{s}_\alpha^{(N)}+\int\limits_0^{2\pi}\sum_{k=1}^{N}\beta_k^2 s_\alpha^{(N)}(\tau)\int\limits_0^{2\pi}G_k(t,\tau)\mathrm{d}t\mathrm{d}\tau}=0. \tag{3.25}$$

Since

$$\int\limits_0^{2\pi}G_k(t,\tau)\mathrm{d}t=\frac{1}{1-e^{-2\pi\lambda_k}}\left(\int\limits_\tau^{2\pi}e^{-\lambda_k(t-\tau)}\mathrm{d}t+\int\limits_0^{\tau}e^{-\lambda_k(t-\tau+2\pi)}\mathrm{d}t\right)$$
$$=-\frac{1}{\lambda_k(1-e^{-2\pi\lambda_k})}\left(e^{-\lambda_k(t-\tau)}\Big|_{t_1=\tau}^{t_2=2\pi}+e^{-\lambda_k(t-\tau+2\pi)}\Big|_{t_1=0}^{t_2=\tau}\right)=\frac{1}{\lambda_k},$$

the second term in (3.25) is equal to $\sum\limits_{k=1}^{N}\dfrac{\beta_k^2}{\lambda_k}\bar{s}_\alpha^{(N)}$ and from (3.25) it follows that

$$\left(\alpha+\sum_{k=1}^{N}\frac{\beta_k^2}{\lambda_k}\right)\bar{s}_\alpha^{(N)}=0$$

and thus, $\bar{s}_\alpha^{(N)}=0$.

From this it follows that the mean value $\bar{V}_\alpha^{(N)}(x')$ of $V_\alpha^{(N)}(x',t)$ also vanishes: $\bar{V}_\alpha^{(N)}(x')=0$.

It is well known that Fredholm integral equations of the second kind satisfy the Fredholm alternative (e.g., [94]). So, it is enough to prove the uniqueness of the solution to (3.23). Let $F(t)=0$.

By construction, $\int\limits_0^{2\pi}\sum\limits_{k=1}^{N}\beta_k^2G_k(t,\tau)s_\alpha^{(N)}(\tau)\mathrm{d}\tau=\int\limits_\sigma V_\alpha^{(N)}(x',t)\mathrm{d}x'$ and the homogeneous equation (3.23) gives

$$\int\limits_\sigma V_\alpha^{(N)}(x',t)\mathrm{d}x'=-\alpha s_\alpha^{(N)}(t).$$

Multiplying $(3.24)_1$ by $w_{k,\alpha}^{(N)}(t)$, summing by k from 1 to N and integrating over the interval $(0,2\pi)$ yields

$$\int_0^{2\pi}\int_\sigma (V_\alpha^{(N)})_t(x',t)V_\alpha^{(N)}(x',t)\mathrm{d}x'\mathrm{d}t+\nu\int_0^{2\pi}\int_\sigma |\nabla' V_\alpha^{(N)}(x',t)|^2\mathrm{d}x'\mathrm{d}t$$
$$=\int_0^{2\pi} s_\alpha^{(N)}(t)\int_\sigma V_\alpha^{(N)}(x',\tau)\mathrm{d}x'\mathrm{d}\tau\mathrm{d}t=-\alpha\int_0^{2\pi}|s_\alpha^{(N)}(t)|^2\mathrm{d}t. \tag{3.26}$$

After integration with respect to t, taking into account the time-periodicity of $V_\alpha^{(N)}(x',t)$ and the fact that $\int_\sigma (V_\alpha^{(N)})_t(x',t)V_\alpha^{(N)}(x',t)\mathrm{d}x'\mathrm{d}t$ $=\frac{1}{2}\int_\sigma \left((V_\alpha^{(N)})^2\right)_t(x',t)\mathrm{d}x'$ we obtain

$$\nu\int_0^{2\pi}\int_\sigma |\nabla' V_\alpha^{(N)}(x',t)|^2\mathrm{d}x'\mathrm{d}t+\alpha\int_0^{2\pi}|s_\alpha^{(N)}(t)|^2\mathrm{d}t=0.$$

Thus, $s_\alpha^{(N)}(t)=0$ for a.a. $t\in[0,2\pi]$ and lemma is proved. □

3.5 A priori estimates of the Galerkin approximations

Let the pair $(V_\alpha^{(N)}(x',t),s_\alpha^{(N)}(t))$ be a solution of the problem (3.24) and $U_0(x')$ be the solution of problem (3.7).

Consider the integral $\int_\sigma V_\alpha^{(N)}(x',t)U_0(x')\mathrm{d}x'$. Since the mean value $\bar{V}_\alpha^{(N)}(x')=0$, we have

$$\int_0^{2\pi}\int_\sigma V_\alpha^{(N)}(x',t)U_0(x')\mathrm{d}x'\mathrm{d}t=\int_\sigma U_0(x')\left(\int_0^{2\pi}V_\alpha^{(N)}(x',t)\mathrm{d}t\right)\mathrm{d}x'=0.$$

Therefore, by the Mean Value Theorem there exists $t_*=t_*(\alpha,N)$ such that $\int_\sigma V_\alpha^{(N)}(x',t_*)U_0(x')\mathrm{d}x'=0$. The point $t_*(\alpha,N)$ depends on α and N, but in this section we denote it just t_* in order to simplify the notation. By periodicity we also have $\int_\sigma V_\alpha^{(N)}(x',t_*+2\pi)U_0(x')\mathrm{d}x'=0$.

Let $f\in L^2_\sharp(0,2\pi)$. For $t\in[t_*,t_*+2\pi]$ define the notation

$S_f^*(t)=-\int_t^{t_*+2\pi}f(\tau)\mathrm{d}\tau$. Since the mean value of f vanishes, we have $S_f^*(t_*+2\pi)=S_f^*(t_*)=0$. Moreover, $\dfrac{dS_f^*(t)}{dt}=f(t)$.

Lemma 3.5.1. *The following estimate*

$$\begin{aligned}\int_{t_*}^{t_*+2\pi}\int_{\sigma}|V_\alpha^{(N)}(x',t)|^2\mathrm{d}x'\mathrm{d}t+\int_{t_*}^{t_*+2\pi}\int_{\sigma}\left|\nabla' S^*_{V_\alpha^{(N)}}(x',t)\right|^2\mathrm{d}x'\mathrm{d}t\\ +\int_{t_*}^{t_*+2\pi}|S^*_{s_\alpha^{(N)}}(\tau)|^2\mathrm{d}\tau\leqslant c\int_{t_*}^{t_*+2\pi}|F(\tau)|^2\mathrm{d}\tau\end{aligned}\tag{3.27}$$

holds with a constant c independent of α and N.

Proof. Define $\gamma_{k,\alpha}^{(N)}(t)=\int_t^{2\pi+t_*}w_{k,\alpha}^{(N)}(\tau)\mathrm{d}\tau,\ t_*\leqslant t\leqslant 2\pi+t_*$. Multiplying $(3.24)_1$ by $\gamma_{k,\alpha}^{(N)}(t)$, summing the obtained relation from $k=1$ to $k=N$ and integrating them over the interval $(t_*,t_*+2\pi)$ we obtain

$$\begin{aligned}&\int_{t_*}^{t_*+2\pi}\int_{\sigma}(V_\alpha^{(N)})_t(x',t)\int_t^{t_*+2\pi}V_\alpha^{(N)}(x',\tau)\mathrm{d}\tau\mathrm{d}x'\mathrm{d}t\\ &+\nu\int_{t_*}^{t_*+2\pi}\int_{\sigma}\nabla' V_\alpha^{(N)}(x',t)\int_t^{t_*+2\pi}\nabla' V_\alpha^{(N)}(x',\tau)\mathrm{d}\tau\mathrm{d}x'\mathrm{d}t\\ &=\int_{t_*}^{t_*+2\pi}s_\alpha^{(N)}(t)\int_t^{t_*+2\pi}\int_{\sigma}V_\alpha^{(N)}(x',\tau)\mathrm{d}x'\mathrm{d}\tau\mathrm{d}t.\end{aligned}\tag{3.28}$$

Using the relation

$$\int_{\sigma}V_\alpha^{(N)}(x',t)\mathrm{d}x'=\sum_{k=1}^{N}\beta_k^2\int_0^{2\pi}G_k(t,\tau)s_\alpha^{(N)}(\tau)\mathrm{d}\tau$$

and $(3.24)_3$ we derive

$$\int_{\sigma}V_\alpha^{(N)}(x',t)\mathrm{d}x'=F(t)-\alpha s_\alpha^{(N)}(t).$$

Therefore, (3.28) can be written as

$$\begin{aligned}&\int_{t_*}^{t_*+2\pi}\int_{\sigma}\left(V_\alpha^{(N)}\right)_t(x',t)\int_t^{t_*+2\pi}V_\alpha^{(N)}(x',\tau)\mathrm{d}\tau\mathrm{d}x'\mathrm{d}t\\ &+\nu\int_{t_*}^{t_*+2\pi}\int_{\sigma}\nabla' V_\alpha^{(N)}(x',t)\int_t^{t_*+2\pi}\nabla' V_\alpha^{(N)}(x',\tau)\mathrm{d}\tau\mathrm{d}x'\mathrm{d}t\\ &=\int_{t_*}^{t_*+2\pi}s_\alpha^{(N)}(t)\int_t^{t_*+2\pi}\left(F(\tau)-\alpha s_\alpha^{(N)}(\tau)\right)\mathrm{d}\tau\mathrm{d}t.\end{aligned}\tag{3.29}$$

Then

$$\int_{t_*}^{t_*+2\pi} s_\alpha^{(N)}(t) \int_t^{t_*+2\pi} (F(\tau)-\alpha s_\alpha^{(N)}(\tau))\mathrm{d}\tau\mathrm{d}t$$

$$= \int_{t_*}^{t_*+2\pi} \frac{dS^*_{s_\alpha^{(N)}}(t)}{dt} \int_t^{t_*+2\pi} (F(\tau)-\alpha s_\alpha^{(N)}(\tau))\mathrm{d}\tau\mathrm{d}t$$

$$= \int_{t_*}^{t_*+2\pi} S^*_{s_\alpha^{(N)}}(t)F(t)\mathrm{d}t - \alpha \int_{t_*}^{t_*+2\pi} S^*_{s_\alpha^{(N)}}(t)s_\alpha^{(N)}(t)\mathrm{d}t$$

$$= \int_{t_*}^{t_*+2\pi} S^*_{s_\alpha^{(N)}}(t)F(t)\mathrm{d}t - \alpha \int_{t_*}^{t_*+2\pi} S^*_{s_\alpha^{(N)}}(t)\frac{dS^*_{s_\alpha^{(N)}}(t)}{dt}\mathrm{d}t = \int_{t_*}^{t_*+2\pi} S^*_{s_\alpha^{(N)}}(t)F(t)\mathrm{d}t.$$

Calculating similarly two integrals J_1 and J_2 on the left hand side of (3.29) we derive that

$$J_1 = \int_{t_*}^{t_*+2\pi} \int_\sigma \left|V_\alpha^{(N)}(x',t)\right|^2 \mathrm{d}x'\mathrm{d}t, \quad J_2 = 0.$$

Hence the relation (3.29) takes the form

$$\int_{t_*}^{t_*+2\pi} \int_\sigma \left|V_\alpha^{(N)}(x',t)\right|^2 \mathrm{d}x'\mathrm{d}t = \int_{t_*}^{t_*+2\pi} S^*_{s_\alpha^{(N)}}(t)F(t)\mathrm{d}t. \tag{3.30}$$

Now multiply $(3.24)_1$ by $(t-t_*)\gamma_{k,\alpha}^{(N)}(t)$, the sum from $k=1$ to $k=N$ and integrate over the interval $(t_*, t_*+2\pi)$:

$$\begin{aligned} &\int_{t_*}^{t_*+2\pi} \int_\sigma (t-t_*)\left(V_\alpha^{(N)}\right)_t(x',t) \int_t^{t_*+2\pi} V_\alpha^{(N)}(x',\tau)\mathrm{d}\tau\mathrm{d}x'\mathrm{d}t \\ &+\nu \int_{t_*}^{t_*+2\pi} \int_\sigma (t-t_*)\nabla' V_\alpha^{(N)}(x',t) \int_t^{t_*+2\pi} \nabla' V_\alpha^{(N)}(x',\tau)\mathrm{d}\tau\mathrm{d}x'\mathrm{d}t \\ &= \int_{t_*}^{t_*+2\pi} (t-t_*)s_\alpha^{(N)}(t) \int_t^{t_*+2\pi} (F(\tau)-\alpha s_\alpha^{(N)}(\tau))\mathrm{d}\tau\mathrm{d}t. \end{aligned} \tag{3.31}$$

Evaluating each of the three integrals in (3.31) and having in mind that mean values of participating functions are zero, we obtain

$$\begin{aligned}\int_{t_*}^{t_*+2\pi}\int_{\sigma}(t-t_*)|V_\alpha^{(N)}(x',t)|^2\mathrm{d}x'\mathrm{d}t+\frac{\nu}{2}\int_{t_*}^{t_*+2\pi}\int_{\sigma}|\nabla' S^*_{V_\alpha^{(N)}}(x',t)|^2\mathrm{d}x'\mathrm{d}t\\ =\int_{t_*}^{t_*+2\pi}(t-t_*)S^*_{s_\alpha^{(N)}}(t)F(t)\mathrm{d}t-\frac{\alpha}{2}\int_{t_*}^{t_*+2\pi}\left|S^*_{s_\alpha^{(N)}}(t)\right|^2\mathrm{d}t\\ -\int_{t_*}^{t_*+2\pi}S^*_{s_\alpha^{(N)}}(t)\int_{t}^{t_*+2\pi}F(\tau)\mathrm{d}\tau\mathrm{d}t.\end{aligned}\tag{3.32}$$

From (3.30) and (3.32) it follows that

$$\begin{aligned}\int_{t_*}^{t_*+2\pi}\int_{\sigma}|V_\alpha^{(N)}(x',t)|^2\mathrm{d}x'\mathrm{d}t\leqslant\varepsilon\int_{t_*}^{t_*+2\pi}\left|S^*_{s_\alpha^{(N)}}(t)\right|^2\mathrm{d}t\\ +\frac{1}{2\varepsilon}\int_{t_*}^{t_*+2\pi}|F(t)|^2\mathrm{d}t,\end{aligned}\tag{3.33}$$

and

$$\begin{aligned}&\frac{\nu}{2}\int_{t_*}^{t_*+2\pi}\int_{\sigma}|\nabla' S^*_{V_\alpha^{(N)}}(x',t)|^2\mathrm{d}x'\mathrm{d}t\\ &\leqslant\left|\int_{t_*}^{t_*+2\pi}(t-t_*)S^*_{s_\alpha^{(N)}}(t)F(t)\mathrm{d}t\right|+\left|\int_{t_*}^{t_*+2\pi}S^*_{s_\alpha^{(N)}}(t)\int_{t}^{t_*+2\pi}F(\tau)\mathrm{d}\tau\mathrm{d}t\right|\\ &\leqslant\varepsilon(4\pi^2+1)\int_{t_*}^{t_*+2\pi}|S^*_{s_\alpha^{(N)}}(t)|^2\mathrm{d}t+\frac{1}{2\varepsilon}\int_{t_*}^{t_*+2\pi}|F(t)|^2\mathrm{d}t\\ &\quad+\frac{1}{2\varepsilon}\int_{t_*}^{t_*+2\pi}\left|\int_{t}^{t_*+2\pi}F(\tau)\mathrm{d}\tau\right|^2\mathrm{d}t\\ &\leqslant(4\pi^2+1)\left(\varepsilon\int_{t_*}^{t_*+2\pi}|S^*_{s_\alpha^{(N)}}(t)|^2\mathrm{d}t+\frac{1}{2\varepsilon}\int_{t_*}^{t_*+2\pi}|F(t)|^2\mathrm{d}t\right).\end{aligned}\tag{3.34}$$

Let us estimate the integral $\int_{t_*}^{t_*+2\pi}\left|S^*_{s_\alpha^{(N)}}(t)\right|^2\mathrm{d}t$. Let $U_0\in\mathring{W}^{1,2}(\sigma)$ be a solution of the problem (3.7). Remind that the flux of U_0 is nonzero, $\kappa_0=\int_\sigma U_0(x')\mathrm{d}x'>0$ (see (3.8)). Since $\{u_k(x')\}$ is a basis in $\mathring{W}^{1,2}(\sigma)$, U_0 can be expressed as a Fourier series in $\mathring{W}^{1,2}(\sigma)$:

$$U_0(x')=\sum_{k=1}^{\infty}a_k u_k(x'),\quad a_k\in\mathbb{R}^1.$$

Let us multiply the relations $(3.24)_1$ by a_k and sum them over k. This gives

$$\begin{aligned}\int_\sigma (V_\alpha^{(N)})_t(x',t)U_0(x')\mathrm{d}x' + \nu\int_\sigma \nabla' V_\alpha^{(N)}(x',t)\cdot\nabla' U_0(x')\mathrm{d}x' \\ = s_\alpha^{(N)}(t)\int_\sigma U_0(x')\mathrm{d}x' = s_\alpha^{(N)}(t)\kappa_0.\end{aligned} \tag{3.35}$$

On the other hand, multiplying (3.7) by $V_\alpha^{(N)}(x',t)$ and integrating by parts in σ we obtain

$$\begin{aligned}\nu\int_\sigma \nabla' U_0(x')\cdot\nabla' V_\alpha^{(N)}(x',t)\mathrm{d}x' \\ = \int_\sigma V_\alpha^{(N)}(x',t)\mathrm{d}x' = F(t) - \alpha s_\alpha^{(N)}(t).\end{aligned} \tag{3.36}$$

Substituting (3.36) into (3.35) yields

$$\int_\sigma \left(V_\alpha^{(N)}\right)_t(x',t)U_0(x')\mathrm{d}x' + F(t) - \alpha s_\alpha^{(N)}(t) = s_\alpha^{(N)}(t)\kappa_0,$$

i.e.,

$$(\kappa_0+\alpha)s_\alpha^{(N)}(t) = \int_\sigma \left(V_\alpha^{(N)}\right)_t(x',t)U_0(x')\mathrm{d}x' + F(t). \tag{3.37}$$

Integrating (3.37) with respect to t from τ to $t_*+2\pi$ we obtain

$$\begin{aligned}(\kappa_0+\alpha)\int_\tau^{t_*+2\pi} s_\alpha^{(N)}(t)\mathrm{d}t = -(\kappa_0+\alpha)S^*_{s_\alpha^{(N)}}(\tau) \\ = -\int_\sigma V_\alpha^{(N)}(x',\tau)U_0(x')\mathrm{d}x' + \int_\tau^{t_*+2\pi} F(t)\mathrm{d}t.\end{aligned} \tag{3.38}$$

Here we have used the choice of the point t_*, that is

$$\int_\sigma V_\alpha^{(N)}(x',t_*)U_0(x')\mathrm{d}x' = \int_\sigma V_\alpha^{(N)}(x',t_*+2\pi)U_0(x')\mathrm{d}x' = 0.$$

and hence,

$$\int_\tau^{t_*+2\pi}\int_\sigma \left(V_\alpha^{(N)}\right)_t(x',t)U_0(x')\mathrm{d}x'\mathrm{d}t = -\int_\sigma V_\alpha^{(N)}(x',\tau)U_0(x')\mathrm{d}x'.$$

From (3.38) it follows that

$$
\begin{aligned}
&(\kappa_0+\alpha)^2\int\limits_{t_*}^{t_*+2\pi}\left|S^*_{s_\alpha^{(N)}}(\tau)\right|^2\mathrm{d}\tau\\
&\leqslant 2\int\limits_{t_*}^{t_*+2\pi}\left(\int\limits_\sigma V_\alpha^{(N)}(x',\tau)U_0(x')\mathrm{d}x'\right)^2\mathrm{d}\tau+2\int\limits_{t_*}^{t_*+2\pi}\left(\int\limits_\tau^{t_*+2\pi}F(t)\mathrm{d}t\right)^2\mathrm{d}\tau\\
&\leqslant 2\int\limits_{t_*}^{t_*+2\pi}\int\limits_\sigma\left|V_\alpha^{(N)}(x',\tau)\right|^2\mathrm{d}x'\int\limits_\sigma\left|U_0(x')\right|^2\mathrm{d}x'\mathrm{d}\tau+2\int\limits_{t_*}^{t_*+2\pi}|S_F^*(\tau)|^2\mathrm{d}\tau \qquad (3.39)\\
&\leqslant c\int\limits_{t_*}^{t_*+2\pi}\int\limits_\sigma\left|V_\alpha^{(N)}(x',\tau)\right|^2\mathrm{d}x'\int\limits_\sigma\left|\nabla' U_0(x')\right|^2\mathrm{d}x'\mathrm{d}\tau+2\int\limits_{t_*}^{t_*+2\pi}|S_F^*(\tau)|^2\mathrm{d}\tau\\
&\leqslant c\left(\int\limits_{t_*}^{t_*+2\pi}\int\limits_\sigma\left|V_\alpha^{(N)}(x',\tau)\right|^2\mathrm{d}x'\mathrm{d}\tau+\int\limits_{t_*}^{t_*+2\pi}|F(\tau)|^2\mathrm{d}\tau\right).
\end{aligned}
$$

Substituting (3.39) into (3.33) yields

$$
\int\limits_{t_*}^{t_*+2\pi}\int\limits_\sigma\left|V_\alpha^{(N)}(x',t)\right|^2\mathrm{d}x'\mathrm{d}t\leqslant c\varepsilon\int\limits_{t_*}^{t_*+2\pi}\int\limits_\sigma\left|V_\alpha^{(N)}(x',t)\right|^2\mathrm{d}x'\mathrm{d}t+c_\varepsilon\int\limits_{t_*}^{t_*+2\pi}\left|F(t)\right|^2\mathrm{d}t
$$

and choosing ε sufficiently small we obtain

$$
\int\limits_{t_*}^{t_*+2\pi}\int\limits_\sigma\left|V_\alpha^{(N)}(x',t)\right|^2\mathrm{d}x'\mathrm{d}t\leqslant c\int\limits_{t_*}^{t_*+2\pi}\left|F(t)\right|^2\mathrm{d}t. \qquad (3.40)
$$

The estimates (3.40) and (3.39) give

$$
\int\limits_{t_*}^{t_*+2\pi}\left|S^*_{s_\alpha^{(N)}}(\tau)\right|^2\mathrm{d}\tau\leqslant c\int\limits_{t_*}^{t_*+2\pi}\left|F(\tau)\right|^2\mathrm{d}\tau. \qquad (3.41)
$$

Finally from (3.34) and (3.41) it follows that

$$
\int\limits_{t_*}^{t_*+2\pi}\int\limits_\sigma\left|\nabla' S^*_{V_\alpha^{(N)}}(x',t)\right|^2\mathrm{d}x'\mathrm{d}t\leqslant c\int\limits_{t_*}^{t_*+2\pi}\left|F(t)\right|^2\mathrm{d}t. \qquad (3.42)
$$

The constants in (3.40)–(3.42) are independent of α and N. □

3.6 Convergence of the Galerkin approximations. Proof of Theorem 3.3.1

Proof of the existence. The constructed approximate solutions $(V_\alpha^{(N)}(x',t), s_\alpha^{(N)}(t))$ satisfy the equalities $(3.24)_1$. Multiplying these relations by arbitrary functions $d_k(t) \in L^2_{\wp}(0,2\pi)$ such that $d_k'(t) \in L^2_\sharp(0,2\pi)$, summing over k from $k=1$ to $k=M, M \leqslant N$, integrating with respect to t and then integrating by parts, we obtain the integral identity

$$\begin{aligned} &\int_0^{2\pi}\int_\sigma V_\alpha^{(N)}(x',t)\eta_t(x',t)\mathrm{d}x'\mathrm{d}t \\ &+\nu\int_0^{2\pi}\int_\sigma \nabla' S^*_{V_\alpha^{(N)}}(x',t)\cdot\nabla'\eta_t(x',t)\mathrm{d}x'\mathrm{d}t \\ &\qquad = \int_0^{2\pi} S^*_{s_\alpha^{(N)}}(\tau)\int_\sigma \eta_t(x',t)\mathrm{d}x'\mathrm{d}t \end{aligned} \tag{3.43}$$

for test functions η having the form $\eta(x',t) = \sum_{k=1}^{M} d_k(t)u_k(x')$.

Recall that $(V_\alpha^{(N)}(x',t), s_\alpha^{(N)}(t))$ obey the a priori estimate (3.27) with a constant c independent of α and N.

Since all functions in (3.27) are 2π-periodic, the inequality (3.27) is equivalent to

$$\begin{aligned} &\int_0^{2\pi}\int_\sigma \left|V_\alpha^{(N)}(x',t)\right|^2\mathrm{d}x'\mathrm{d}t + \int_0^{2\pi}\int_\sigma \left|\nabla' S^*_{V_\alpha^{(N)}}(x',t)\right|^2\mathrm{d}x'\mathrm{d}t \\ &\qquad + \int_0^{2\pi}\left|S^*_{s_\alpha^{(N)}}(\tau)\right|^2\mathrm{d}\tau \leqslant c\int_0^{2\pi}\left|F(\tau)\right|^2\mathrm{d}\tau. \end{aligned} \tag{3.44}$$

Let us fix N and choose a subsequences $\{\alpha_l\}$ and $\{(V_{\alpha_l}^{(N)}(x',t), s_{\alpha_l}^{(N)}(t))\}$ such that $\lim\limits_{l\to\infty}\alpha_l = 0$, $\{V_{\alpha_l}^{(N)}\}$ converges weakly in $L^2_\sharp(0,2\pi;L^2(\sigma))$ to some $V^{(N)}$, $\left\{S^*_{V_{\alpha_l}^{(N)}}\right\}$ converges weakly in $L^2_{\wp}(0,2\pi;\mathring{W}^{1,2}(\sigma))$ to $S_{V^{(N)}}$. Recall that for $U \in L^2_\sharp(0,T;L^2(\sigma))$, and S_U is the primitive of U. Moreover, $\left\{s_{\alpha_l}^{(N)}\right\}$ converges weakly in $W^{-1,2}_{\wp}(0,2\pi)$ to $s^{(N)}$. The last convergence means that

$$\lim_{l\to\infty}\int_0^{2\pi} S^*_{s_{\alpha_l}^{(N)}}(t)\eta'(t)\mathrm{d}t = \int_0^{2\pi} S_{s^{(N)}}(t)\eta'(t)\mathrm{d}t = \langle s^{(N)},\eta\rangle \quad \forall\eta\in W^{1,2}_{\wp}(0,2\pi),$$

where $s^{(N)} \in W_{\wp}^{-1,2}(0,2\pi)$ and $S_{s^{(N)}} \in L^2_{\sharp}(0,2\pi)$ is a primitive of $s^{(N)}$ in the distributional sense.

Obviously, for the limit functions $V^{(N)}$ and $S_{s^{(N)}}$, the estimate (3.44) remains valid with a constant c independent of N. In (3.43) taking $\alpha = \alpha_l$ and passing to the limit as $\alpha_l \to 0$, we get

$$\begin{aligned} &\int_0^{2\pi}\int_\sigma V^{(N)}(x',t)\eta_t(x',t)\mathrm{d}x'dt \\ &+\nu\int_0^{2\pi}\int_\sigma \nabla' S_{V^{(N)}}(x',t)\cdot\nabla'\eta_t(x',t)\mathrm{d}x'\mathrm{d}t \\ &= \int_0^{2\pi} S_{s^{(N)}}(\tau)\int_\sigma \eta_t(x',t)\mathrm{d}x'\mathrm{d}t. \end{aligned} \tag{3.45}$$

Let us show that $V^{(N)}(x',t)$ satisfy the flux condition:

$$\int_\sigma V^{(N)}(x',t)\mathrm{d}x' = F(t). \tag{3.46}$$

Integrating the equation $(3.24)_3$ for $\alpha = \alpha_l$ from t to 2π yields

$$\alpha_l S_{s_{\alpha_l}^{(N)}}(t) + \int_t^{2\pi}\int_\sigma V_{\alpha_l}^{(N)}(x',\tau)\mathrm{d}x'\mathrm{d}\tau = S_F(t). \tag{3.47}$$

Obviously, the sequence $\left\{\varphi_l^{(N)}(\tau) = \int_\sigma V_{\alpha_l}^{(N)}(x',\tau)\mathrm{d}x'\right\}$ is bounded in $L^2(0,2\pi)$. So we may assume, without loss of generality, that $\{\varphi_l^{(N)}\}$ is weakly convergent to $\varphi^{(N)}$ in $L^2(0,2\pi)$.

Then, the sequence of primitives $S_{\varphi_l^{(N)}}(t) = -\int_t^{2\pi}\varphi_l^{(N)}(\tau)\mathrm{d}\tau \to S_{\varphi^{(N)}}(t)$ for all $t \in [0,2\pi]$.

Hence $\left\|S_{\varphi_l^{(N)}} - S_{\varphi^{(N)}}\right\|_{L^2(0,2\pi)} \to 0$ as $l \to \infty$ $(\alpha_l \to 0)$.

From (3.47) we have

$$\left\|S_{\varphi_l^{(N)}} - S_F\right\|_{L^2(0,2\pi)} = \alpha_l \left\|S_{s_{\alpha_l}^{(N)}}\right\|_{L^2(0,2\pi)} \leqslant c\alpha_l \to 0 \quad \text{as } l \to \infty.$$

Therefore,

$$\int_t^{2\pi}\int_\sigma V^{(N)}(x',\tau)\mathrm{d}x'\mathrm{d}\tau = \int_t^{2\pi} F(\tau)\mathrm{d}\tau \quad \text{for a.a. } t\in[0,2\pi],$$

and differentiating this equality with respect to t we get (3.46).

Now we choose a subsequence $\{(V^{(N_k)}(x',t),\, s^{(N_k)}(t))\}$ such that $\{V^{(N_k)}\}$ converges weakly in $L^2_\sharp(0,2\pi;L^2(\sigma))$ to some V, $\{S_{V^{(N_k)}}\}$ converges weakly in $L^2_\wp(0,2\pi;\mathring{W}^{1,2}(\sigma))$ to S_V and $\{s^{(N_k)}\}$ converges weakly in $W^{-1,2}_\wp(0,2\pi)$ to s.

In (3.45) passing to the limit over the subsequence $N_k\to+\infty$, yields

$$\begin{aligned}\int_0^{2\pi}\int_\sigma V(x',t)\eta_t(x',t)\mathrm{d}x'\mathrm{d}t+\nu\int_0^{2\pi}\int_\sigma \nabla' S_V(x',t)\cdot\nabla'\eta_t(x',t)\mathrm{d}x'\mathrm{d}t\\ =\int_0^{2\pi} S_s(\tau)\int_\sigma \eta_t(x',t)\mathrm{d}x'\mathrm{d}t\end{aligned} \tag{3.48}$$

Exactly as above we can prove that $V(x',t)$ satisfies the flux condition (3.14). However, the integral identity (3.48) is proved, up to now, only for test functions η which can be represented as the sums:

$$\eta(x',t)=\sum_{k=1}^{M} d_k(t)u_k(x') \text{ with } d_k(t)\in L^2_\wp(0,2\pi) \text{ such that } d_k'(t)\in L^2_\sharp(0,2\pi).$$

After we have passed to the limit in (3.45) as $N_l\to+\infty$, the subscript M in these sums can be arbitrary large natural number. Such sums are dense in the space $\mathcal{V}=\{\eta:\eta\in L^2_\wp(0,2\pi;\mathring{W}^{1,2}(\sigma)),\, \eta_t\in L^2_\sharp(0,2\pi;L^2(\sigma))\}$. This can be proved exactly in the same way as it is done in the book [44] for the case of an initial boundary value problem. Thus, they also are dense in the subspace $\mathcal{V}_1=\{\eta:\eta\in L^2_\wp(0,2\pi;\mathring{W}^{1,2}(\sigma)),\, \eta_t\in L^2_\sharp(0,2\pi;W^{1,2}(\sigma))\}\subset\mathcal{V}$ and, therefore (3.45) remains valid for $\forall\,\eta\in\mathcal{V}_1$. This proves that $\big(V(x',t),\, s(t)\big)$ satisfies the integral identity (3.15) and thus it is a weak solution of the problem (3.10). The estimate (3.16) for $\big(V(x',t),\, s(t)\big)$ follows from the estimate (3.44) for the approximate solutions.

□

Proof of the uniqueness. Assume that $F(t)=0$. We have $\eta_t \in L^2_\sharp(0,2\pi;W^{1,2}(\sigma))$, consider

$$\eta(x',t)=\int_t^{2\pi}\big(S_V(x',\tau)-\bar{S}_V(x')\big)\mathrm{d}\tau$$
$$=\int_t^{2\pi}\Big(-\int_\tau^{2\pi}V(x',\mu)\mathrm{d}\mu+\frac{1}{2\pi}\int_0^{2\pi}\int_t^{2\pi}V(x',\mu)\mathrm{d}\mu\mathrm{d}t\Big)\mathrm{d}\tau.$$

Obviously, $\eta\in\mathcal{V}_1$. Putting this η into the integral identity (3.15), we obtain

$$\begin{aligned}&\int_0^{2\pi}\int_\sigma V(x',t)\big(S_V(x',t)-\bar{S}_V(x')\big)\,\mathrm{d}x'\mathrm{d}t\\ &+\nu\int_0^{2\pi}\int_\sigma \nabla' S_V(x',t)\cdot\nabla'\big(S_V(x',t)-\bar{S}_V(x')\big)\,\mathrm{d}x'\mathrm{d}t\\ &=\int_0^{2\pi}S_s(t)\int_\sigma\big(S_V(x',t)-\bar{S}_V(x')\big)\,\mathrm{d}x'\mathrm{d}t.\end{aligned}\tag{3.49}$$

Since

$$\int_\sigma V(x',t)\,\mathrm{d}x'=F(t)=0,$$

by Fubini's theorem and the time-periodicity of the function $V(x',t)$, we have

$$\int_\sigma\big(S_V(x',t)-\bar{S}_V(x')\big)\mathrm{d}x'=\int_\sigma\Big(-\int_t^{2\pi}V(x',\tau)\,\mathrm{d}\tau\Big)\mathrm{d}x'$$
$$+\frac{1}{2\pi}\int_\sigma\Big(\int_0^{2\pi}\int_t^{2\pi}V(x',\tau)\,\mathrm{d}\tau\mathrm{d}t\Big)\mathrm{d}x'$$
$$=-\int_t^{2\pi}\Big(\int_\sigma V(x',\tau)\,\mathrm{d}x'\Big)\mathrm{d}\tau+\frac{1}{2\pi}\int_0^{2\pi}\int_t^{2\pi}\Big(\int_\sigma V(x',\tau)\,\mathrm{d}x'\Big)\mathrm{d}\tau\mathrm{d}t=0;$$

$$\int_0^{2\pi}\int_\sigma V(x',t)\big(S_V(x',t)-\bar{S}_V(x')\big)\,\mathrm{d}x'\mathrm{d}t=\frac{1}{2}\int_0^{2\pi}\frac{d}{dt}\int_\sigma|S_V(x',t)|^2\mathrm{d}t$$
$$-\frac{1}{2}\int_0^{2\pi}\frac{d}{dt}\int_\sigma S_V(x',t)\bar{S}_V(x')\mathrm{d}x\mathrm{d}t=0;$$

$$\int_0^{2\pi}\int_\sigma \nabla' S_V(x',t)\cdot\nabla'\big(S_V(x',t)-\bar S_V(x')\big)\,\mathrm{d}x'\mathrm{d}t$$
$$=\int_0^{2\pi}\int_\sigma |\nabla'\big(S_V(x',t)-\bar S_V(x')\big)|^2\,\mathrm{d}x'\mathrm{d}t$$
$$+\int_0^{2\pi}\int_\sigma \nabla'\bar S_V(x')\cdot\big(S_V(x',t)-\bar S_V(x')\big)\,\mathrm{d}x'\mathrm{d}t$$
$$=\int_0^{2\pi}\int_\sigma |\nabla'\big(S_V(x',t)-\bar S_V(x')\big)|^2\mathrm{d}x'\mathrm{d}t$$
$$-\int_\sigma \nabla'\bar S_V(x')\cdot\nabla'\bigg(\int_0^{2\pi}\Big(S_V(x',t)-\bar S_V(x')\Big)\bigg)\mathrm{d}t\,\mathrm{d}x'$$
$$=\int_0^{2\pi}\int_\sigma |\nabla'\big(S_V(x',t)-\bar S_V(x')\big)|^2\,\mathrm{d}x'\mathrm{d}t.$$

Therefore, from (3.49) it follows that

$$\int_0^{2\pi}\int_\sigma |\nabla'\big(S_V(x',t)-\bar S_V(x')\big)|^2\,\mathrm{d}x'\mathrm{d}t=0.$$

Then $\nabla'\big(S_V(x',t)-\bar S_V(x')\big)=0$ and, hence, $S_V(x',t)-\bar S_V(x')=m(t)$. Integrating over σ we get

$$|\sigma|m(t)=-\int_\sigma\int_t^{2\pi} V(x',\tau)\mathrm{d}\tau\mathrm{d}x'+\frac{1}{2\pi}\int_\sigma\int_0^{2\pi}\int_\tau^{2\pi} V(x',\mu)\mathrm{d}\mu\mathrm{d}\tau\mathrm{d}x'$$
$$=-\int_t^{2\pi}\Big(\int_\sigma V(x',\tau)\mathrm{d}x'\Big)\mathrm{d}\tau+\frac{1}{2\pi}\int_0^{2\pi}\int_\tau^{2\pi}\Big(\int_\sigma V(x',\mu)\mathrm{d}x'\Big)\mathrm{d}\mu\mathrm{d}\tau=0.$$

Thus, $S_V(x',t)=\bar S_V(x')$, and since $S_V(x',0)=S_V(x',2\pi)=0$, we conclude that $S_V(x',t)=0$ for a.a $(x',t)\in\sigma\times[0,2\pi]$, that is $\int_t^{2\pi}V(x',\tau)\mathrm{d}\tau=0$ for a.a. x' and t. This implies $V(x',t)=0$.

From the identity (3.15) it follows that

$$\int_0^{2\pi} S_s(t)\int_\sigma \eta_t(x',t)\mathrm{d}t=0\quad\forall\eta\in\mathcal{V}_1. \tag{3.50}$$

In (3.50) we take $\eta=b(t)U_0(x')$, where $b\in W^{1,2}_\wp(0,2\pi)$ is arbitrary and $U_0(x')$ is the solution of problem (3.7). Recall that $\int_\sigma U_0(x')\mathrm{d}x'=\kappa_0\neq 0$.

Then (3.50) takes the form

$$\int_0^{2\pi} S_s(t) \int_\sigma \eta_t(x', t) \mathrm{d}t = \kappa_0 \int_0^{2\pi} S_s(t) b'(t) \mathrm{d}t = 0 \quad \forall b \in W^{1,2}_{\wp}(0, 2\pi).$$

Thus, $S_s(t) = const$. Since $S_s \in L^2_\sharp(0, 2\pi)$, i.e., the mean value of $S_s(t)$ is equal to zero, we get that $S_s(t) = 0$. Therefore, the functional $s = 0$. □

Chapter 4

Poiseuille-Type Approximations for Axisymmetric Flow in a Thin Tube with Thin Stiff Elastic Wall

4.1 Introduction

The interaction between a fluid and an elastic wall arises in many real-life applications like engineering and biology. The corresponding mathematical model is represented by the fluid–structure interaction (FSI) problem, coupling two media with different, often highly contrasting physical characteristics. The wall can be modeled either by a two dimensional shell or by a three dimensional solid body; the stiffness of the wall is finite. The stiffness of the wall as a large parameter was considered in [60], [61] and [62] by G. Panasenko, Y. Sirakov and R. Stavre, where the fluid–plate and fluid–cylindric wall interactions were studied, and the wall was modeled by a special boundary condition. In [49], [64], [65] by I. Malakhova-Ziablova, G. Panasenko and R. Stavre the wall was modeled by the elasticity equation in two or three dimensions as a thin plate or thin cylindric layer, but the fluid domain was not thin. The asymptotic behavior of the solution when both the thickness of the wall and the diameter of the pipe are small parameters, and the wall has high stiffness, was first considered in [66] by G. Panasenko and R. Stavre. Note that this setting is crucial for understanding an analog of a Poiseuille flow in a tube with an elastic wall.

The goal of this Chapter is to study FSI problem in a cylinder surrounded by a stiff elastic wall. We take the model proposed by G. Panasenko and R. Stavre in [65], [66] and we obtain from it a 4^{th} order simplified PDE which depends only on one space variable and time and describes the fluid flow in a pipe surrounded by an elastic wall as accurately as Navier–Stokes model coupled with FSI. Subsequently, we make a comparative analysis of a numerical solution (without swirl [1]) to the full Navier–Stokes equations and to the derived 4^{th} order simplified PDE in two geometries: a cylinder and a Y-shaped network of cylinders. Remarkably, in the case when the difference in prescribed velocities between inlet and outlet of the cylinder is small, the solutions on cross sections of a cylinder obtained from the both approaches do not show a significant difference. Notably, the solution of the 4^{th} order PDE demands less computational time, resulting in resource savings.

4.2 Problem formulation

Consider a fluid occupying the interior of a thin cylindrical tube with an elastic wall (as shown in Figure 4.1). We define ε_1 as the radius of the fluid domain, ε as the thickness of the elastic wall, the length of the tube equals to one. The ratio between the radius of the fluid domain and the thickness of the wall must be at least greater than 10, the ratio between the length of the tube and the radius of the tube must be also at least greater than 10, i.e.

$$\varepsilon << \varepsilon_1 << 1. \tag{4.1}$$

Let us denote the fluid domain by

$$C^f = \{(x_1, x_2, x_3) \in \mathbb{R}^3 : x_1^2 + x_2^2 < \varepsilon_1^2, x_3 \in \mathbb{R}\},$$

and the domain of an elastic wall by

$$C_\varepsilon^e = \{(x_1, x_2, x_3) \in \mathbb{R}^3 : \varepsilon_1^2 < x_1^2 + x_2^2 < (\varepsilon_1 + \varepsilon)^2, x_3 \in \mathbb{R}\}.$$

Supposing that the coupled problem is axisymmetric and denoting $r = \sqrt{x_1^2 + x_2^2}$, we convert C^f into L^f and C_ε^e into L_ε^e in cylindrical coordinate

1. The idea is that this symmetry reduces the number of degrees of freedom in the domain to two (the radial and the longitudial, but not the angular coordinate), so that this approach simplifies computations

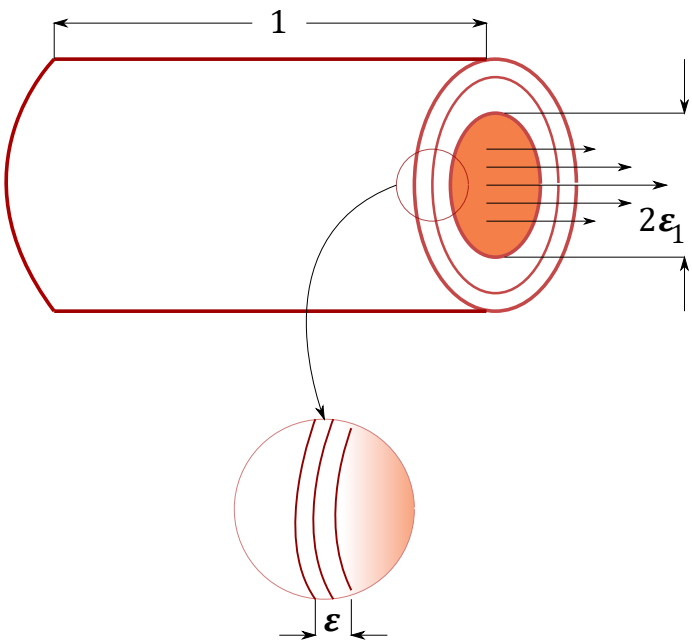

Figure 4.1 – A thin tube with radius ε_1, covered by elastic wall of thickness ε.

form:

$$L^f = \{(x_3, r) \in \mathbb{R}^2 : x_3 \in \mathbb{R}, r \in (0, \varepsilon_1)\},$$

$$L^e_\varepsilon = \{(x_3, r) \in \mathbb{R}^2 : x_3 \in \mathbb{R}, r \in (\varepsilon_1, \varepsilon_1 + \varepsilon)\}.$$

Let us denote by

$$F^0 = \{(x_3, 0) : x_3 \in \mathbb{R}\}$$

the axis of symmetry of the tube, by

$$F^{\varepsilon_1} = \{(x_3, \varepsilon_1) : x_3 \in \mathbb{R}\}$$

the boundary of the fluid domain and the internal part of the elastic wall (the coupling boundary), and by

$$F^{\varepsilon_1+\varepsilon} = \{(x_3, \varepsilon_1 + \varepsilon) : x_3 \in \mathbb{R}\}$$

the external boundary of the elastic wall.

The characteristics of the elastic wall are represented by the variable density $\tilde{\rho}_e = \tilde{\rho}_e(\xi)$ depending on the radius of the tube and by the matrix-valued coefficients $\tilde{A}_{ij} = \tilde{A}_{ij}(\xi), i,j \in \{1,2,3\}$ which depend on the Young's modulus $\tilde{E} = \tilde{E}(\xi)$ and on the Poisson's ratio $\hat{\nu} = \hat{\nu}(\xi)$, with $\xi = \dfrac{r-\varepsilon_1}{\varepsilon}$, $r \in (\varepsilon_1, \varepsilon_1 + \varepsilon)$. Since the density and the Young's modulus characterizing a solid phase (the elastic wall) may be very different from a material to another, it is interesting to analyze the changes of the mathematical model with respect to these physical characteristics. For this purpose, in [66] G. Panasenko and R. Stavre introduced two additional parameters related to ε:

$$\omega_\rho = \varepsilon^\alpha,\ \omega_E = \varepsilon^\beta,\ \text{with } \alpha, \beta \in \mathbb{R} \tag{4.2}$$

and supposed that the density of the elastic tube is of order ω_ρ and its Young's modulus is of order ω_E, while the characteristic time, the dynamic viscosity and the density of the fluid are supposed to be scaled so that they are of order one. So, $\tilde{\rho}_e = \omega_\rho \rho_e$ and $\tilde{E} = \omega_E E$, with ρ_e and E of order one. With respect to the physical characteristics of the elastic wall, in [66] the following assumptions were imposed:

$$\omega_\rho \leqslant \omega_E; \quad \varepsilon^{-1} \leqslant \omega_E. \tag{4.3}$$

Moreover, with respect to the magnitude of ω_E, in [66] the following different cases were considered:

1) $\varepsilon^{-1} \leqslant \omega_E << \varepsilon^{-1}\varepsilon_1^{-2}$;

2) $\omega_E = \varepsilon^{-1}\varepsilon_1^{-2}$;

3) $\varepsilon^{-1}\varepsilon_1^{-2} << \omega_E << \varepsilon^{-1}\varepsilon_1^{-3}$;

4) $\omega_E = \varepsilon^{-1}\varepsilon_1^{-3}$;

5) $\omega_E >> \varepsilon^{-1}\varepsilon_1^{-3}$.

In most practical applications, the relation between the density of an elastic wall and its Young's modulus is $\omega_\rho << \omega_E$. However, in order to simplify the illustration, we start with the relation

$$\omega_\rho = \omega_E; \tag{4.4}$$

and then, we pass to the case

$$\omega_\rho << \omega_E. \tag{4.5}$$

Furthermore, in [66] G. Panasenko and R. Stavre showed that there is a major difference between the cases (4.4) and (4.5).

Consider the stiffness matrices $\tilde{A}_{ij}$ having the elements $\tilde{A}_{ij} = (\tilde{a}_{ij}^{kl})_{1\leq k,l\leq 3}$ which satisfy the relations

$$\tilde{a}_{ij}^{kl} = \omega_E a_{ij}^{kl},$$

$$a_{ij}^{kl} = \frac{E}{2(1+\hat{\nu})}\left(\frac{2\hat{\nu}}{1-2\hat{\nu}}\delta_{ik}\delta_{jl} + \delta_{ij}\delta_{kl} + \delta_{il}\delta_{jk}\right),$$

with the properties:

(i) $a_{ij}^{kl}(\xi) = a_{kj}^{il}(\xi) = a_{ji}^{lk}(\xi), \forall i,j,k,l \in \{1,2,3\}, \forall \xi \in [0,1]$,

(ii) $\exists\ \kappa > 0$ independent of $\varepsilon, \varepsilon_1$ such that

$$\sum_{i,j,k,l=1}^{3} a_{ij}^{kl}(\xi)\eta_j^l\eta_i^k \geq \kappa \sum_{j,l=1}^{3} (\eta_j^l)^2, \forall \xi \in [0,1], \forall \eta = (\eta_j^l)_{1\leq j,l\leq 3}, \text{ with } \eta_j^l = \eta_l^j.$$

The functions $\rho_e, \hat{\nu}, E$ are supposed to be piecewise-smooth and ρ_e satisfies the following condition

$$\begin{aligned} &\exists m_\rho, M_\rho \text{ independent of } \varepsilon, \varepsilon_1, 0 < m_\rho < M_\rho, \text{ such that} \\ &\qquad m_\rho \leq \rho_e(\xi) \leq M_\rho, \forall \xi \in [0,1]. \end{aligned} \tag{4.6}$$

So, the wall can be a natural laminate which is the case of blood vessels. The characteristics of the viscous fluid, independent of $\varepsilon, \varepsilon_1$, are the positive constants ρ_f and ν representing its density and its dynamic viscosity, respectively. They are supposed to be of order one.

In addition to the coefficients $\rho_e, E, \hat{\nu}$ (for the elastic wall) and ρ_f, ν (for the viscous fluid), we also consider as data of the problem the forces $\mathbf{g}$ and $\mathbf{f}$ which represent an external action on the elastic wall and on the fluid, respectively. In the case of blood vessels, it corresponds to the action of the surrounding tissues.

The mathematical model of the periodic, axisymmetric, time dependent interaction between an incompressible, Stokes fluid and a cylindrical, stratified [1] tube with elastic wall uses the following notation and expressions for:

— the linear elasticity operator

$$L\mathbf{u}\cdot\mathbf{e}_3 = \frac{\partial}{\partial x_3}\left((\lambda+2\mu)\frac{\partial u_3}{\partial x_3}+\lambda\left(\frac{\partial u_r}{\partial r}+\frac{1}{r}u_r\right)\right) + \frac{\partial}{\partial r}\left(\mu\left(\frac{\partial u_3}{\partial r}+\frac{\partial u_r}{\partial x_3}\right)\right)+\frac{\mu}{r}\left(\frac{\partial u_3}{\partial r}+\frac{\partial u_r}{\partial x_3}\right),$$

$$L\mathbf{u}\cdot\mathbf{e}_r = \frac{\partial}{\partial x_3}\left(\mu\left(\frac{\partial u_3}{\partial r}+\frac{\partial u_r}{\partial x_3}\right)\right)+\frac{\partial}{\partial r}\left(\lambda\left(\frac{\partial u_3}{\partial x_3}+\frac{1}{r}u_r\right) +(\lambda+2\mu)\frac{\partial u_r}{\partial r}\right)+\frac{2\mu}{r}\left(\frac{\partial u_r}{\partial r}-\frac{1}{r}u_r\right),$$

— the divergence operator for a vector-valued function and a symmetric tensor-valued function

$$\mathrm{div}_c\mathbf{u} = \frac{\partial u_3}{\partial x_3}+\frac{\partial u_r}{\partial r}+\frac{1}{r}u_r,$$

$$\mathrm{div}_c S = \left(\frac{\partial S_{33}}{\partial x_3}+\frac{1}{r}\frac{\partial}{\partial r}(rS_{r3})\right)\mathbf{e}_3 + \left(\frac{\partial S_{3r}}{\partial x_3}+\frac{1}{r}\frac{\partial}{\partial r}(rS_{rr})-\frac{S_{\theta\theta}}{r}\right)\mathbf{e}_r,$$

— the gradient operator for a vector-valued function

$$\nabla_c\mathbf{u} = \begin{pmatrix} \dfrac{\partial u_3}{\partial x_3} & 0 & \dfrac{\partial u_3}{\partial r} \\ 0 & \dfrac{1}{r}u_r & 0 \\ \dfrac{\partial u_r}{\partial x_3} & 0 & \dfrac{\partial u_r}{\partial r} \end{pmatrix},$$

— the velocity strain tensor

$$D_c(\mathbf{u}) = \frac{1}{2}\left(\nabla_c\mathbf{u}+(\nabla_c\mathbf{u})^T\right).$$

1. The tube contains an elastic and fluid domains (see 4.1).

Here (x_3, r, θ) are the cylindrical coordinates, $\mathbf{e}_3$ and $\mathbf{e}_r$ are the unit vectors of Ox_3 and Or axes, respectively, $\mathbf{u}$ represents a vector function, S represents a tensorial axisymmetric function and

$$\lambda = \frac{E\hat{\nu}}{(1+\hat{\nu})(1-2\hat{\nu})}, \quad \mu = \frac{E}{2(1+\hat{\nu})}$$

are Lamé parameters, E is Young modulus and $\hat{\nu}$ is Poisson ratio.

In cylindrical coordinates the velocity strain tensor can be expressed as follows:

$$D_c(\mathbf{u}) = \begin{pmatrix} \dfrac{\partial u_3}{\partial x_3} & \dfrac{1}{2}\left(\dfrac{\partial u_3}{\partial r} + \dfrac{\partial u_r}{\partial x_3}\right) \\ \dfrac{1}{2}\left(\dfrac{\partial u_3}{\partial r} + \dfrac{\partial u_r}{\partial x_3}\right) & \dfrac{\partial u_r}{\partial r} \end{pmatrix}. \tag{4.7}$$

The mathematical model describing the fluid-elastic structure interaction is given by (see [66]) :

$$\begin{cases} \omega_\rho \rho_e \dfrac{\partial^2 \mathbf{u}}{\partial t^2} - \omega_E L\mathbf{u} = \varepsilon^{-1}\mathbf{g} & \text{in } L^e_\varepsilon \times (0,T), \\ \begin{cases} \rho_f \dfrac{\partial \mathbf{v}}{\partial t} - 2\nu \mathrm{div}_c D_c(\mathbf{v}) + \nabla p = \mathbf{f} \\ \mathrm{div}_c \mathbf{v} = 0 \end{cases} & \text{in } L^f \times (0,T), \\ v_r = 0 & \text{on } F^0 \times (0,T), \\ \begin{cases} \dfrac{\partial u_3}{\partial r} + \dfrac{\partial u_r}{\partial x_3} = 0 \\ \lambda(1)\dfrac{\partial u_3}{\partial x_3} + (\lambda(1) + 2\mu(1))\dfrac{\partial u_r}{\partial r} \\ + \dfrac{\lambda(1)}{\varepsilon_1 + \varepsilon} u_r = 0 \end{cases} & \text{on } F^{\varepsilon_1+\varepsilon} \times (0,T), \\ \begin{cases} \mathbf{v} = \dfrac{\partial \mathbf{u}}{\partial t} \\ \nu\left(\dfrac{\partial v_3}{\partial r} + \dfrac{\partial v_r}{\partial x_3}\right) = \omega_E \mu(0)\left(\dfrac{\partial u_3}{\partial r} + \dfrac{\partial u_r}{\partial x_3}\right) \\ -p + 2\nu \dfrac{\partial v_r}{\partial r} = \omega_E\Big(\lambda(0)\dfrac{\partial u_3}{\partial x_3} + (\lambda(0) \\ + 2\mu(0))\dfrac{\partial u_r}{\partial r} + \dfrac{\lambda(0)}{\varepsilon_1} u_r\Big) \end{cases} & \text{on } F^{\varepsilon_1} \times (0,T), \\ \mathbf{u}, \mathbf{v}, p & 1-\text{periodic in } x_3, \\ \mathbf{u}(0) = \dfrac{\partial \mathbf{u}}{\partial t}(0) = \mathbf{0} & \text{in } L^e_\varepsilon, \\ \mathbf{v}(0) = \mathbf{0} & \text{in } L^f. \end{cases} \tag{4.8}$$

Note that in (4.8) the time interval $(0,T)$ can be chosen arbitrarily, independently of $\varepsilon, \varepsilon_1$.

In [66] G. Panasenko and R. Stavre constructed a complete asymptotic expansion of the solution to (4.8). Furthermore, the leading term of this expansion was computed as some analogue of the Poiseuille flow for tubes with elastic walls. In general, the classical Poiseuille flow is defined as a flow with a given pressure drop at the ends of a tube. Since $\mathbf{u}, \mathbf{v}, p$ are 1–periodic in x_3 the problem (4.8) does not include such a case.

However, such a pressure drop can be constructed in a middle of a tube, i.e. we can take two sufficiently close cross sections of a tube and consider the difference of pressure on them as a pressure drop. Then the leading term of the asymptotic expansion of the solution can be interpreted as a Poiseuille type flow, the velocity of the fluid and the displacements of the walls are expressed via three basic functions depending on the normal variable and time only:

a) the scaled average velocity Q, the averaged velocity is equal to $2\varepsilon_1^2 Q$;

b) the longitudinal displacement of the wall-fluid interface w_3 ($\mathbf{w}$ is the displacement of the wall-fluid interface containing two components w_r and w_3);

c) the leading term for the pressure q.

Moreover, in [66] G. Panasenko and R. Stavre derived the relation between the leading term for pressure q and the scaled average velocity Q described by the equation

$$\frac{\partial q}{\partial x_3}(x_3,t) + 16\nu Q(x_3,t) = f_3, \tag{4.9}$$

where f_3 is a longitudial external force which represents action on a fluid. So, it follows from (4.9), that we can consider only two independent basic functions q and Q of the leading term in the asymptotic expansion.

Below the expressions obtained in [66] of the longitudial and radial velocities of the fluid, pressure, longitudial and radial velocities of the elastic wall are listed:

$$
\begin{aligned}
v_3(x_3,r,t) &= 4\varepsilon_1^2\left(1-\frac{r^2}{\varepsilon_1^2}\right)Q(x_3,t)\\
&+\frac{\partial w_3}{\partial t}(x_3,t)+\frac{\varepsilon_1^2}{4}\left(1-\frac{r^2}{\varepsilon_1^2}\right)\left(-\frac{\rho_f}{\nu}\frac{\partial^2 w_3}{\partial t^2}(x_3,t)+\frac{\partial^3 w_3}{\partial t\partial x_3^2}(x_3,t)\right),\\
v_r(x_3,r,t) &= -\varepsilon_1^3\frac{r}{\varepsilon_1}\Big(2-\frac{r^2}{\varepsilon_1^2}\Big)\frac{\partial Q}{\partial x_3}(x_3,t)-\varepsilon_1\frac{r}{2\varepsilon_1}\frac{\partial^2 w_3}{\partial t\partial x_3}(x_3,t)\\
&-\frac{\varepsilon_1^3}{16}\frac{r}{\varepsilon_1}\left(2-\frac{r^2}{\varepsilon_1^2}\right)\left(-\frac{\rho_f}{\nu}\frac{\partial^3 w_3}{\partial t^2\partial x_3}(x_3,t)+\frac{\partial^4 w_3}{\partial t\partial x_3^3}(x_3,t)\right),\\
p(x_3,r,t) &= q(x_3,t),\\
u_3(x_3,r,t) &= w_3(x_3,t)+\varepsilon\frac{r-\varepsilon_1}{\varepsilon}\left(\varepsilon_1^3\int_0^t\frac{\partial^2 Q}{\partial x_3^2}(x_3,\theta)\mathrm{d}\theta\right.\\
&\left.+\frac{\varepsilon_1}{2}\frac{\partial^2 w_3}{\partial x_3^2}(x_3,t)\right)-\nu\omega_E^{-1}\varepsilon\varepsilon_1\left(\int_0^{\frac{r-\varepsilon_1}{\varepsilon}}\frac{1-\tau}{\mu(\tau)}\mathrm{d}\tau\right)\\
&\times\left(8Q(x_3,t)-\frac{\rho_f}{2\nu}\frac{\partial^2 w_3}{\partial t^2}(x_3,t)+\frac{\partial^3 w_3}{\partial t\partial x_3^2}(x_3,t)\right),\qquad(4.10)\\
u_r(x_3,r,t) &= -\varepsilon_1^3\left(1-\varepsilon\int_0^{\frac{r-\varepsilon_1}{\varepsilon}}\frac{1}{\varepsilon_1+\varepsilon\tau}\frac{\lambda(\tau)}{\lambda(\tau)+2\mu(\tau)}\mathrm{d}\tau\right)\\
&\times\int_0^t\frac{\partial Q}{\partial x_3}(x_3,\theta)\mathrm{d}\theta-\left(\frac{\varepsilon_1}{2}\Big(1-\varepsilon\int_0^{\frac{r-\varepsilon_1}{\varepsilon}}\frac{1}{\varepsilon_1+\varepsilon\tau}\frac{\lambda(\tau)}{\lambda(\tau)+2\mu(\tau)}\mathrm{d}\tau\Big)\right.\\
&\left.+\varepsilon\int_0^{\frac{r-\varepsilon_1}{\varepsilon}}\frac{\lambda(\tau)}{\lambda(\tau)+2\mu(\tau)}\mathrm{d}\tau\right)\frac{\partial w_3}{\partial x_3}(x_3,t)\\
&+\omega_E^{-1}\varepsilon\left(\int_0^{\frac{r-\varepsilon_1}{\varepsilon}}\frac{1-\tau}{\lambda(\tau)+2\mu(\tau)}\mathrm{d}\tau\right)\left(2\nu\varepsilon_1^2\frac{\partial Q}{\partial x_3}(x_3,t)\right.\\
&\left.-\nu\frac{\partial^2 w_3}{\partial t\partial x_3}(x_3,t)-q(x_3,t)\right).
\end{aligned}
$$

Here, for the leading terms, we keep the same notation as for the exact solution.

The radial displacement of the wall-fluid interface w_r is approximately

related with the third basic function w_3 by equation

$$w_r(x_3,t) = -\varepsilon_1^3 \int_0^t \frac{\partial Q}{\partial x_3}(x_3,\tau)\mathrm{d}\tau - \frac{\varepsilon_1}{2}\frac{\partial w_3}{\partial x_3}(x_3,t) \tag{4.11}$$

or

$$\frac{\partial w_r}{\partial t}(x_3,t) = -\varepsilon_1^3 \frac{\partial Q}{\partial x_3}(x_3,t) - \frac{\varepsilon_1}{2}\frac{\partial^2 w_3}{\partial t \partial x_3}(x_3,t). \tag{4.12}$$

For a continuous approximation of the velocity at the wall-fluid interface, in [66] the following approximation of u_r was derived:

$$u_r(x_3,t) = -\frac{\varepsilon_1^3}{16}\left(-\frac{\rho_f}{\nu}\frac{\partial^2 w_3}{\partial t \partial x_3}(x_3,t) + \frac{\partial^3 w_3}{\partial x_3^3}(x_3,t)\right).$$

Relations (4.10), (4.9) with basic functions Q and w_3 can be used as an ansatz in the frame of the method of asymptotic partial decomposition of the domain (MAPDD) for the three-dimensional problem of the Stokes or Navier–Stokes equations in a network of vessels with elastic walls (see [49],[63]). This approach allows to reduce dimension to one in all cylindrical parts of the network and reduces the computational costs.

4.3 The variational framework of the problem

In the first part of this section we define the functional spaces we are dealing with. Since our functions are 1-periodic with respect to x_3, we consider the fluid motion in the 3D domain

$$\Omega^f = \{(x_1,x_2,x_3) \in \mathbb{R}^3 : x_1^2 + x_2^2 < \varepsilon_1^2,\, x_3 \in (0,1)\},$$

and the domain for the equation of the elastic wall is

$$\Omega_\varepsilon^e = \{(x_1,x_2,x_3) \in \mathbb{R}^3 : \varepsilon_1^2 < x_1^2 + x_2^2 < (\varepsilon_1+\varepsilon)^2,\, x_3 \in (0,1)\}.$$

Since the coupled problem is axisymmetric and, as mentioned before $r = \sqrt{x_1^2+x_2^2}$, we denote D^f which means the domain to Ω^f in cylindrical coordinates

$$D^f = \{(x_3,r) \in \mathbb{R}^2 : x_3 \in (0,1),\, r \in (0,\varepsilon_1)\},$$

and D_ε^e which represents Ω_ε^e in cylindrical coordinates

$$D_\varepsilon^e = \{(x_3,r) \in \mathbb{R}^2 : x_3 \in (0,1),\, r \in (\varepsilon_1,\varepsilon_1+\varepsilon)\}.$$

Furtermore, we denote the axis of symmetry of the tube by

$$\Gamma^0 = \{(x_3, 0) : x_3 \in (0,1)\}.$$

The boundary of the fluid domain and the internal part of the elastic wall we denote by

$$\Gamma^{\varepsilon_1} = \{(x_3, \varepsilon_1) : x_3 \in (0,1)\},$$

and the external boundary of the elastic wall is

$$\Gamma^{\varepsilon_1+\varepsilon} = \{(x_3, \varepsilon_1+\varepsilon) : x_3 \in (0,1)\}.$$

In the fluid domain we consider the following function spaces

$$\begin{aligned}
L^2(D^f) &= \{\boldsymbol{\psi} : D^f \mapsto \mathbb{R}^2 : \int\limits_{D^f} r\,\boldsymbol{\psi}^2(x_3, r)\mathrm{d}x_3\mathrm{d}r < \infty\},\\
W^{1,2}(D^f) &= \{\boldsymbol{\psi} \in L^2(D^f) : \int\limits_{D^f} r|\nabla_c \boldsymbol{\psi}|^2(x_3, r)\mathrm{d}x_3\mathrm{d}r < \infty\},\\
\mathring{W}^{1,2}(D^f) &= \{\boldsymbol{\psi} \in W^{1,2}(D^f) : r\boldsymbol{\psi} = 0 \text{ on } \Gamma^{\varepsilon_1}\},\\
W^{2,2}(D^f) &= \{\boldsymbol{\psi} \in W^{1,2}(D^f) : \int\limits_{D^f} r|\nabla_c^2 \boldsymbol{\psi}|^2(x_3, r)\mathrm{d}x_3\mathrm{d}r < \infty\},
\end{aligned} \tag{4.13}$$

where

$$\begin{aligned}
|\nabla_c^2 \boldsymbol{\psi}|^2 = &\left(\frac{\partial^2 \psi_3}{\partial x_3^2}\right)^2 + \left(\frac{\partial^2 \psi_3}{\partial r^2}\right)^2 + 2\left(\frac{\partial^2 \psi_3}{\partial x_3 \partial r}\right)^2 + \left(\frac{\partial^2 \psi_r}{\partial x_3^2}\right)^2 + \left(\frac{\partial^2 \psi_r}{\partial r^2}\right)^2\\
&+2\left(\frac{\partial^2 \psi_r}{\partial x_3 \partial r}\right)^2 + \frac{1}{r^2}\left(\left(\frac{\partial \psi_3}{\partial r}\right)^2 + 2\left(\frac{\partial \psi_r}{\partial x_3}\right)^2 + 3\left(\frac{\partial \psi_r}{\partial r} - \frac{1}{r}\psi_r\right)^2\right).
\end{aligned}$$

Since we deal with 1-periodic in x_3 functions, we also need the definition of corresponding spaces.

Let $D(\mathbb{R}^1)$ be a Hilbert space of functions defined on $\mathbb{R}^1$. By $D_{per}(\mathbb{R}^1)$ we denote the subspace of $1-$periodic with respect to x_3 functions in $D(\mathbb{R}^1)$.

Then we define Lebesgue and Sobolev spaces of 1-periodic functions in the following way:

$L^2_{per}(D^f) = \{h \in L^2(D^f) : h(x_3) = h(x_3+1)\ \forall x_3 \in \mathbb{R}^1\}$.

$W^{l,2}_{per}(D^f) = \{h \in W^{l,2}(D^f) : h(x_3) = h(x_3+1)\ \forall x_3 \in \mathbb{R}^1\}$.

The space of the traces of functions from $W^{l,2}_{per}(D^f)$ is denoted by $W^{l-1/2,2}_{per}(\partial D^f)$. If we are interested only in the properties of functions on a subset $\Gamma \subset \partial D^f$, we shall write $W^{l-1/2,2}_{per}(\Gamma)$, for l integer, $l \geqslant 1$.

The space $W_{per}^{-1/2,2}(\Gamma)$ represents the dual of the subspace of $W_{per}^{1/2,2}(\partial D^f)$ which contains functions that vanish on $\partial D^f \backslash \Gamma$.

Denote also:

$$\begin{aligned}
U_{per}^{1,2}(D_\varepsilon^e) &= \{\boldsymbol{\varphi} \in W_{per}^{1,2}(D_\varepsilon^e) : \int_0^1 \varphi_r(x_3,1)\mathrm{d}x_3 = 0\},\\
V_{per}^{1,2}(D^f) &= \{\boldsymbol{\psi} \in W_{per}^{1,2}(D^f) : \mathrm{div}_c\, \boldsymbol{\psi} = 0,\ \psi_r = 0 \text{ on } \Gamma^0\},\\
H_{per}^U(D_\varepsilon^e) &= \{\boldsymbol{\varphi} \in W^{1,2}(0,T;U_{per}^{1,2}(D_\varepsilon^e)) : \frac{\partial^2 \boldsymbol{\varphi}}{\partial t^2} \in L^2(0,T;U_{per}^{-1,2}(D_\varepsilon^e))\},\\
H_{per}^V(D^f) &= \{\boldsymbol{\psi} \in L^2(0,T;V_{per}^{1,2}(D^f)) : \frac{\partial \boldsymbol{\psi}}{\partial t} \in L^2(0,T;V_{per}^{-1,2}(D^f))\}.
\end{aligned} \tag{4.14}$$

In order to define the space containing a function with the coupling condition, we put for any $\boldsymbol{\varphi}$ defined on D_ε^e and belonging to a certain functional space H,

$$V_{\boldsymbol{\varphi}} = \{\boldsymbol{\psi} \in V : \boldsymbol{\psi} = \boldsymbol{\varphi} \text{ on } \Gamma^{\varepsilon_1}\} \tag{4.15}$$

and then

$$S_H = \{(\boldsymbol{\varphi}, \boldsymbol{\psi}) : \boldsymbol{\varphi} \in H, \boldsymbol{\psi} \in V_{\boldsymbol{\varphi}}\}. \tag{4.16}$$

Note that the functions from H should have enough regularity for giving sense to the trace of $\boldsymbol{\varphi}$ on Γ^{ε_1}.

Remark 4.3.1. *In the axisymmetric case, we associate to any function $\boldsymbol{\psi} : L^f \mapsto \mathbb{R}^2$ or $\boldsymbol{\psi} :\ L_\varepsilon^e \mapsto \mathbb{R}^2$ the function $\boldsymbol{\Psi} : C^f \mapsto \mathbb{R}^3$ or $\boldsymbol{\Psi} : C_\varepsilon^e \mapsto \mathbb{R}^3$, respectively, such that*

$$\begin{aligned}
&\boldsymbol{\Psi}(x_1,x_2,x_3) \text{ is the 3D cartesian form of } \boldsymbol{\psi}(x_3,r)\\
&\text{for } (x_1,x_2,x_3) \in C^f (\text{or } C_\varepsilon^e), \quad \text{with } \sqrt{x_1^2+x_2^2} = r.
\end{aligned} \tag{4.17}$$

As in [66], we assume that

$$\begin{aligned}
&\rho_e,\ a_{ij}^{kl} \in L^\infty(0,1),\ i,j,k,l \in \{1,2,3\},\\
&\mathbf{g} \in W^{1,2}(0,T;L_{per}^2(D_\varepsilon^e)),\ \mathbf{f} \in W^{1,2}(0,T;L_{per}^2(D^f)).
\end{aligned} \tag{4.18}$$

In the framework presented above, the variational formulation of system

(4.8), proposed in [65] by G. Panasenko and R. Stavre, is given by

$$\begin{cases} \text{Find } (\mathbf{u},\mathbf{v}) \in H^U_{per} \times H^V_{per}, \text{ such that} \\ \omega_\rho \dfrac{\mathrm{d}}{\mathrm{dt}} \displaystyle\int_{D^e_\varepsilon} r\rho_e \frac{\partial \mathbf{u}(t)}{\partial t} \cdot \boldsymbol{\varphi} + \omega_E\, a_L(\mathbf{u}(t),\boldsymbol{\varphi}) + \rho_f \frac{\mathrm{d}}{\mathrm{dt}} \int_{D^f} r\mathbf{v}(t)\cdot\boldsymbol{\psi} \\ +2\nu \displaystyle\int_{D^f} r D_c(\mathbf{v}(t)) : D_c(\boldsymbol{\psi}) = \varepsilon^{-1} \int_{D^e_\varepsilon} r\mathbf{g}(t)\cdot\boldsymbol{\varphi} \\ + \displaystyle\int_{D^f} r\mathbf{f}(t)\cdot\boldsymbol{\psi} \quad \forall (\boldsymbol{\varphi},\boldsymbol{\psi}) \in S_U, \quad \text{a.e. in } (0,T), \\ \dfrac{\partial \mathbf{u}}{\partial t} = \mathbf{v} \qquad\qquad \text{in } L^2(0,T;W^{1/2,2}_{per}(\Gamma^{\varepsilon_1})), \\ \mathbf{u}(0) = \dfrac{\partial \mathbf{u}}{\partial t}(0) = \mathbf{0} \qquad \text{in } L^2_{per}(D^e_\varepsilon), \\ \mathbf{v}(0) = \mathbf{0} \qquad\qquad \text{in } L^2_{per}(D^f), \end{cases} \tag{4.19}$$

where

$$\begin{aligned} a_L(\mathbf{u},\boldsymbol{\varphi}) = \int_{D^e_\varepsilon} r \Big(\mu \Big(2 \Big(\frac{\partial u_3}{\partial x_3}\frac{\partial \varphi_3}{\partial x_3} + \frac{\partial u_r}{\partial r}\frac{\partial \varphi_r}{\partial r} \Big) \\ + \Big(\frac{\partial u_3}{\partial r} + \frac{\partial u_r}{\partial x_3} \Big) \Big(\frac{\partial \varphi_3}{\partial r} + \frac{\partial \varphi_r}{\partial x_3} \Big) + 2\frac{u_r}{r}\frac{\varphi_r}{r} \Big) + \lambda \mathrm{div}_c \mathbf{u}\, \mathrm{div}_c \boldsymbol{\varphi} \Big) \end{aligned} \tag{4.20}$$

is the bilinear form associated to the elasticity operator L. The results concerning the existence, the uniqueness and the regularity of the solution of (4.19) are obtained in [65].

4.4 Modified variational formulation for the numerical setup

Now we will modify the boundary conditions at the ends of the tube. Instead of the periodic solution with respect to the variable x_3, we introduce some given inflow and outflow supposing that the tube being clamped at its ends. Namely, the periodic boundary conditions $(4.8)_{10}$ are replaced by given Poiseuille type velocities $v_r = \frac{1}{4\nu}(\varepsilon_1^2 - r^2)g_{in}(t), v_3 = 0$ for $x_3 = 0$ and $v_r = \frac{1}{4\nu}(\varepsilon_1^2 - r^2)g_{out}(t), v_3 = 0$ for $x_3 = 1$ and by vanishing displacements $\mathbf{u} = 0$ for $x_3 = 0$ and $x_3 = 1$. Here g_{in} and g_{out} are given differentiable functions. The right-hand sides $\mathbf{g}$ and $\mathbf{f}$ are taken equal to zero. So, the problem takes the form

$$
\begin{cases}
\omega_\rho \rho_e \dfrac{\partial^2 \mathbf{u}}{\partial t^2} - \omega_E L\mathbf{u} = 0 & \text{in } L_\varepsilon^e \times (0,T), \\
\begin{cases} \rho_f \dfrac{\partial \mathbf{v}}{\partial t} - 2\nu \mathrm{div}_c D_c(\mathbf{v}) + \nabla p = 0 \\ \mathrm{div}_c \mathbf{v} = 0 \end{cases} & \text{in } L^f \times (0,T), \\
v_r = 0 & \text{on } F^0 \times (0,T), \\
\begin{cases} \dfrac{\partial u_3}{\partial r} + \dfrac{\partial u_r}{\partial x_3} = 0 \\ \lambda(1)\dfrac{\partial u_3}{\partial x_3} + (\lambda(1) + 2\mu(1))\dfrac{\partial u_r}{\partial r} \\ + \frac{\lambda(1)}{\varepsilon_1 + \varepsilon} u_r = 0 \end{cases} & \text{on } F^{\varepsilon_1 + \varepsilon} \times (0,T), \\
\begin{cases} \mathbf{v} = \dfrac{\partial \mathbf{u}}{\partial t} \\ \nu\left(\dfrac{\partial v_3}{\partial r} + \dfrac{\partial v_r}{\partial x_3}\right) = \omega_E \mu(0)\left(\dfrac{\partial u_3}{\partial r} + \dfrac{\partial u_r}{\partial x_3}\right) \\ -p + 2\nu \dfrac{\partial v_r}{\partial r} = \omega_E \Big(\lambda(0)\dfrac{\partial u_3}{\partial x_3} + (\lambda(0) \\ + 2\mu(0))\dfrac{\partial u_r}{\partial r} + \dfrac{\lambda(0)}{\varepsilon_1} u_r\Big) \end{cases} & \text{on } F^{\varepsilon_1} \times (0,T), \\
v_r = \frac{1}{4\nu}(\varepsilon_1^2 - r^2)g_{in}(t), v_3 = 0, \mathbf{u} = 0 & \text{for } x_3 = 0, \\
v_r = \frac{1}{4\nu}(\varepsilon_1^2 - r^2)g_{out}(t), v_3 = 0, \mathbf{u} = 0 & \text{for } x_3 = 1, \\
\mathbf{u}(0) = \dfrac{\partial \mathbf{u}}{\partial t}(0) = \mathbf{0} & \text{in } L_\varepsilon^e, \\
\mathbf{v}(0) = \mathbf{0} & \text{in } L^f.
\end{cases}
\tag{4.21}
$$

Respectively, the variational formulation is changed as follows:

$$
\begin{cases}
\text{Find } (\mathbf{u},\mathbf{v}) \in H^U \times H^V, \text{ such that} \\
v_r = \frac{1}{4\nu}(\varepsilon_1^2 - r^2) g_{in}(t), v_3 = 0, \mathbf{u} = 0 \text{ for } x_3 = 0, \\
v_r = \frac{1}{4\nu}(\varepsilon_1^2 - r^2) g_{out}(t), v_3 = 0, \mathbf{u} = 0 \text{ for } x_3 = 1, \text{ and} \\
\omega_\rho \dfrac{\mathrm{d}}{\mathrm{d}t} \displaystyle\int_{D_\varepsilon^e} r\rho_e \frac{\partial \mathbf{u}(t)}{\partial t} \cdot \boldsymbol{\varphi} + \omega_E \, a_L(\mathbf{u}(t), \boldsymbol{\varphi}) \\
+\rho_f \dfrac{\mathrm{d}}{\mathrm{d}t} \displaystyle\int_{D^f} r\mathbf{v}(t) \cdot \boldsymbol{\psi} + 2\nu \int_{D^f} r D_c(\mathbf{v}(t)) : D_c(\boldsymbol{\psi}) = 0 \\
\text{a.e. in } (0,T) \ \ \forall (\boldsymbol{\varphi}, \boldsymbol{\psi}) \in S_U, \\
\text{such that } \ \boldsymbol{\varphi}|_{x_3=0;1} = 0, \boldsymbol{\psi}|_{x_3=0;1} = 0, \\
\dfrac{\partial \mathbf{u}}{\partial t} = \mathbf{v} \qquad\qquad \text{in } L^2(0,T; W^{1/2,2}(\Gamma^{\varepsilon_1})), \\
\mathbf{u}(0) = \dfrac{\partial \mathbf{u}}{\partial t}(0) = \mathbf{0} \qquad \text{in } L^2(D_\varepsilon^e), \\
\mathbf{v}(0) = \mathbf{0} \qquad\qquad \text{in } L^2(D^f).
\end{cases}
\tag{4.22}
$$

Note, that the spaces H^U and H^V used in the (4.22) are defined analogously to (4.14) but without the periodicity condition and

$S_U = \left\{ (\boldsymbol{\varphi}, \boldsymbol{\psi}) : \boldsymbol{\varphi} \in H^U, \boldsymbol{\psi} \in V_{\boldsymbol{\varphi}} \right\}$ (see (4.15) and (4.16)).

Integrating $(4.22)_4$ with respect to t over the interval $[0;T]$ we get the equivalent integral expression

$$
\begin{cases}
\text{Find } (\mathbf{u},\mathbf{v}) \in H^U \times H^V, \text{ such that} \\
v_r = \frac{1}{4\nu}(\varepsilon_1^2 - r^2) g_{in}(t), v_3 = 0, \mathbf{u} = 0 \text{ for } x_3 = 0, \\
v_r = \frac{1}{4\nu}(\varepsilon_1^2 - r^2) g_{out}(t), v_3 = 0, \mathbf{u} = 0 \text{ for } x_3 = 1, \text{ and} \\
\omega_\rho \displaystyle\int_0^T \int_{D_\varepsilon^e} r\rho_e \frac{\partial^2 \mathbf{u}(t)}{\partial t^2} \cdot \boldsymbol{\varphi} \mathrm{d}t + \int_0^T \omega_E \, a_L(\mathbf{u}(t), \boldsymbol{\varphi}) \mathrm{d}t \\
+ \displaystyle\int_0^T \rho_f \int_{D^f} r \frac{\partial}{\partial t} \mathbf{v}(t) \cdot \boldsymbol{\psi} \mathrm{d}t + 2 \int_0^T \nu \int_{D^f} r D_c(\mathbf{v}(t)) : D_c(\boldsymbol{\psi}) \mathrm{d}t = 0 \\
\ \forall (\boldsymbol{\varphi}, \boldsymbol{\psi}) \in H^U \times H^V, \ \text{ such that } \ \boldsymbol{\varphi}|_{x_3=0;1} = 0, \\
\boldsymbol{\psi}|_{x_3=0;1} = 0, \ \text{ and} \dfrac{\partial \boldsymbol{\varphi}}{\partial t} = \boldsymbol{\psi} \qquad \text{in } L^2(0,T; W^{1/2,2}(\Gamma^{\varepsilon_1})), \\
\boldsymbol{\varphi}(0) = \boldsymbol{\varphi}(T) = \dfrac{\partial \boldsymbol{\varphi}}{\partial t}(0) = \dfrac{\partial \boldsymbol{\varphi}}{\partial t}(T) = \mathbf{0} \qquad \text{in } L^2(D_\varepsilon^e), \\
\boldsymbol{\psi}(0) = \boldsymbol{\psi}(T) = \mathbf{0} \qquad\qquad \text{in } L^2(D^f).
\end{cases}
\tag{4.23}
$$

Consider a set of test functions $S_U = \Big\{(\boldsymbol{\varphi}, \boldsymbol{\psi}) : \boldsymbol{\varphi} \in H^U, \boldsymbol{\psi} \in V_{\boldsymbol{\varphi}}\Big\}$. Since in axisymmetric case $\mathbf{u}$ contains two components u_3 and u_r, $\boldsymbol{\varphi}$ contains two components φ_3 and φ_r, $\mathbf{v}$ contains two components v_3 and v_r, $\boldsymbol{\psi}$ contains two components ψ_3 and ψ_r, by substituting (4.7) and (4.20) into $(4.23)_4$ we obtain the following equation:

$$\omega_\rho \int\limits_0^T \int\limits_{D_\varepsilon^e} r\rho_e \Big(\frac{\partial^2 u_3}{\partial t^2}\,\varphi_3 + \frac{\partial^2 u_r}{\partial t^2}\,\varphi_r\Big)$$

$$+\omega_E \int\limits_0^T \int\limits_{D_\varepsilon^e} \Bigg(2\mu r \Big(\frac{\partial u_3}{\partial x_3}\,\frac{\partial \varphi_3}{\partial x_3} + \frac{\partial u_r}{\partial r}\,\frac{\partial \varphi_r}{\partial r}\Big)$$

$$+\mu r \Big(\frac{\partial u_3}{\partial r} + \frac{\partial u_r}{\partial x_3}\Big)\Big(\frac{\partial \varphi_3}{\partial r} + \frac{\partial \varphi_r}{\partial x_3}\Big) + 2\mu r\,\frac{u_r}{r}\,\frac{\varphi_r}{r}$$

$$+\lambda r \Big(\frac{\partial u_3}{\partial x_3} + \frac{\partial u_r}{\partial r} + \frac{u_r}{r}\Big)\Big(\frac{\partial \varphi_3}{\partial x_3} + \frac{\partial \varphi_r}{\partial r} + \frac{\varphi_r}{r}\Big)\Bigg) \tag{4.24}$$

$$+\rho_f \int\limits_0^T \int\limits_{D^f} r\Big(\frac{\partial v_3}{\partial t}\psi_3 + \frac{\partial v_r}{\partial t}\psi_r\Big)$$

$$+2\nu \int\limits_0^T \int\limits_{D^f} r\Big(\frac{\partial v_3}{\partial x_3}\,\frac{\partial \psi_3}{\partial x_3} + \frac{1}{2}\Big(\frac{\partial v_3}{\partial r} + \frac{\partial v_r}{\partial x_3}\Big)\Big(\frac{\partial \psi_3}{\partial r} + \frac{\partial \psi_r}{\partial x_3}\Big)$$

$$+\frac{\partial v_r}{\partial r}\,\frac{\partial \psi_r}{\partial r}\Big) = 0.$$

Finally, we consider a projection of this variational formulation to the "ansatz space" of test functions showed in (4.10) with q given by (4.9) with arbitrary basic functions Q and w_3 from $C_0^\infty([0,T]\times[0,1])$. We look for a solution in the closure with respect to the norm $H^U \times H^V$ of the space of functions having the form (4.10) with smooth base functions. Here $2\varepsilon^2 Q$ is the average velocity, $2\pi\varepsilon^4 Q$ is the flux.

In what follows we consider a simplified ansatz, assuming that $w_3 = 0$ and taking only a part of terms in (4.10). Namely, we consider the following functions:

$$
\begin{aligned}
v_3(x_3,r,t) &= 4\varepsilon_1^2\left(1-\frac{r^2}{\varepsilon_1^2}\right)Q(x_3,t),\\
v_r(x_3,r,t) &= -\varepsilon_1^3\frac{r}{\varepsilon_1}\Big(2-\frac{r^2}{\varepsilon_1^2}\Big)\frac{\partial Q}{\partial x_3}(x_3,t),\\
u_3(x_3,r,t) &= \varepsilon\frac{r-\varepsilon_1}{\varepsilon}\left(\varepsilon_1^3\int\limits_0^t\frac{\partial^2 Q}{\partial x_3^2}(x_3,\theta)\mathrm{d}\theta\right)\\
&\quad -8\nu\omega_E^{-1}\varepsilon\varepsilon_1\left(\int\limits_0^{\frac{r-\varepsilon_1}{\varepsilon}}\frac{1-\tau}{\mu(\tau)}\mathrm{d}\tau\right)Q(x_3,t),\\
u_r(x_3,r,t) &= -\varepsilon_1^3\left(1-\varepsilon\int\limits_0^{\frac{r-\varepsilon_1}{\varepsilon}}\frac{1}{\varepsilon_1+\varepsilon\tau}\,\frac{\lambda(\tau)}{\lambda(\tau)+2\mu(\tau)}\mathrm{d}\tau\right)\\
&\quad \times\int\limits_0^t\frac{\partial Q}{\partial x_3}(x_3,\theta)\mathrm{d}\theta+\omega_E^{-1}\varepsilon\left(\int\limits_0^{\frac{r-\varepsilon_1}{\varepsilon}}\frac{1-\tau}{\lambda(\tau)+2\mu(\tau)}\mathrm{d}\tau\right)\\
&\quad \times\left(2\nu\varepsilon_1^2\frac{\partial Q}{\partial x_3}(x_3,t)+16\nu\int\limits_0^{x_3}Q(s,t)\mathrm{d}s\right),
\end{aligned}
\tag{4.25}
$$

where $Q\in L^2(0,T;W^{6,2}(0,1))$, $Q_t\in L^2(0,T;W^{2,2}(0,1))$ and $Q_{tt}\in L^2(0,T;W^{2,2}(0,1))$. Further, we will replace the notation of the basic function Q by the test function R.

Also, we assume that functions g_{in} and g_{out} satisfy the conditions $\langle g_{in}\rangle_T=\langle g_{out}\rangle_T=0$ and $\langle\int_0^t g_{in}(\tau)\mathrm{d}\tau\rangle_T=\langle\int_0^t g_{out}(\tau)\mathrm{d}\tau\rangle_T=0$, where $\langle\cdot\rangle_T=\int_0^T\cdot\mathrm{d}\tau$.

We look for a solution with Q satisfying the relations $\langle Q\rangle_T=\langle\int_0^t Q(\tau)\mathrm{d}\tau\rangle_T=0$. The test functions are considered as well with R satisfying the same relations: $\langle R\rangle_T=\langle\int_0^t R(\tau)\mathrm{d}\tau\rangle_T=0$.

After substituting (4.25) in (4.24) and integrating by parts, we obtain the following integro-differential equation:

$$
\begin{aligned}
&\tilde{C}_1\frac{\partial^4 Q(x_3,t)}{\partial x_3^4}+\tilde{C}_2\frac{\partial^2 Q(x_3,t)}{\partial t^2}+\tilde{C}_3\frac{\partial^2 Q(x_3,t)}{\partial x_3^2}+\tilde{C}_4\frac{\partial^4 Q(x_3,t)}{\partial x_3^2\partial t^2}\\
&\qquad+\tilde{C}_5\int_0^{x_3}\int_0^{\theta}\frac{\partial^2 Q(s,t)}{\partial t^2}\mathrm{d}s\mathrm{d}\theta+\tilde{C}_6\int_0^{t}\int_0^{\tau}\frac{\partial^6 Q(x_3,\theta)}{\partial x_3^6}\mathrm{d}\theta\mathrm{d}\tau\\
&+\tilde{C}_7\int_0^{t}\int_0^{\tau}\frac{\partial^2 Q(x_3,\theta)}{\partial x_3^2}\mathrm{d}\theta\mathrm{d}\tau+\tilde{C}_8Q(x_3,t)+\tilde{C}_9\int_0^{x_3}\int_0^{\theta}Q(s,t)\mathrm{d}s\mathrm{d}\theta\\
&+\tilde{C}_{10}\int_0^{t}\int_0^{\tau}\frac{\partial^4 Q(x_3,\theta)}{\partial x_3^4}\mathrm{d}\theta\mathrm{d}\tau+\tilde{C}_{11}\frac{\partial Q(x_3,t)}{\partial t}+\tilde{C}_{12}\frac{\partial^3 Q(x_3,t)}{\partial x_3^2\partial t}=0,
\end{aligned}
\tag{4.26}
$$

where

$$
\tilde{C}_1=-\omega_\rho\rho_e\varepsilon_1^6\frac{\varepsilon^3(3\varepsilon+4\varepsilon_1)}{12}+4\omega_E\mu\Big(\frac{\omega_E^{-1}\varepsilon}{\lambda+2\mu}\Big)^2\nu^2\varepsilon_1^4\frac{\varepsilon(11\varepsilon+16\varepsilon_1)}{120}+\frac{11}{24}\nu\varepsilon_1^8,
$$

$$
\tilde{C}_2=64\omega_\rho\rho_e\Big(\frac{\nu\omega_E^{-1}\varepsilon\varepsilon_1}{\mu}\Big)^2\frac{\varepsilon(11\varepsilon+16\varepsilon_1)}{120}-64\omega_\rho\rho_e\Big(\frac{\omega_E^{-1}\varepsilon}{\lambda+2\mu}\Big)^2\nu^2\varepsilon_1^2\frac{\varepsilon(11\varepsilon+16\varepsilon_1)}{120},
$$

$$
\begin{aligned}
\tilde{C}_3=&\frac{1}{4}\omega_\rho\rho_e\varepsilon_1^6\Big(((2\varepsilon^2+4\varepsilon_1\varepsilon+2\varepsilon_1^2)\ln^2(\frac{\varepsilon+\varepsilon_1}{\varepsilon_1})\\
&+(-2\varepsilon^2-4\varepsilon_1\varepsilon-2\varepsilon_1^2)\ln(\frac{\varepsilon+\varepsilon_1}{\varepsilon_1})+\varepsilon^2+2\varepsilon_1\varepsilon)\Big(\frac{\lambda}{\lambda+2\mu}\Big)^2\\
&+\big((-4\varepsilon^2-8\varepsilon_1\varepsilon-4\varepsilon_1^2)\ln(\frac{\varepsilon+\varepsilon_1}{\varepsilon_1})+2\varepsilon^2+4\varepsilon_1\varepsilon\big)\frac{\lambda}{\lambda+2\mu}+2\varepsilon^2+4\varepsilon_1\varepsilon\Big)\\
&-64\omega_E(2\mu+\lambda)\Big(\frac{\nu\omega_E^{-1}\varepsilon\varepsilon_1}{\mu}\Big)^2\frac{\varepsilon(11\varepsilon+16\varepsilon_1)}{120}-4\omega_E(2\mu+\lambda)\Big(\frac{\omega_E^{-1}\varepsilon}{\lambda+2\mu}\Big)^2\nu^2\varepsilon_1^4\frac{\varepsilon+4\varepsilon_1}{12\varepsilon}\\
&+64\omega_E\mu\Big(\frac{\omega_E^{-1}\varepsilon}{\lambda+2\mu}\Big)^2\nu^2\varepsilon_1^2\frac{\varepsilon(11\varepsilon+16\varepsilon_1)}{120}+\omega_E(2\mu+\lambda)\Big(\frac{\omega_E^{-1}}{\lambda+2\mu}\Big)^2\nu^2\varepsilon_1^4\big((4\varepsilon_1\varepsilon+2\varepsilon_1^2)\\
&\times\ln(\varepsilon_1+\varepsilon)-3\varepsilon^2+(-4\varepsilon_1\ln(\varepsilon_1)-2\varepsilon_1)\varepsilon-2\varepsilon_1^2\ln(\varepsilon_1)\big)\\
&+16\omega_E\lambda\frac{\nu\omega_E^{-1}\varepsilon\varepsilon_1}{\mu}\frac{\omega_E^{-1}\varepsilon}{\lambda+2\mu}\nu\varepsilon_1^2\Big(\frac{4\varepsilon}{15}+\frac{7\varepsilon+15\varepsilon_1}{60}\Big)-\omega_E\lambda\Big(\frac{\omega_E^{-1}\varepsilon}{\lambda+2\mu}\Big)^2\nu^2\varepsilon_1^4-\nu\varepsilon_1^6,
\end{aligned}
$$

$$
\tilde{C}_4=-4\omega_\rho\rho_e\Big(\frac{\omega_E^{-1}\varepsilon}{\lambda+2\mu}\Big)^2\nu^2\varepsilon_1^4\frac{\varepsilon(11\varepsilon+16\varepsilon_1)}{120},
$$

$$
\tilde{C}_5=-256\omega_\rho\rho_e\Big(\frac{\omega_E^{-1}\varepsilon}{\lambda+2\mu}\Big)^2\nu^2\frac{\varepsilon(11\varepsilon+16\varepsilon_1)}{120},
$$

$$\tilde{C}_6 = \omega_E(2\mu+\lambda)\varepsilon_1^6\frac{\varepsilon^3(3\varepsilon+4\varepsilon_1)}{12},$$

$$\tilde{C}_7 = \omega_E(2\mu+\lambda)\Big(\frac{\lambda\varepsilon_1}{\lambda+2\mu}\Big)^2\ln(\frac{\varepsilon+\varepsilon_1}{\varepsilon_1})+\omega_E(2\mu+\lambda)\varepsilon_1^6\Big(\frac{1}{3}\ln^3(\frac{\varepsilon+\varepsilon_1}{\varepsilon_1})\Big(\frac{\lambda}{\lambda+2\mu}\Big)^2$$
$$-\ln^2(\frac{\varepsilon+\varepsilon_1}{\varepsilon_1})\frac{\lambda}{\lambda+2\mu}+\ln(\frac{\varepsilon+\varepsilon_1}{\varepsilon_1})\Big)-\omega_E\frac{\lambda^2\varepsilon_1^6}{\lambda+2\mu}\Big(\ln(\frac{\varepsilon+\varepsilon_1}{\varepsilon_1})-\frac{1}{2}\ln^2(\frac{\varepsilon+\varepsilon_1}{\varepsilon_1})\frac{\lambda}{\lambda+2\mu}\Big)$$
$$-\omega_E\frac{\lambda^2\varepsilon_1^6}{\lambda+2\mu}\Big(\ln(\frac{\varepsilon+\varepsilon_1}{\varepsilon_1})-\frac{1}{2}\ln^2(\frac{\varepsilon+\varepsilon_1}{\varepsilon_1})\frac{\lambda}{\lambda+2\mu}\Big),$$

$$\tilde{C}_8 = -64\omega_E(2\mu+\lambda)\Big(\frac{\omega_E^{-1}\varepsilon}{\lambda+2\mu}\Big)^2\nu^2\varepsilon_1^2\frac{\varepsilon+4\varepsilon_1}{12\varepsilon}+64\omega_E\mu\Big(\frac{\nu\omega_E^{-1}\varepsilon\varepsilon_1}{\mu}\Big)^2\frac{\varepsilon+4\varepsilon_1}{12\varepsilon}$$
$$+256\omega_E\mu\Big(\frac{\omega_E^{-1}\varepsilon}{\lambda+2\mu}\Big)^2\nu^2\frac{\varepsilon(11\varepsilon+16\varepsilon_1)}{120}$$
$$+16\omega_E(2\mu+\lambda)\Big(\frac{\omega_E^{-1}\varepsilon}{\lambda+2\mu}\Big)^2\nu^2\varepsilon_1^2\varepsilon^{-2}\big((4\varepsilon_1\varepsilon+2\varepsilon_1^2)\ln(\varepsilon_1+\varepsilon)-3\varepsilon^2$$
$$+(-4\varepsilon_1\ln(\varepsilon_1)-2\varepsilon_1)\varepsilon-2\varepsilon_1^2\ln(\varepsilon_1))-16\omega_E\lambda\Big(\frac{\omega_E^{-1}\varepsilon}{\lambda+2\mu}\Big)^2\nu^2\varepsilon_1^2$$
$$+8\omega_E\lambda\frac{\nu\omega_E^{-1}\varepsilon\varepsilon_1}{\mu}\frac{\omega_E^{-1}\varepsilon}{\lambda+2\mu}\Big(\frac{4\varepsilon}{15}+\frac{7\varepsilon+15\varepsilon_1}{60}\Big)+16\nu\varepsilon_1^4,$$

$$\tilde{C}_9 = -64\omega_E(2\mu+\lambda)\Big(\frac{\omega_E^{-1}\varepsilon}{\lambda+2\mu}\Big)^2\nu^2\frac{\varepsilon+4\varepsilon_1}{3\varepsilon}$$
$$+64\omega_E(2\mu+\lambda)\Big(\frac{\omega_E^{-1}\varepsilon}{\lambda+2\mu}\Big)^2\nu^2\varepsilon^{-2}\big((4\varepsilon_1\varepsilon+2\varepsilon_1^2)\ln(\varepsilon_1+\varepsilon)-3\varepsilon^2$$
$$+(-4\varepsilon_1\ln(\varepsilon_1)-2\varepsilon_1)\varepsilon-2\varepsilon_1^2\ln(\varepsilon_1))-64\omega_E\lambda\Big(\frac{\omega_E^{-1}\varepsilon}{\lambda+2\mu}\Big)^2\nu^2,$$

$$\tilde{C}_{10} = -\omega_E\mu\varepsilon_1^6(\varepsilon\varepsilon_1+\frac{\varepsilon^2}{2})-\frac{1}{2}\omega_E\mu\varepsilon_1^6\Big(\big((2\varepsilon^2+4\varepsilon_1\varepsilon+2\varepsilon_1^2)\ln(\frac{\varepsilon_1+\varepsilon}{\varepsilon_1})$$
$$-\varepsilon^2-2\varepsilon\varepsilon_1\big)\frac{\lambda}{\lambda+2\mu}-2\varepsilon^2-4\varepsilon\varepsilon_1\Big)-\frac{1}{4}\omega_E\mu\varepsilon_1^6\Big(\big((2\varepsilon^2+4\varepsilon_1\varepsilon+2\varepsilon_1^2)\ln^2(\frac{\varepsilon+\varepsilon_1}{\varepsilon_1})$$
$$+(-2\varepsilon^2-4\varepsilon_1\varepsilon-2\varepsilon_1^2)\ln(\frac{\varepsilon+\varepsilon_1}{\varepsilon_1})+\varepsilon^2+2\varepsilon_1\varepsilon\big)\Big(\frac{\lambda}{\lambda+2\mu}\Big)^2+\big((-4\varepsilon^2-8\varepsilon_1\varepsilon$$
$$-4\varepsilon_1^2)\ln(\frac{\varepsilon+\varepsilon_1}{\varepsilon_1})+2\varepsilon^2+4\varepsilon_1\varepsilon\big)\frac{\lambda}{\lambda+2\mu}+2\varepsilon^2+4\varepsilon_1\varepsilon\Big)+\omega_E\lambda\frac{\varepsilon_1^6\varepsilon^2}{2(\lambda+2\mu)}$$
$$+\omega_E\frac{\varepsilon_1^6\lambda^2}{\lambda+2\mu}\frac{\varepsilon^2}{2}+\frac{1}{2}\omega_E\lambda\varepsilon_1^6\Big(\big((2\varepsilon^2-2\varepsilon_1^2)\ln(\frac{\varepsilon_1+\varepsilon}{\varepsilon_1})-\varepsilon^2-2\varepsilon_1\varepsilon\big)\frac{\lambda}{\lambda+2\mu}-2\varepsilon^2\Big),$$

$$\tilde{C}_{11} = \frac{8}{3}\rho_f \varepsilon_1^6,\ \tilde{C}_{12} = \frac{11}{24}\rho_f \varepsilon_1^8.$$

Further we consider a shorter approximation of the solution:

$$\begin{aligned}
v_3(x_3,r,t) &= 4\varepsilon_1^2\left(1-\frac{r^2}{\varepsilon_1^2}\right)Q(x_3,t),\\
v_r(x_3,r,t) &= -\varepsilon_1^3\frac{r}{\varepsilon_1}\Big(2-\frac{r^2}{\varepsilon_1^2}\Big)\frac{\partial Q}{\partial x_3}(x_3,t),\\
u_3(x_3,r,t) &= -8\nu\omega_E^{-1}\varepsilon\varepsilon_1\left(\int\limits_0^{\frac{r-\varepsilon_1}{\varepsilon}}\frac{1-\tau}{\mu(\tau)}\mathrm{d}\tau\right)Q(x_3,t),\\
u_r(x_3,r,t) &= 2\omega_E^{-1}\varepsilon\nu\left(\int\limits_0^{\frac{r-\varepsilon_1}{\varepsilon}}\frac{1-\tau}{\lambda(\tau)+2\mu(\tau)}\mathrm{d}\tau\right)\varepsilon_1^2\frac{\partial Q}{\partial x_3}(x_3,t).
\end{aligned} \tag{4.27}$$

We assume that Lamé parameters μ and λ are constant, so from (4.27) we obtain the following expressions:

$$\begin{aligned}
v_3(x_3,r,t) &= 4\varepsilon_1^2\left(1-\frac{r^2}{\varepsilon_1^2}\right)Q(x_3,t),\\
v_r(x_3,r,t) &= -\varepsilon_1^3\frac{r}{\varepsilon_1}\Big(2-\frac{r^2}{\varepsilon_1^2}\Big)\frac{\partial Q}{\partial x_3}(x_3,t),\\
u_3(x_3,r,t) &= -\frac{8\nu\,\omega_E^{-1}\varepsilon\varepsilon_1}{\mu}\Big(\frac{r-\varepsilon_1}{\varepsilon}-\frac{(r-\varepsilon_1)^2}{2\varepsilon^2}\Big)Q(x_3,t),\\
u_r(x_3,r,t) &= -\frac{2\omega_E^{-1}\varepsilon\nu}{\lambda+2\mu}\Big(\frac{r-\varepsilon_1}{\varepsilon}-\frac{(r-\varepsilon_1)^2}{2\varepsilon^2}\Big)\varepsilon_1^2 Q(x_3,t).
\end{aligned} \tag{4.28}$$

By substituting (4.28) into the following integral identity obtained differentiating (4.24) with respect to t:

$$\begin{aligned}
&\omega_\rho\frac{d}{dt}\int\limits_{D_\varepsilon^e} r\rho_e\Big(\frac{\partial u_3}{\partial t}\,\varphi_3+\frac{\partial u_r}{\partial t}\,\varphi_r\Big)+\omega_E\int\limits_{D_\varepsilon^e}\Big(2\mu\,r\,\Big(\frac{\partial u_3}{\partial x_3}\,\frac{\partial\varphi_3}{\partial x_3}+\frac{\partial u_r}{\partial r}\,\frac{\partial\varphi_r}{\partial r}\Big)\\
&\qquad+\mu\,r\,\Big(\frac{\partial u_3}{\partial r}+\frac{\partial u_r}{\partial x_3}\Big)\Big(\frac{\partial\varphi_3}{\partial r}+\frac{\partial\varphi_r}{\partial x_3}\Big)\\
&\quad+2\mu\,r\,\frac{u_r}{r}\,\frac{\varphi_r}{r}+\lambda\,r\Big(\frac{\partial u_3}{\partial x_3}+\frac{\partial u_r}{\partial r}+\frac{u_r}{r}\Big)\Big(\frac{\partial\varphi_3}{\partial x_3}+\frac{\partial\varphi_r}{\partial r}+\frac{\varphi_r}{r}\Big)\Big)\\
&\qquad+\rho_f\frac{d}{dt}\int\limits_{D^f} r\left(v_3\psi_3+v_r\psi_r\right)\\
&+2\nu\int\limits_{D^f} r\Big(\frac{\partial v_3}{\partial x_3}\,\frac{\partial\psi_3}{\partial x_3}+\frac{1}{2}\Big(\frac{\partial v_3}{\partial r}+\frac{\partial v_r}{\partial x_3}\Big)\Big(\frac{\partial\psi_3}{\partial r}+\frac{\partial\psi_r}{\partial x_3}\Big)+\frac{\partial v_r}{\partial r}\,\frac{\partial\psi_r}{\partial r}\Big)=0,
\end{aligned} \tag{4.29}$$

we obtain the 4^{th} order differential equation describing the elastic wall Poiseuille equation (EWPE):

$$\begin{aligned} C_1\frac{\partial^2 Q(x_3,t)}{\partial t^2}+C_2\frac{\partial^4 Q(x_3,t)}{\partial x_3^2\partial t^2}+C_3\frac{\partial Q(x_3,t)}{\partial t}+C_4\frac{\partial^3 Q(x_3,t)}{\partial x_3^2\partial t} \\ +C_5\frac{\partial^4 Q(x_3,t)}{\partial x_3^4}+C_6\frac{\partial^2 Q(x_3,t)}{\partial x_3^2}+C_7 Q(x_3,t)=0, \end{aligned} \tag{4.30}$$

where

$$C_1=\frac{8\omega_\rho\rho_e\nu^2\omega_E^{-2}\varepsilon_1^2\varepsilon^3(16\varepsilon_1+11\varepsilon)}{15\mu},\ C_2=-\frac{\omega_\rho\rho_e\nu^2\omega_E^{-2}\varepsilon_1^4\varepsilon^3(16\varepsilon_1+11\varepsilon)}{30(\lambda+2\mu)^2},$$

$$C_3=\frac{8\rho_f\varepsilon_1^6}{3},\ C_4=-\frac{11\rho_f\varepsilon_1^8}{24},\ C_5=\omega_E\frac{\mu\nu^2\omega_E^{-2}\varepsilon_1^4\varepsilon^3(16\varepsilon_1+11\varepsilon)}{30(\lambda+2\mu)^2}+2\nu\frac{11\varepsilon_1^8}{48},$$

$$\begin{aligned} C_6=-\omega_E\Bigg(&\frac{8(\lambda+2\mu)\nu^2\omega_E^{-2}\varepsilon_1^2\varepsilon^3(16\varepsilon_1+11\varepsilon)}{15\mu^2}+\frac{2\lambda\nu^2\omega_E^{-2}\varepsilon_1^4\varepsilon(4\varepsilon_1+\varepsilon)}{3(\lambda+2\mu)^2} \\ &+\frac{(\lambda-2\mu)\nu^2\varepsilon_1^4\big((4\varepsilon_1\varepsilon+2\varepsilon_1^2)\ln(\varepsilon_1+\varepsilon)-3\varepsilon^2-(\ln(\varepsilon_1^{4\varepsilon_1})+2\varepsilon_1)\varepsilon-\ln(\varepsilon_1^{2\varepsilon_1^2})\big)}{\omega_E^2\varepsilon(\lambda+2\mu)^2} \\ &+\frac{-4\lambda\nu^2\omega_E^{-2}\varepsilon_1^3\varepsilon^2(15\varepsilon_1+7\varepsilon)}{15\mu(\lambda+2\mu)}+\frac{-32\lambda\nu^2\omega_E^{-2}\varepsilon_1^3\varepsilon^3}{15\mu(\lambda+2\mu)} \\ &+\frac{\lambda\nu^2\omega_E^{-2}\varepsilon_1^4\varepsilon^2}{(\lambda+2\mu)^2}+\frac{2\lambda\nu^2\omega_E^{-2}\varepsilon_1^3\varepsilon^3(16\varepsilon_1+11\varepsilon)}{15\mu(\lambda+2\mu)}\Bigg)+\omega_E\frac{-2\mu\nu^2\omega_E^{-2}\varepsilon_1^3\varepsilon^2(15\varepsilon_1+7\varepsilon)}{15\mu(\lambda+2\mu)} \\ &+\omega_E\frac{-2\mu\nu^2\omega_E^{-2}\varepsilon_1^3\varepsilon^2(15\varepsilon_1+7\varepsilon)}{15\mu}-2\nu\frac{19\varepsilon_1^6}{6}+4\nu\frac{4\varepsilon_1^6}{3}, \end{aligned}$$

$$C_7=\omega_E\frac{16\mu\nu^2\omega_E^{-2}\varepsilon_1^2\varepsilon(4\varepsilon_1+\varepsilon)}{3\mu^2}+2\nu 8\varepsilon_1^4.$$

4.5 Numerical scheme for the EWPE

In this section, we describe the scheme from doctoral dissertation [87] by V. Šumskas for numerical solution to the following boundary value problem for the elastic wall Poiseuille equation (EWPE) (4.30):

$$\begin{cases} C_1\dfrac{\partial^2 Q(x_3,t)}{\partial t^2}+C_2\dfrac{\partial^4 Q(x_3,t)}{\partial x_3^2\partial t^2}+C_3\dfrac{\partial Q(x_3,t)}{\partial t}+C_4\dfrac{\partial^3 Q(x_3,t)}{\partial x_3^2\partial t} \\ +C_5\dfrac{\partial^4 Q(x_3,t)}{\partial x_3^4}+C_6\dfrac{\partial^2 Q(x_3,t)}{\partial x_3^2}+C_7 Q(x_3,t)=0, \\ Q(0,t)=g_{in}(t),\ Q(1,t)=g_{out}(t), \\ \dfrac{\partial Q(0,t)}{\partial x_3}=\dfrac{\partial Q(1,t)}{\partial x_3}=0, \\ Q(x_3,0)=\dfrac{\partial Q(x_3,0)}{\partial t}=0. \end{cases} \tag{4.31}$$

Let us approximate the derivatives in (4.31) numerically using the finite difference method. See Figure 4.2 below for a simplified visualisation of the proposed numerical approximation of these terms (x_3 is denoted by x).

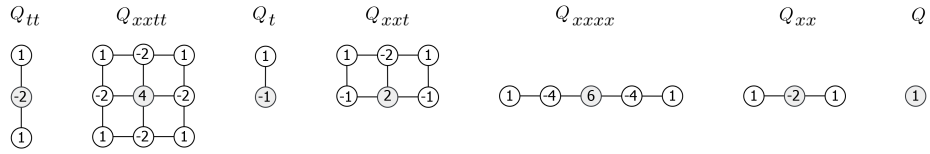

Figure 4.2 – A schematic visualisation of numerical approximation of terms involved in (4.31), here the numbers inside circles correspond to the weights of coefficients of numerical points for approximations of differential terms. Vertical direction corresponds stepping in time, while horizontal direction corresponds stepping in space

A uniform numerical grid is used, as no localized effects are of interest here and thus there is no need to thicken the mesh at some places. Let us denote by Q_i^n the numerical solution to (4.31) at $(x_i,t_n)=(ih,n\tau)$, here h and τ are step sizes in space and time, respectively, with

$$i=0,\dots,N_h,\ h=L/N_h,$$
$$n=0,\dots,N_\tau,\ \tau=T/N_\tau,$$

where L is the length of spatial domain and T is the length of time interval. The computational molecule applied at numerical mesh interior point Q_i^n is depicted in Figure 4.3

For simplicity, the following notations will be used in this section:

$$m_1=\frac{C_1}{\tau^2},\ m_2=\frac{C_2}{h^2\tau^2},\ m_3=\frac{C_3}{\tau},\ m_4=\frac{C_4}{h^2\tau},$$
$$m_5=\frac{C_5}{h^4},\ m_6=\frac{C_6}{h^2},\ m_7=C_7.$$

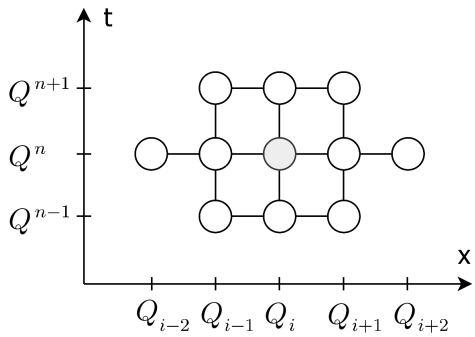

Figure 4.3 – A computational molecule (stencil).

Now, let us find the coefficients of each point of the computational molecule:

$$
\begin{aligned}
Q_{i-i}^{n+1} &: \; m_2 + m_4; \\
Q_i^{n+1} &: \; m_1 - 2m_2 + m_3 - 2m_4; \\
Q_{i-1}^{n+1} &: \; m_2 + m_4; \\
Q_{i-2}^{n} &: \; m_5; \\
Q_{i-1}^{n} &: \; -2m_2 - m_4 - 4m_5 + m_6; \\
Q_i^{n} &: \; -2m_1 + 4m_2 - m_3 + 2m_4 + 6m_5 - 2m_6 + m_7; \\
Q_{i+1}^{n} &: \; -2m_2 - m_4 - 4m_5 + m_6; \\
Q_{i+2}^{n} &: \; m_5; \\
Q_{i-1}^{n-1} &: \; m_2; \\
Q_i^{n-1} &: \; m_1 - 2m_2; \\
Q_{i+1}^{n-1} &: \; m_2.
\end{aligned}
$$

As there are three points in the unknown time layer Q^{n+1}, at each time step the solution is implemented implicitly using the classical Thomas algorithm for tridiagonal matrices.

Note that in general, the expected accuracy of this scheme is $O(h^2 + \tau)$, as forward differences are used to approximate derivatives of first order in time, while the second and fourth order derivatives are approximated using central differences.

Using the classical stability analysis, it is easy to show that for the practical problems of our interest, the numerical stability Courant-Friedrichs-Lewy (CFL) condition $\tau \leqslant ch^2$ holds with some constant c that depends on the parameters of the model.

We seek the scaled average velocity Q in m/s inside a small elastic tube or capillary with the Young modulus $E = 10^6$ Pa, the Poisson ratio $\hat{\nu} = 0.35$, the length of the tube 10^{-3} m, the radius $5 \cdot 10^{-5}$ m, the thickness $\varepsilon = 2 \cdot 10^{-5}$ m and the dynamic viscosity of blood $\nu = 4 \cdot 10^{-3}$ Pa·s, the following set of constants C_i was obtained:

$C_1 = 9.2287 \cdot 10^{-38},\ C_2 = -2.0734 \cdot 10^{-42},\ C_3 = 4.1667 \cdot 10^{-2},$
$C_4 = -1.7904 \cdot 10^{1},\ C_5 = 7.1615 \cdot 10^{1},\ C_6 = -6.2500 \cdot 10^{-2},\ C_7 = 4.000 \cdot 10^{-4}.$

To test the accuracy of the constructed solver, let us define the error in the maximum norm by e, also the experimental convergence rates in space and time by e_h and e_τ:

$$e(h,\tau) = \max_m \left| U_m^N - U(x^m,T) \right|,\ e_h(h) = \log_2 \left(\frac{e(2h,\tau)}{e(h,\tau)} \right),$$
$$e_\tau(\tau) = \log_2 \left(\frac{e(h,2\tau)}{e(h,\tau)} \right).$$

Here $U(x^m,T)$ is a benchmark solution, which is computed using very small step sizes. The results of experimental convergence tests are presented in Table 4.1. Here the functions $g_{in}(t) = 0.005 \sin(2t)$, $g_{out} = 0.001 e^t$ were used and the problem was solved for $T = 1$. Table 4.1 shows that the experimental convergence rate agrees well with the theoretical estimate.

h	$e(h,\tau)$	$e_h(h)$	τ	$e(h,\tau)$	$e_\tau(\tau)$
$1 \cdot 10^{-4}$	$3.1982 \cdot 10^{-6}$	2.0019	$5 \cdot 10^{-5}$	$1.1683 \cdot 10^{-10}$	1.0203
$5 \cdot 10^{-5}$	$7.9850 \cdot 10^{-7}$	1.9957	$2.5 \cdot 10^{-5}$	$5.7601 \cdot 10^{-11}$	1.0409
$2.5 \cdot 10^{-5}$	$2.0022 \cdot 10^{-7}$	1.9984	$1.25 \cdot 10^{-5}$	$2.7996 \cdot 10^{-11}$	1.0900
$1.25 \cdot 10^{-5}$	$5.0111 \cdot 10^{-8}$	2.0105	$6.25 \cdot 10^{-6}$	$1.3152 \cdot 10^{-11}$	0.9782

Table 4.1 – Errors and experimental convergence rates for sequences of step sizes in space (left) and time (right). The results confirm experimentally that the order of accuracy of the numerical scheme is $O(h^2 + \tau)$.

The first order derivatives in the numerical implementation of boundary and initial conditions respectively are approximated in the following form:

$$Q_t(x_i,t_0) = \frac{Q_i^1 - Q_i^{-1}}{2\tau} + O(\tau^2) \quad \text{and} \quad Q_x(x_i,t_n) = \frac{Q_{i+1}^n - Q_{i-1}^n}{2h} + O(h^2).$$

For additional details on stability, accuracy and numerical tests, please refer to [87].

4.6 Numerical comparison of the approximate 1D model and the full-dimension problem

In the present section, we compare the numerical solutions of two problems: the full dimension Navier–Stokes equations with the fluid-structure interaction (FSI) conditions for the tubes with an elastic wall and the EWPE approximation.

Solution in a single vessel

We consider two types of inflow/outflow boundary conditions: first, $g_{in}(t) = g_{out}(t)$; second, with $g_{out}(t) = g_{in}(t+\delta)$ and compare the solutions in the middle point of the tube.

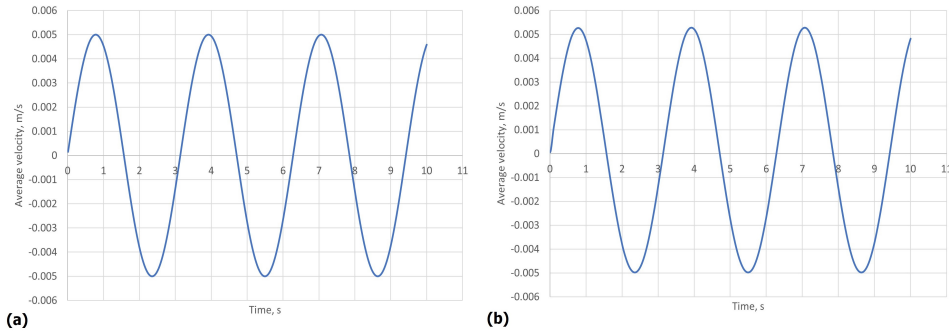

Figure 4.4 – (a) the average velocity computed by EWPE (the 4^{th} order PDE (4.31))in time, (b) the average solution (velocity) of the full Navier–Stokes model. In both cases, $g_{in} = 0.005\sin(2t)$, $g_{out} = 0.005\sin(2t+0.02)$ and the solution was taken in the middle cross section of the tube.

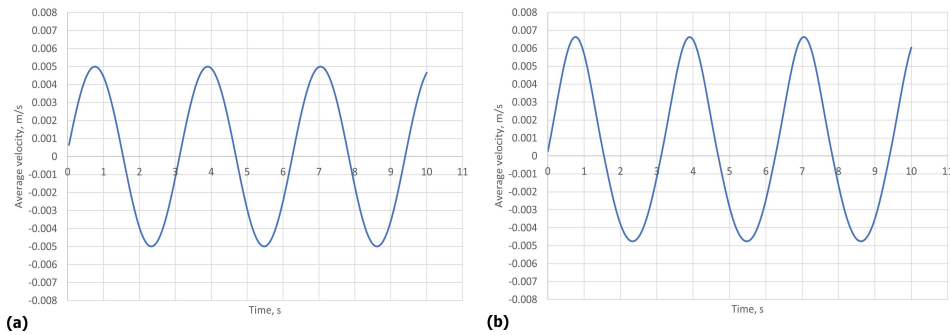

Figure 4.5 – (a) the average velocity according to the EWPE approximation in time, (b) the average velocity of the full Navier–Stokes model. In both cases, $g_{in} = 0.005\sin(2t)$, $g_{out} = 0.005\sin(2t+0.1)$ and the solution was taken in the middle cross section of the tube. Note that here we purposely simulate a case of large displacement of the wall, to explore the limitations of the ansatz.

For $\delta = 0$ and $\delta = 0.1$ the difference between the solutions is less than 10 percent. When δ increases ($\delta = 0.2$, $\delta = 0.25$), the difference is more significant. It can be explained by important variations of the cross section (more than two times).

Solution in a Y-shaped network of vessels

Next, we compare solutions acquired by (4.31) and the full Navier–Stokes in a Y-shaped network (see Figure 4.7), where the inflow is on the left and two outflows are on the right. The corresponding boundary conditions are $g_{in} = 0.005\sin(2t)$ and $g_{out} = 0.0025\sin(2t + 0.02)$ for each of the two outlets to the right, while the Young modulus is $E = 10^6$ Pa for the tube-shaped blood vessel wall and $E = 10^{10}$ Pa for the sphere-shaped connection of three tubes, the Poisson ratio $\hat{\nu} = 0.35$, the length of each of the three tubes 10^{-2} m, the radius 10^{-3} m, the wall thickness $\varepsilon = 10^{-4}$ m and the dynamic viscosity of blood $\nu = 4 \cdot 10^{-3}$ Pa·s. The large Young's modulus of the wall in the bifurcation zone simulates the no-slip boundary condition there. It corresponds to the experimental observations that near the bifurcations the vessels become much stiffer than the "tube" walls.

The EWPE approximation used the following junction conditions at the bifurcation node (see Figure 4.6):

1) the flux $4\pi\varepsilon_1^4 Q$ coming from the left tube is equal to the sum of the fluxes going out into the right tubes (this condition corresponds to a stiffer bifurcation zone of vessels),
2) the first derivatives $\frac{\partial Q}{\partial x_3} = 0$ for all tubes at the bifurcation node.
3) the second derivatives $\frac{\partial^2 Q}{\partial x_3^2} = 0$ at the bifurcation node for the tubes on the right.

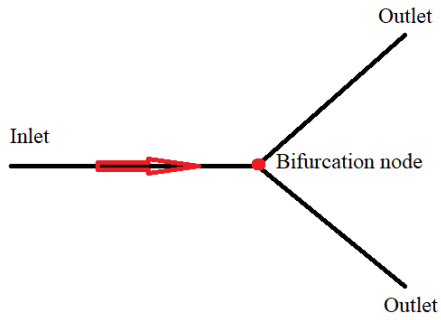

Figure 4.6 – The scheme of Y-shaped bifurcation model.

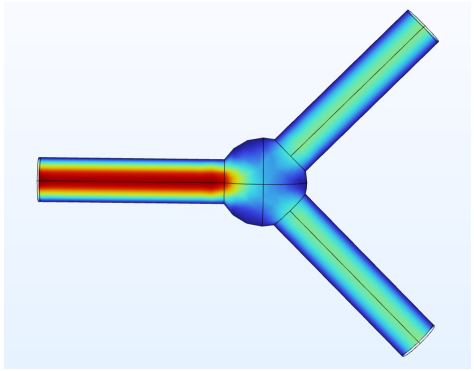

Figure 4.7 – The geometry of Y-shaped bifurcation model.

Figures 4.8 and 4.9 display the graphs of averaged velocity in midpoints of left and right vessels, respectively, up to T=10.

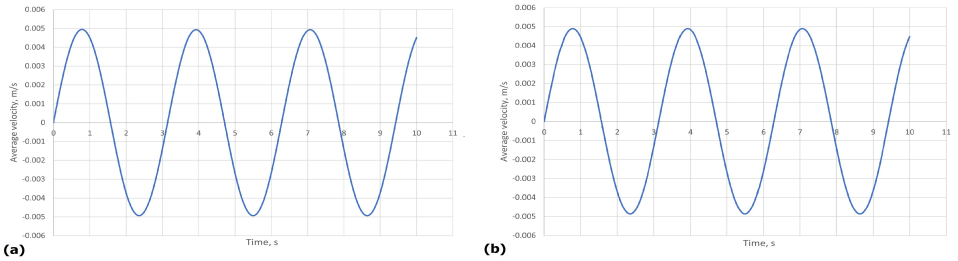

Figure 4.8 – (a) the average velocity by the EWPE approximation (4.31) in time, (b) the average velocity of the full Navier–Stokes model. In both cases, $g_{in} = 0.005\sin(2t)$, $g_{out} = 0.0025\sin(2t+0.02)$ and the solution was taken in the middle cross section of the left tube.

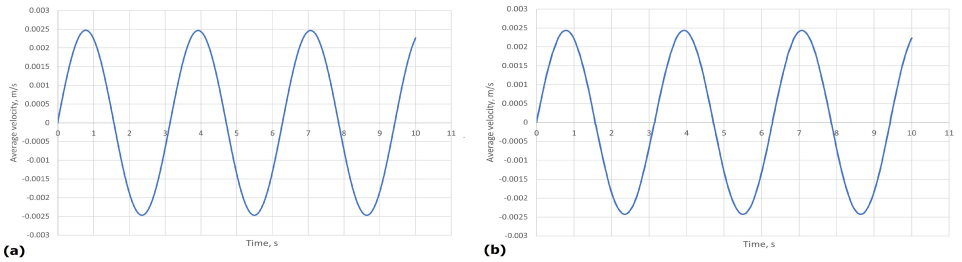

Figure 4.9 – (a) the average velocity by the EWPE approximation(4.31) in time, (b) the average velocity of the full Navier–Stokes model. In both cases, $g_{in} = 0.005\sin(2t)$, $g_{out} = 0.0025\sin(2t+0.02)$, and the solution was taken in the middle cross section of either of the right tubes.

The inflows and outflows conserving the flux as well as without flux conservation are tested. The obtained results show a good approximation for the fluid-structure interaction model in the case of small displacements of the wall and modest Reynold's numbers.

Chapter 5

Efficient Computation of Blood Velocity in the Left Atrial Appendage: A Practical Perspective

5.1 Introduction

Circulatory diseases are the leading causes of death in the world (see [98]). These diseases are mostly related to the thrombus formation in various parts of the circulatory system (see [98]). One of the most dangerous scenarios is thrombogenesis at the left atrial appendage (LAA) of the heart during the atrial fibrillation (AF). The choice of the treatment strategy needs the detailed patient-specific information on the blood circulation in LAA. The information obtained by the clinical investigations of a patient by Magnetic Resonance Imaging (MRI), Computed Tomography (CT) or Electrocardiogram (ECG) technique is not complete, that is why the modern clinical practice uses some scores (see for example Table 5.1).

Such scores are not too reliable. That is why actually mathematical modeling becomes an important tool to get much more precise information on the blood flow in patient-specific LAA and to evaluate the thrombogenesis risk. Two main directions are developed in this context: the first one is the direct computer simulations of the blood flow in patient-specific LAA with detection of stagnation zones as the probable places of thrombogenesis; while the second one is related to the detailed mathematical modeling of the coagulation process (coagulation cascade of reactions) combined with the hemodynamics (see [5], [13], [25], [26], [41], [48], [81], [89], [90], [91],

CHA_2DS_2–VASc Score		
C	Congestive Heart Failure	1 point
H	Hypertension	1 point
A_2	Age $\geqslant 75$ years	2 points
D	Diabetes	1 point
S_2	Stroke	2 points
V	Vascular disease	1 point
A	Age $\geqslant 65$ years	1 point
Sc	Sex category, female	1 point

Table 5.1 – CHA_2DS_2–VASc (or $CHADS_2$) score system. Maximum total score = 10 points. Anticoagulation Recommendations: Score = 0 no therapy. Score $\geqslant 1$ oral anticoagulation (see [52]).

[92], [93], [100], [102]). The second direction allows to understand the physiological mechanism of thrombogenesis but it needs the characterization of multiple parameters regarding the reaction kinetics which is difficult to obtain in clinical practice; also the models are sensitive to uncertainties in these parameters. The main challenges in the first direction (see [12], [34], [42], [51], [95], [97]) are: fluid dynamics simulations in patient-specific (not idealized) complex geometry, which is in reality time dependent due to the heart-wall motion. Thus, in recent paper [97] by D. Vella *et al.* LA is modelled by a very simplified geometry, in [12] by G.M. Bosi *et al.* the flow in LA with rigid (not moving) wall is simulated.

In this Chapter we introduce a fluid-structure interaction (FSI) model of the blood flow in the LA and provide two patient-specific studies of the stagnation zones. One of the patients had a stroke and the second had not. We will also discuss the challenges of the FSI simulations, such as convergence of the numerical process. The research starts from CT imaging, segmentation, cleaning (noise reduction), and subsequent domain generation. The obtained domain is then employed to solve the Navier–Stokes equations within the LA, accounting for the elastic behavior of the LA wall. By applying the FSI model we compute the velocity and the pressure in the LA, and in particular, in the LAA. The contraction of the LA is simulated by the application of the outer pressure. The model was validated for the

contraction force by controlling the 20 % decreasing of the volume of the LA, for the inflow-outflow boundary conditions by comparing the computed velocity with the measured by Doppler technique velocity at some points in LA (note that measurement of the velocity inside the LAA is very difficult).

5.2 LAA classification and Thrombogenesis

The human heart comprises four chambers: the LA, Left Ventricle, Right Atrium, and Right Ventricle (see Figure 5.1). LA is equipped with an appendage known as the LAA. In case of AF the probability of thrombi formation in LAA increases, leading to a heightened risk of cardioembolic events.

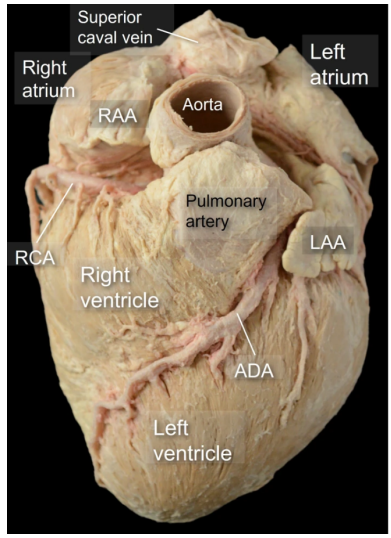

Figure 5.1 – In this specimen, the epicardium has been removed to show the spatial relationship of the cardiac structures in relation to the LAA. The left atrium is located superiorly and posteriorly to the right atrium. Note the close relationship of the anterior wall of the left atrium to the ascending Aorta, and the LAA with the right ventricle outflow tract (see [35]).

The length of the LAA is on average 45 mm long, with a range from 27 to 60 mm. The types of LAA in [23] by L. Di Biase *et al.* are classified into the following geometries: "chicken wing" (48% of population), "windsock"(19% of population), "cauliflower"(3% of population), and "cactus" (30% of population).

During normal sinus rhythm (when a person is healthy), the risk of a thrombus formation is very low (see [43]), but during AF the blood flow

velocity, which results from a combination of LAA contraction and filling, is much lower when compared to the sinus rhythm.

Blood flow velocities below 37 cm/s are linked to an elevated risk of a thrombus formation (see [47]). Moreover, in [11] by J. L. Blackshear *et al.* a comprehensive analysis was done by reviewing twenty-three distinct studies where we can see that among the 3,504 patients with AF due to rheumatic causes, 13% (446 patients) confirmed a thrombus in LAA. Similarly, among the 1,288 patients with non-rheumatic AF, 17% (222 patients) had documented a thrombus in LAA.

The likelihood of experiencing a stroke or transient ischemic attack during AF depends on the geometry of the LAA. In [85] by J. M. Smit *et al.*, the following data is shown: the incidence of stroke ar transient ischemic attack varies according to different LAA geometries, with the highest rates observed in patients with a cactus-shaped LAA (19%), followed by cauliflower-shaped (8%), windsock-shaped (7%), and chicken wing-shaped (6%) LAAs.

5.3 The Development of the Model

5.3.1 Imaging. Cleaning. Making Geometry

The imaging process involved a chest Computed Tomography (CT) scans which come in Digital Imaging and Communications in Medicine (DICOM) format files. One such file consists of a set of images with headers. In the case of a CT scan of the heart, the file includes images of about 500 slices of the human chest. Figure 5.2 shows one of the slices of a CT scan opened in 3D-Slicer software, used for visualizing and processing 3D images. The images, viewed in three planes (the axial, sagittal and coronal) were manually segmented to separate the left side of the heart from surrounding tissues. 3D-Slicer produced a primary geometry of the left side of the heart with a rough surface and parts of veins that were unnecessary for the calculations, and therefore removed. The resulting .stl file was edited using Meshlab, a software for processing 3D triangular meshes. The rough surface of the primary geometry would have up to 300 000 triangular elements. To simplify the process of editing the geometry, the number of mesh elements was reduced to 30 000 elements.

Figure 5.2 – CT of a human chest area

SolidWorks2022 was then used to edit the .ply file. This software is used to design, analyse and visualize models of solid objects. The left ventricle and parts of the pulmonary veins that extended the most were removed, and mesh errors (such as inverted mesh elements and very fine elements pointing outwards) were avoided. The surface was smoothened so that the model would upload to COMSOL and the calculations would converge, but the geometry remained as close to the original left atrium as possible (see Figure 5.3).

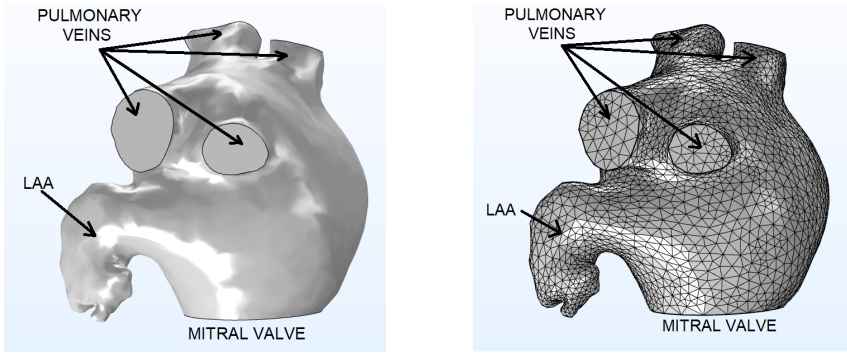

Figure 5.3 – Left Atrium (LA) containing Left Atrial Appendage (LAA): Computation geometry on the left hand side and computation mesh on the right hand side.

5.3.2 Formulation of the problem

The model considers the four pulmonary veins as inlets and the mitral valve as the outlet. The whole interior part of the LA is considered as a fluid domain G (see Figure 5.3). We use the FSI model. The boundary of domain G is presented as a union of three parts: the lateral wall of the LA

(fluid-structure interface), denoted as Γ_1, four cross sections $\gamma_2^{(1)},...,\gamma_2^{(4)}$ of the pulmonary veins (we denote $\Gamma_2 = \cup_{i=1}^4 \gamma_2^{(i)}$), and the mitral zone cross section Γ_3. (see Figure 5.4) The wall is considered as a thin elastic layer (shell) denoted G_d, where d is a thickness of the shell. At rest it occupies the space between surfaces Γ_1 and $\Gamma_{1,d}$ at the distance d from Γ_1 in the direction of the outer normal vector. The lateral boundary of the wall $\partial G_d \backslash (\Gamma_1 \cup \Gamma_{1,d})$ is perpendicular to Γ_1 and consists of five components. Four of them correspond to the cross sections of the vein walls and are denoted $\gamma_{2,d}^{(1)},...,\gamma_{2,d}^{(4)}$. The fifth corresponds to Γ_3 and is denoted $\gamma_{3,d}$.

The elastic wall moves and so Γ_1 also moves. The fluid motion equations are set in the time dependent domain G^t between the current in time position of the wall, Γ_2 and Γ_3. The current position of the wall is characterized by the unknown displacement vector $\mathbf{u}(x,t)$, where $x \in G_d$, so that the moving part of the boundary is $\Gamma_1^t = \{x + \mathbf{u}(x,t) \ : x \in \Gamma_1\}$. The equations determining displacements $\mathbf{u}(x,t)$ in the elastic wall are defined further.

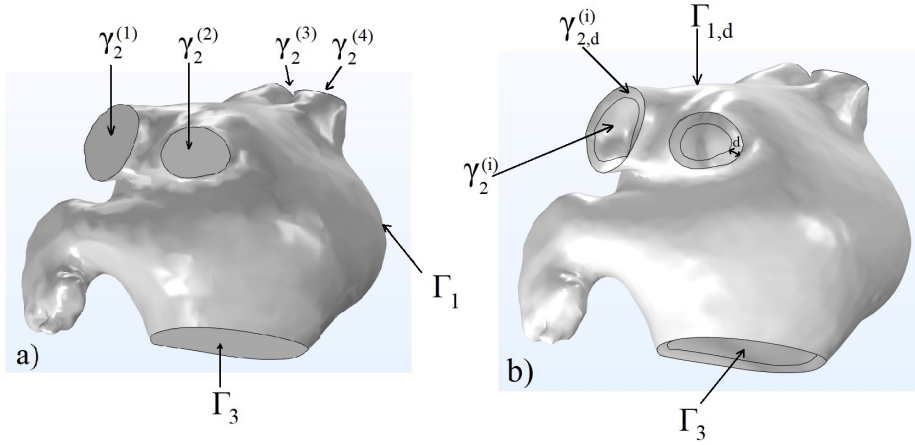

Figure 5.4 – Four pulmonary veins (inlets), mitral valve (outlet) domains and boundaries of geometry: a) Fluid domain; b) Solid domain.

The blood flow in the LA (domain G^t) is described by the Navier–Stokes equations

$$\begin{cases} \rho_f \mathbf{v}_t - \mu_f \Delta \mathbf{v} + \rho_f (\mathbf{v} \cdot \nabla)\mathbf{v} + \nabla p &= 0, \\ \text{div } \mathbf{v} &= 0, \end{cases} \tag{5.1}$$

where $\mathbf{v}$ is the blood velocity, p is the pressure function, $\rho_f > 0$ is the density

of the blood, and $\mu_f > 0$ is the constant dynamic viscosity of the blood, with the initial condition

$$\mathbf{v}(x,0) = 0, \tag{5.2}$$

and boundary or interface conditions on Γ_1, Γ_2, and Γ_3, which will be described below.

On Γ_2 the inflow boundary conditions are introduced as the given velocity

$$\mathbf{v}(x,t)|_{\Gamma_2} = \mathbf{g}(x,t), \tag{5.3}$$

where on each component $\gamma_2^{(i)}$ of Γ_2 function $\mathbf{g}$ is defined as follows.

Let $\tilde{x}_1, \tilde{x}_2$ be the local in-plane coordinates of $\gamma_2^{(i)}$, let $v_{P,i}(\tilde{x}_1, \tilde{x}_2, t), q(t)$ be the solution of the inverse heat problem set on $\gamma_2^{(i)} \times (0, +\infty)$:

$$\rho_f \frac{\partial v_{P,i}}{\partial t}(\tilde{x}_1, \tilde{x}_2, t) - \mu_f \Delta v_{P,i}(\tilde{x}_1, \tilde{x}_2, t) = q(t),$$
$$v_{P,i}|_{\partial\gamma_2^{(i)}} = 0, \quad v_{P,i}|_{t=0} = 0,$$

$$\int\limits_{\gamma_2^{(i)}} v_{P,j}(\tilde{x}_1, \tilde{x}_2, t) \mathrm{d}\tilde{x}_1 \mathrm{d}\tilde{x}_2 = \Phi(t) \frac{\text{mes } \gamma_2^{(i)}}{\sum_{j=1}^{4} \text{mes } \gamma_2^{(j)}}$$

with $\Phi(t)$ standing for the total inlet flux (see [76], [74]).

The tangential components of $\mathbf{g}$ are equal to zero, while the normal component $g_n(\tilde{x}_1, \tilde{x}_2, t)$ on $\gamma_2^{(i)}$ is defined as

$$g_n(\tilde{x}_1, \tilde{x}_2, t) = v_{P,i}(\tilde{x}_1, \tilde{x}_2, t).$$

Such structure of the inflow velocity corresponds to the non-stationary Poiseuille flow corresponding to the given flux depending on time. It corresponds to the flow in an infinite tube with cross section $\gamma_2^{(i)}$. So, these inflows approximate the blood comming to the inlets through some cylinders modeling the pulmonary veins. In this case the average velocity (flux divided by the cross section area) is the same for all four inlet cross sections and is equal to $F(t)$ introduced by the graph at Figure 5.5. Here $F(t) = \Phi(t)(\sum_{j=1}^{4} \text{mes } \gamma_2^{(j)})^{-1}$.

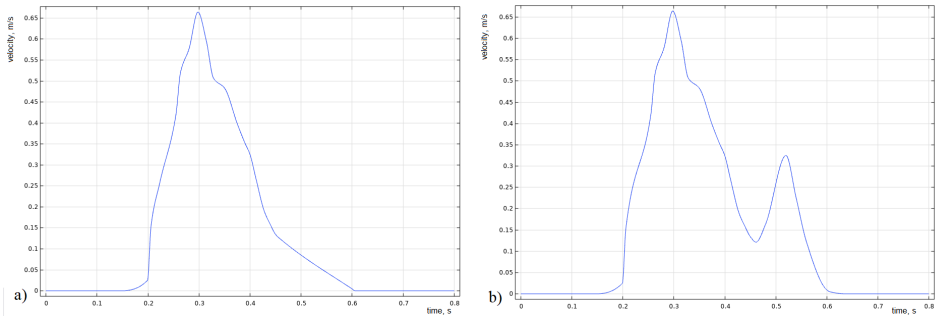

Figure 5.5 – Inlet average velocity $F(t)$: a) Atrial fibrillation; b) Sinus rhythm.

On Γ_3 the outflow boundary conditions are introduced as follows

$$\mathbf{v}_\tau(x,t)|_{\Gamma_3} = 0, \quad p(x,t)|_{\Gamma_3} = 0. \tag{5.4}$$

Here $\mathbf{v}_\tau$ is the tangential velocity at the boundary. The boundary condition $p(x,t)|_{\Gamma_3} = 0$ follows from a more general condition that the normal component of the normal stress is equal to zero:

$$\Big(-pI + \mu_f(\nabla\mathbf{v} + (\nabla\mathbf{v})^T)\mathbf{n}\Big) \cdot \mathbf{n} = 0.$$

Taking into account the equation $\mathrm{div}\mathbf{v} = 0$ and condition $\mathbf{v}_\tau = 0$ we derive that $p = 0$ on Γ_3.

The part Γ_1 of the boundary ∂G is the interface between the fluid and the elastic solid. The wall corresponding myocardium is described by the non-linear elasticity equations for the unknown displacement $\mathbf{u}(x,t)$ where $x \in G_d$:

$$\rho \frac{\partial^2 \mathbf{u}}{\partial t^2}(x,t) - \nabla \cdot (J\sigma \boldsymbol{F}^{-T})^T = 0, \tag{5.5}$$

where $\rho > 0$ is the density of the wall material, $\mathbf{F} = I + \nabla\mathbf{u}$ is the deformation gradient, $J\sigma\boldsymbol{F}^{-T}$ is the 1^{st} Piola-Kirchhoff stress, $J = \det \boldsymbol{F}$ is the Jacobian determinant, σ_{ij} is the stress tensor satisfying the linear Hooke's law (see [68]):

$$\sigma_{ij} = \lambda \sum_{k=1}^{3} \varepsilon_{kk}\delta_{ij} + 2\mu\varepsilon_{ij}, \tag{5.6}$$

where λ and μ are the Lamé parameters, δ_{ij} is the Kronecker's delta:

$$\delta_{ij} = \begin{cases} 0 & \text{if } i \neq j \\ 1 & \text{if } i = j, \end{cases}$$

while

$$\varepsilon_{ij} = \frac{1}{2}\Big(\frac{\partial u_i}{\partial x_j} + \frac{\partial u_j}{\partial x_i} + \sum_{k=1}^{3} \frac{\partial u_k}{\partial x_i}\frac{\partial u_k}{\partial x_j}\Big)$$

is the strain tensor. In the linear theory it is linearized as

$$\varepsilon_{ij} = \frac{1}{2}\Big(\frac{\partial u_i}{\partial x_j} + \frac{\partial u_j}{\partial x_i}\Big),$$

Note that the Lamé constants can be expressed via the Young modulus E and the Poisson ratio ν, $E > 0,\ -1 < \nu < 1/2$:

$$\lambda = \frac{E\nu}{(1+\nu)(1-2\nu)}, \quad \mu = \frac{E}{2(1+\nu)}. \tag{5.7}$$

This system of equations necessitates two initial conditions for $\mathbf{u}$:

$$\mathbf{u}(x,0) = 0, \quad \frac{\partial \mathbf{u}}{\partial t}(x,0) = 0, \quad x \in G_d, \tag{5.8}$$

boundary conditions on $\partial G_d \backslash (\Gamma_1 \cup \Gamma_{1,d})$ (clamped ends):

$$\mathbf{u}(x,t) = 0, \quad x \in \partial G_d \backslash (\Gamma_1 \cup \Gamma_{1,d}), \tag{5.9}$$

boundary condition on $\Gamma_{1,d}$ (applied pressure $p_{\text{wall}}(t)$ simulating the contractions of the wall displayed in Figure 5.6):

$$(J\sigma \boldsymbol{F}^{-T})^T \mathbf{n} = -p_{\text{wall}}(t)\mathbf{n}, \quad x \in \Gamma_{1,d}, \tag{5.10}$$

and finally the junction conditions on the moving interface Γ_1: the continuity of the velocity at the moving interface

$$\mathbf{v}(x + \mathbf{u}(x,t), t) = \frac{\partial \mathbf{u}}{\partial t}(x,t), \quad x \in \Gamma_1, \tag{5.11}$$

and the continuity of the stresses:

$$-(J\sigma \boldsymbol{F}^{-T})^T \mathbf{n} = (-pI + \mu_f(\nabla \mathbf{v} + (\nabla \mathbf{v})^T))\mathbf{n}, \quad x \in \Gamma_1, \tag{5.12}$$

$\mathbf{u}$ is an outer normal for G. As before we can replace the right-hand side of this condition by $-p\mathbf{n}$.

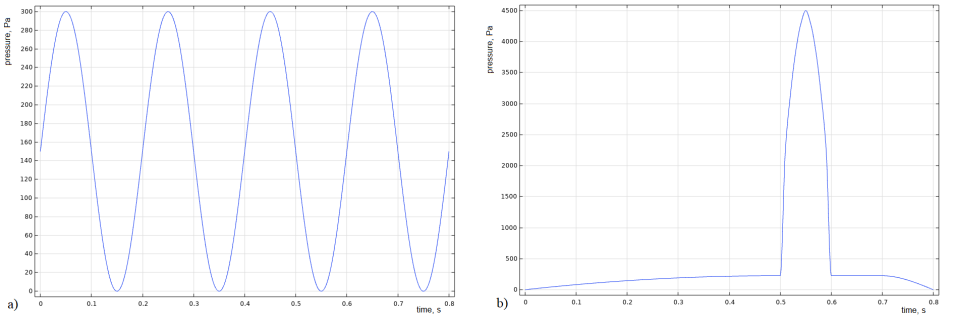

Figure 5.6 – Pressure load $p_{\text{wall}}(t)$ on the shell: a) Atrial fibrillation; b) Sinus rhythm.

The parameters of the model are taken as follows: $d = 2.5 \cdot 10^{-3}$ m, $\rho_f = \rho = 1050$ kg/m^3, $\mu_f = 3.5 \cdot 10^{-3}$ Pa$\cdot$s, $\nu = 0.47$, E belongs to the interval $[4 \cdot 10^4, 8 \cdot 10^5]$ Pa. We considered the Young modulus depending on time, following the contraction pressure $p_{\text{wall}}(t)$ graph:

$$E(t) = 4 \cdot 10^4 + p_{\text{wall}}(t)(8 \cdot 10^5 - 4 \cdot 10^4)/\max p_{\text{wall}},$$

i.e. strengthening when the heart wall muscles contract.

5.3.3 Uflyand–Mindlin shell approximation

To solve this problem numerically we used the COMSOL software. The thin layer G_d was approximated by the Uflyand–Mindlin shell model. According to the Uflyand–Mindlin shell theory the displacement vector $\mathbf{u}$ is supposed to have the following form:

$$\mathbf{u}(\tilde{x}_1, \tilde{x}_2, \tilde{x}_3, t) = \boldsymbol{\eta}(\tilde{x}_1, \tilde{x}_2, t) + \tilde{x}_3 \boldsymbol{\zeta}(\tilde{x}_1, \tilde{x}_2, t), \tag{5.13}$$

where $\tilde{x}_1$ and $\tilde{x}_2$ are the in-plane local coordinates of the shell, $\tilde{x}_3 \in [-d/2, d/2]$ is the normal coordinate, equal to zero on the mid-surface $\Gamma_{1,d/2}$ (at the distance $d/2$ from Γ_1 and from $\Gamma_{1,d}$, see Figure 5.7), $\boldsymbol{\eta}(\tilde{x}_1, \tilde{x}_2, t)$ is the displacement vector of the mid-surface of the shell and $\boldsymbol{\zeta}(\tilde{x}_1, \tilde{x}_2, t)$ is the angular displacement of shell normal ($\boldsymbol{\zeta} \cdot \mathbf{n} = 0$). Further, for the shell equations theory $\Gamma_{1,d/2}$ is replaced (approximated) by Γ_1.

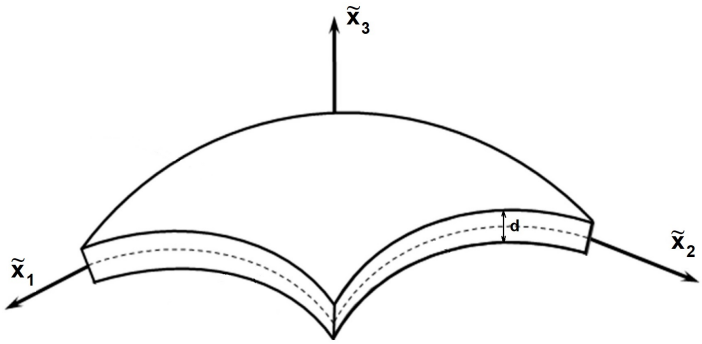

Figure 5.7 – Local coordinates for shell

The first condition at the interface is the continuity of the velocity on moving boundary:

$$\mathbf{v}(x+\boldsymbol{\eta}(\tilde{x}_1,\tilde{x}_2,t),t)=\frac{\partial\boldsymbol{\eta}}{\partial t}(\tilde{x}_1,\tilde{x}_2,t). \tag{5.14}$$

The second condition relates the unknown functions $\boldsymbol{\eta},\boldsymbol{\zeta}$ and the pressure p by the system of equations of motion of the shell. This system consists of two equations corresponding to the second order time derivatives of $\boldsymbol{\eta},\boldsymbol{\zeta}$ in the left-hand side. To get these equations at some point $\tilde{x}$ of the interface Γ_1 let us expand the expression $\nabla\cdot((J\sigma\boldsymbol{F}^{-T})^T)$ with $\mathbf{u}(\tilde{x}_1,\tilde{x}_2,\tilde{x}_3,t)$ replaced by the sum (5.13) according to the first order Taylor's formula with respect to the normal variable $\tilde{x}_3$:

$$\nabla\cdot((J\sigma\boldsymbol{F}^{-T})^T)=\boldsymbol{\Phi}[\boldsymbol{\eta},\boldsymbol{\zeta}](\tilde{x}_1,\tilde{x}_2,t)+\tilde{x}_3\boldsymbol{\Psi}[\boldsymbol{\eta},\boldsymbol{\zeta}](\tilde{x}_1,\tilde{x}_2,t)+o(\tilde{x}_3),$$

where $\boldsymbol{\Phi}[\boldsymbol{\eta},\boldsymbol{\zeta}],\boldsymbol{\Psi}[\boldsymbol{\eta},\boldsymbol{\zeta}]$ are expressions containing functions $\boldsymbol{\eta},\boldsymbol{\zeta}$ and their space derivatives of order one and two. Then the second condition has the following form:

$$\begin{cases} \rho\dfrac{\partial^2\boldsymbol{\eta}}{\partial t^2}(\tilde{x}_1,\tilde{x}_2,t)=\boldsymbol{\Phi}[\boldsymbol{\eta},\boldsymbol{\zeta}](\tilde{x}_1,\tilde{x}_2,t)+d^{-1}(-p_{\text{wall}}+p)\mathbf{n}, \\ \rho\dfrac{\partial^2\boldsymbol{\zeta}}{\partial t^2}(\tilde{x}_1,\tilde{x}_2,t)=\boldsymbol{\Psi}[\boldsymbol{\eta},\boldsymbol{\zeta}](\tilde{x}_1,\tilde{x}_2,t). \end{cases} \tag{5.15}$$

The second equation here corresponds to the momentum balance.

The initial conditions for the shell are:

$$\boldsymbol{\eta}(\tilde{x}_1,\tilde{x}_2,0)=0,\quad \frac{\partial\boldsymbol{\eta}}{\partial t}(\tilde{x}_1,\tilde{x}_2,0)=0,\quad \boldsymbol{\zeta}(\tilde{x}_1,\tilde{x}_2,0)=0,$$
$$\frac{\partial\boldsymbol{\zeta}}{\partial t}(\tilde{x}_1,\tilde{x}_2,0)=0,\quad \tilde{x}_1,\tilde{x}_2\in\Gamma_1. \tag{5.16}$$

The boundary conditions for the shell are chosen as follows:

$$\boldsymbol{\eta}(\tilde{x}_1,\tilde{x}_2,t)=0,\quad \boldsymbol{\zeta}(\tilde{x}_1,\tilde{x}_2,t)=0,\quad \tilde{x}_1,\tilde{x}_2\in\partial\Gamma_2 \tag{5.17}$$

$$\boldsymbol{\eta}(\tilde{x}_1,\tilde{x}_2,t)=0,\ \ M_{nn}(\tilde{x}_1,\tilde{x}_2,t)=0,\ \ M_{n\tau}(\tilde{x}_1,\tilde{x}_2,t)=0,\ \ \tilde{x}_1,\tilde{x}_2\in\partial\Gamma_3, \tag{5.18}$$

where M_{nn} is the normal moment at the boundary of Γ_3, while τ is the tangential direction (for example, if x_1 is the normal direction, then $M_{11}(\tilde{x}_1,\tilde{x}_2,t)=0, M_{21}(\tilde{x}_1,\tilde{x}_2,t)=0$).

Here the moments are defined as $M=\int\limits_{-d/2}^{d/2}\tilde{x}_3 J\sigma\boldsymbol{F}^{-T}\mathrm{d}\tilde{x}_3$ (the leading part of the Taylor's expansion).

Note that using the ALE technique with moving mesh the computed in time dependent domain G^t velocity $\mathbf{v}$ and pressure p can be presented in the points of the reference domain G, so that, for example, $\mathbf{v}(x,t),\ x\in G^t$ is presented in the points $(\hat{x},t)$, where $x-\hat{x}=\mathbf{u}(\hat{x},t)$ the displacement of the point $\hat{x}$.

The direct COMSOL computations of this model often demonstrate bad convergence. It is explained as follows. COMSOL uses the implicit numerical schemes, and for each time step it needs to solve a big algebraic nonlinear system of equations. The solver is based on Newton's method which is very sensitive to the choice of the initial approximation. That is why we solve the FSI problem in two steps: first we solve the Navier–Stokes equations (5.1) with non-moving wall, i.e. in the domain G with initial condition (5.2) and boundary conditions (5.3) on Γ_2 and (5.4) on Γ_3, while the boundary conditions on Γ_1 are replaced by

$$\mathbf{v}=0,\quad x\in\Gamma_1.$$

Then at the second step the FSI problem is solved using the initial approximations from the first step. This approach improves the convergence of the solver.

5.4 Results

We possess data concerning two distinct patients diagnosed an AF: we denote these as PATIENT **A** (with "chicken wing" geometry), who had a stroke, and PATIENT **B** (with "windsock" geometry), who has not got a stroke. After the stroke PATIENT **A** recovered to sinus rhythm and then the blood flow velocity through mitral valve was measured by Doppler technique (see Figure 5.8).

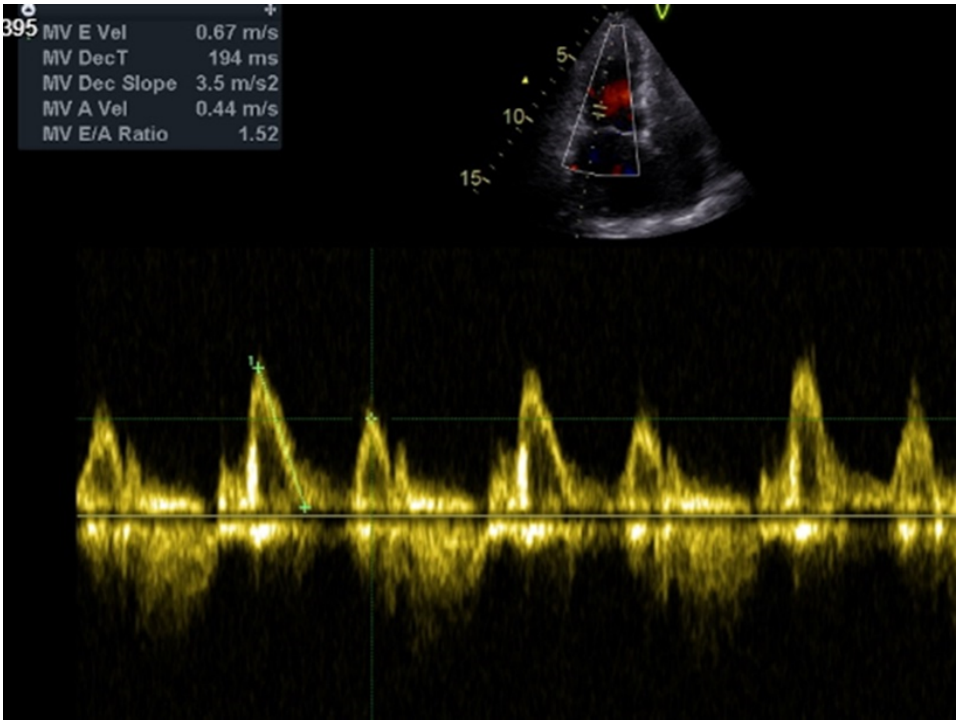

Figure 5.8 – Blood flow through mitral valve during sinus rhythm (PATIENT **A** specific data)

We utilize this graph to prescribe the average velocity $F(t)$ in boundary condition (5.3) (see Figure 5.5 b)).

Given the inherent limitations in capturing *in vivo* blood velocity measurements within LAA, we are able to compute the magnitude of blood velocity within this area. We validate our simulations comparing the computed normal velocity at the inlet point of the LAA, known as the ostium, with the measured one.

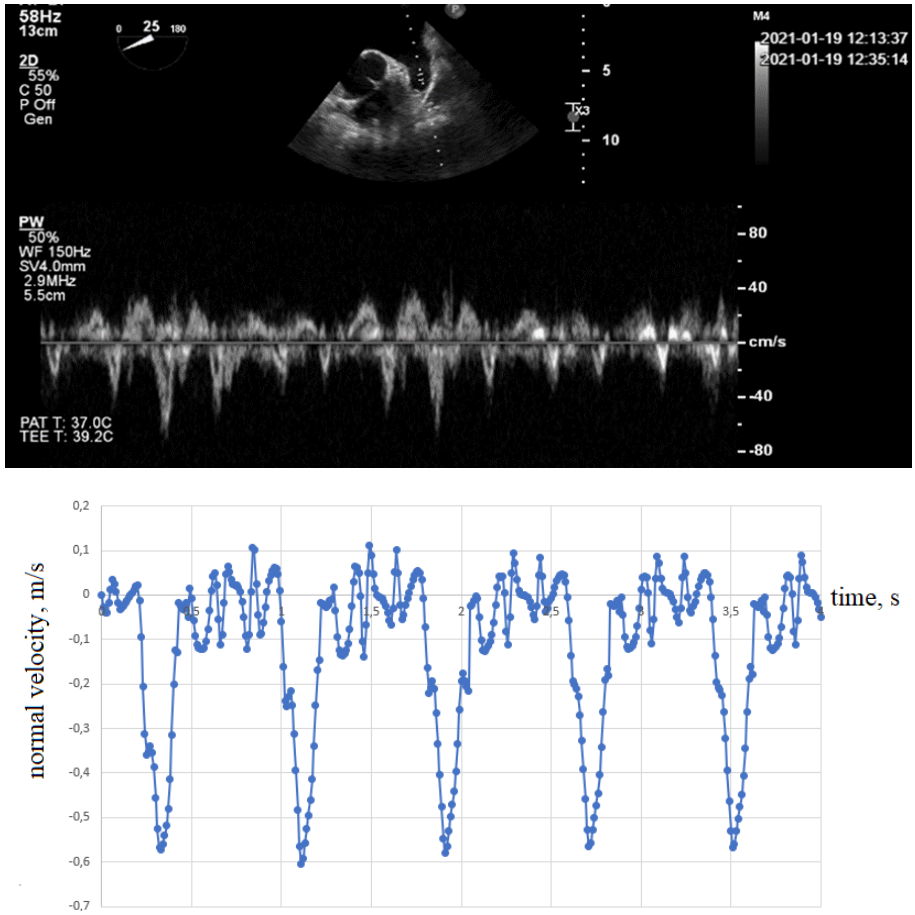

Figure 5.9 – At the higher picture the measured normal blood velocity at the ostium of LAA of PATIENT **A** is presented, on the lower one the computed normal blood velocity at the ostium of LAA of PATIENT **A** is shown.

Figure 5.9 shows the similar order of the normal velocity at the ostium of LAA (AF case), i.e. Doppler measurements are compared to the computer simulations.

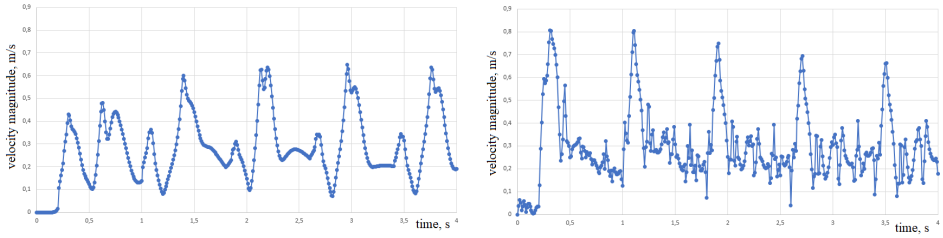

Figure 5.10 – Blood flow velocity magnitude of PATIENT' s **A** ostium of the LAA during AF with Hard Wall on the left hand side and with FSI on the right hand side.

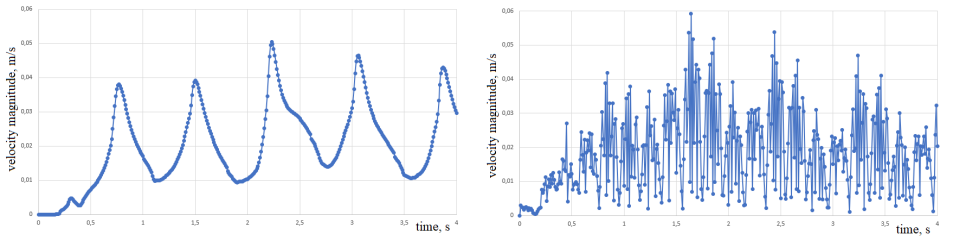

Figure 5.11 – Blood flow velocity magnitude of PATIENT' s **A** center of the LAA during AF with Hard Wall on the left hand side and with FSI on the right hand side.

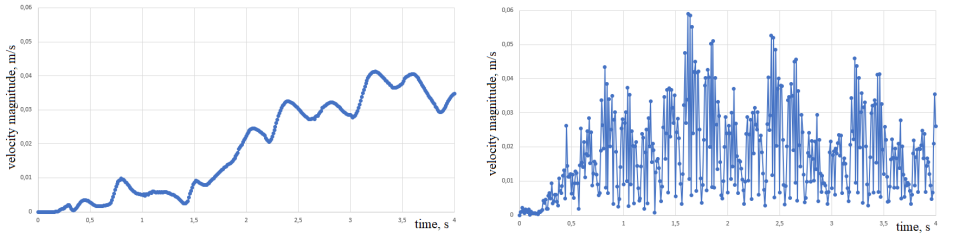

Figure 5.12 – Blood flow velocity magnitude of PATIENT' s **A** lateral part of the LAA during AF with Hard Wall on the left hand side and with FSI on the right hand side.

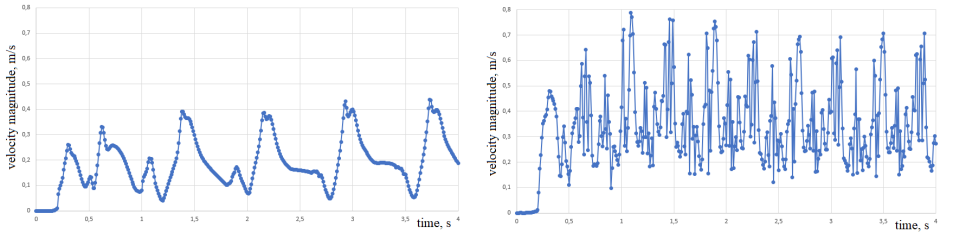

Figure 5.13 – Blood flow velocity magnitude of PATIENT' s **A** ostium of the LAA during sinus rhythm with Hard Wall on the left hand side and with FSI on the right hand side.

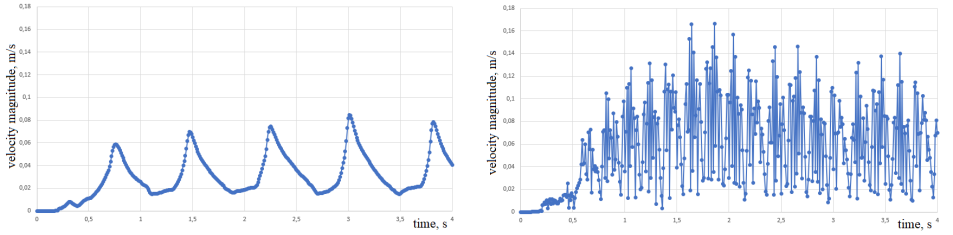

Figure 5.14 – Blood flow velocity magnitude of PATIENT' s **A** center of the LAA during sinus rhythm with Hard Wall on the left hand side and with FSI on the right hand side.

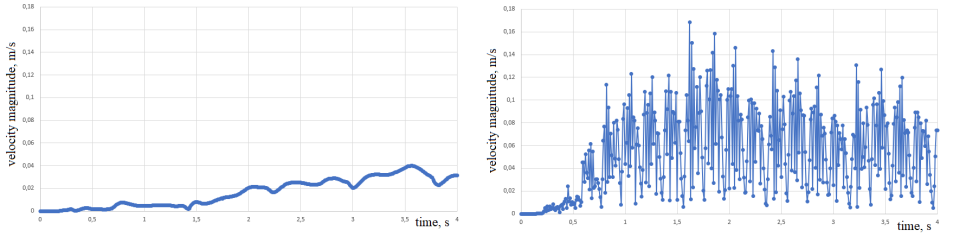

Figure 5.15 – Blood flow velocity magnitude of PATIENT' s **A** lateral part of the LAA during sinus rhythm with Hard Wall on the left hand side and with FSI on the right hand side.

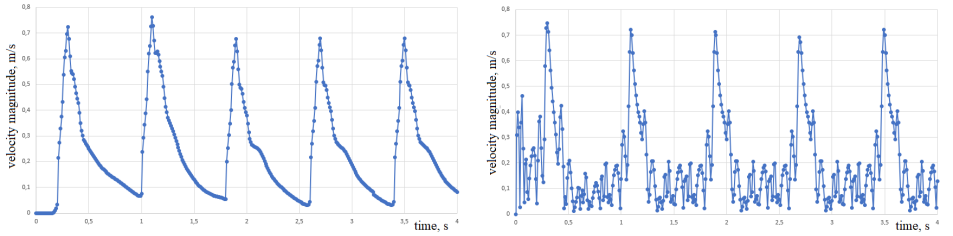

Figure 5.16 – Blood flow velocity magnitude of PATIENT' s **B** ostium of the LAA during AF with Hard Wall on the left hand side and with FSI on the right hand side.

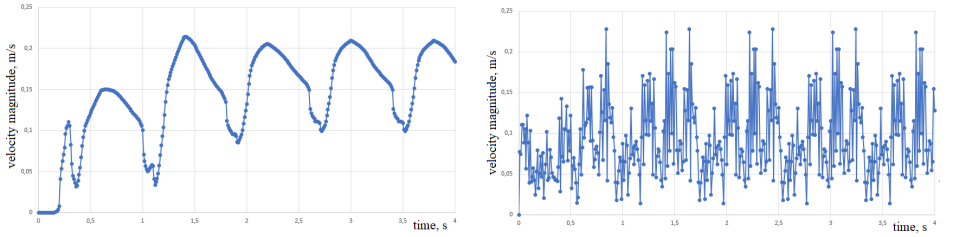

Figure 5.17 – Blood flow velocity magnitude of PATIENT' s **B** center of the LAA during AF with Hard Wall on the left hand side and with FSI on the right hand side.

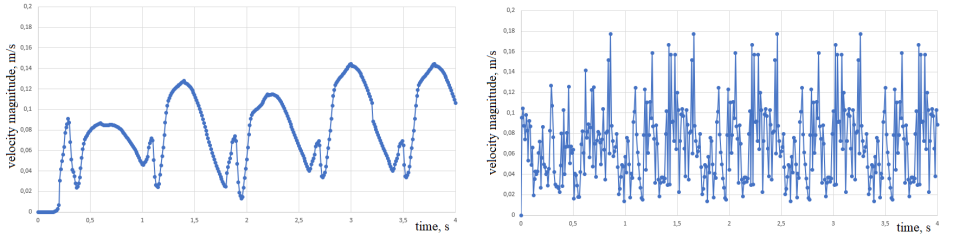

Figure 5.18 – Blood flow velocity magnitude of PATIENT' s **B** lateral part of the LAA during AF with Hard Wall on the left hand side and with FSI on the right hand side.

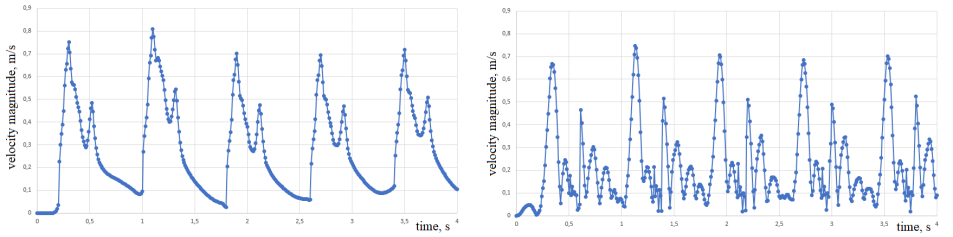

Figure 5.19 – Blood flow velocity magnitude of PATIENT' s **B** ostium of the LAA during sinus rhythm with Hard Wall on the left hand side and with FSI on the right hand side.

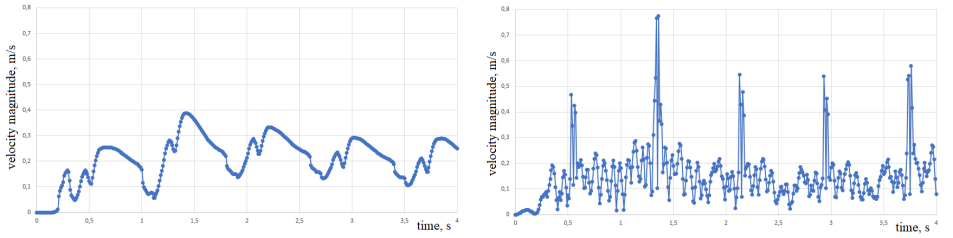

Figure 5.20 – Blood flow velocity magnitude of PATIENT' s **B** center of the LAA during sinus rhythm with Hard Wall on the left hand side and with FSI on the right hand side.

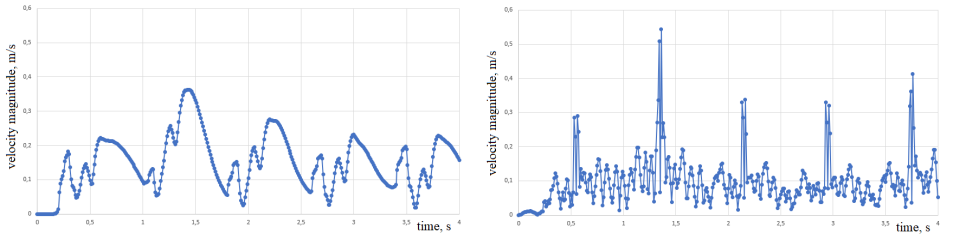

Figure 5.21 – Blood flow velocity magnitude of PATIENT' s **B** lateral part of the LAA during sinus rhythm with Hard Wall on the left hand side and with FSI on the right hand side.

For each of two patients we fix three points in the LAA: one at the inlet to the LAA (ostium), one in the middle of the LAA (center) and one near the wall (lateral). Figures 5.10, 5.11, 5.12 present the results of computer simulations (velocity magnitude) for the LAA of PATIENT **A** in case of AF with a rigid (not moving) wall on the left and with FSI (moving wall) on the right. Figures 5.13, 5.14, 5.15 present analogous simulations for the LAA of the PATIENT **A** in the case of sinus rhythm. Figures 5.16, 5.17, 5.18 show the graphs of the velocity magnitude for the LAA of PATIENT **B** in case of AF, and, finally, Figures 5.19, 5.20, 5.21 present the velocity magnitude for the LAA of PATIENT **B** in case of sinus rhythm. All upmentioned pictures

show the satisfactory stabilization of the velocity to a periodic regime after three heartbeats. These pictures show that in the case of PATIENT **A** (the one with a stroke) the magnitude order is similar for the rigid wall and FSI computations in the case of AF, but differs significantly for the sinus rhythm, while for the PATIENT **B** (the one without a stroke) the magnitude order is the same in both AF and sinus rhythm cases. It shows that probably the mobility of the wall is more important for the geometry of LAA of the PATIENT **A** (who had a stroke) than for the geometry of the PATIENT **B** (who had not). Thus, hypothetically one can use the comparison of the rigid wall and FSI simulations for AF and sinus rhythm cases to evaluate the type of geometry with a higher risk of stroke. Another guess can be done for the case of AF simulations: the magnitudes of the velocity in the LAA are similar for the rigid wall computations and for the FSI model. Note that the rigid wall simulations are much simpler and less time-consumable than FSI.

As we can see on Figure 5.22, PATIENT **A** had in LAA velocity magnitude which is obviously lower than PATIENT' s **B**. So, the lower velocity magnitude corresponds to the higher risk of thrombi formation. Notice, that PATIENT **A** has "chicken wing" LAA geometry (which according to [85] is at the lowest risk of stroke), while PATIENT **B** has "windsock" LAA geometry. It shows that the prediction of the stroke via the simulations of the blood flow in the LA may be more realistic than the statistical evaluation based on the classification of the geometry of the LAA.

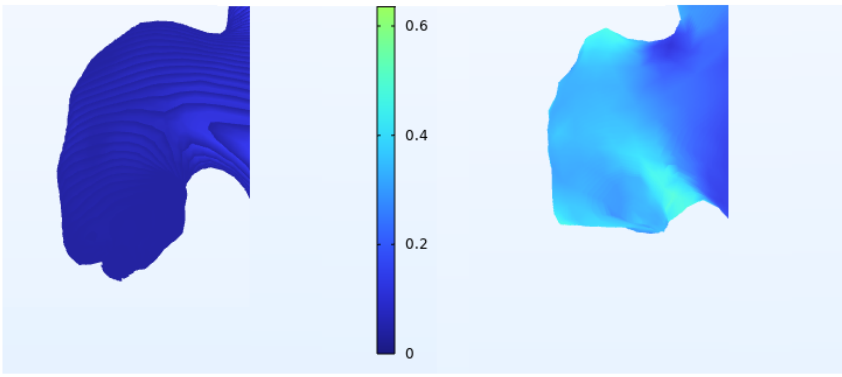

Figure 5.22 – Computed blood flow velocity magnitude (m/s) in the LAA during AF: Patient **A** on the left, Patient **B** on the right (deep blue color corresponds to a lower velocity magnitude, while light blue corresponds to a higher velocity.

Since we notice that PATIENT **A** has got lower blood flow velocity magnitude in the LAA, we choose several points and we compute maximal blood flow velocity magnitude in these points as shown on Figure 5.23

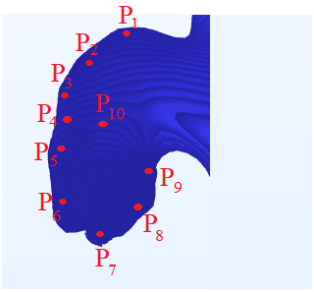

Point	Velocity magnitude, m/s
P_1	0.0631
P_2	0.0534
P_3	0.0478
P_4	0.0508
P_5	0.0423
P_6	0.0389
P_7	0.0293
P_8	0.0321
P_9	0.0336
P_{10}	0.0585

Figure 5.23 – Computed blood flow velocity magnitude (m/s) in several points of the PATIENT's **A** LAA during AF.

In comparison with the center of the LAA (point P_{10}) we can see, that in the points P_i, $i = 6, ..., 9$ the computed blood flow velocity magnitude is lower, so near these points could be stagnation zones where thrombogenesis occurs.

Chapter 6

Conclusions

For the accurate study and understanding of the hemodynamics several aims were solved:

I. The existence and uniqueness of the solution of time-periodic Navier–Stokes problem in an infinite cylinder with a prescribed flow rate $F(t) \in L^2(0,T)$ under minimal regularity of data was proved.

II. The FSI model was reduced into a 4^{th} order simplified PDE. Computation of blood flow velocity in a single vessel considered as cylinder and a Y-shaped network of vessels considered as connected cylinders utilizing both approaches: the FSI model containing numerical solution of non-stacionary Navier–Stokes equations with a moving wall and the derived less time consumable 4^{th} order PDE showed results with no significant difference.

III. An FSI model of the blood flow in patient-specific LA is introduced. The simulations including the imaging, segmentation, cleaning (noise reduction), domain generation and FSI computational fluid dynamics within patient-specific LA are provided. The computed blood flow velocity in the developed model is compared with the obtained one by Doppler measurements at the ostium of the LAA. The correlation of the presence of stagnation zones in LAA with the stroke risk is studied. The COMSOL simulations of the FSI model are quite challenging and often the direct application of the code leads to the fail of the convergence. It is pointed out that the two-step computations (rigid wall at the first step, and FSI at the second step) improves the convergence of the latter code.

Bibliography

[1] R. A. Adams. *Sobolev Spaces*, Academic Press, New York, San Francisco, London (1975).

[2] L. Alinezhad, F. Ghalichi, M. Ahmadlouydarab, M. Chenaghlou. Left atrial appendage shape impacts on the left atrial flow hemodynamics: A numerical hypothesis generating study on two cases, *Computer Methods and Programs in Biomedicine*, **213**, 106506 (2022).

[3] N. M. Al-Saady, O. A. Obel, A. J. Camm. Left atrial appendage: structure, function, and role in thromboembolism, *Heart*, **82**, 547–54 (1999).

[4] M. Alquwaizani, L. Buckley, C. Adams, J. Fanikos. Anticoagulants: A Review of the Pharmacology, Dosing, and Complications, *Current Emergency and Hospital Medicine Reports*, **1**, 83–97 (2013).

[5] M. Anand, K. Rajagopal, K. R. Rajagopal. A model for the formation and lysis of blood clots, *Pathophysiology of Haemostasis and Thrombosis*, **34** (2-3), 109-120 (2006).

[6] N. Bakhvalov, G. P. Panasenko. *Homogenisation: Averaging Processes in Periodic Media*, Nauka, Moscow, 352 (1984); English translation: Kluwer, Dordrecht/Boston/London, 366 (1989).

[7] M. Bansal, R. R. Kasliwal. Echocardiography for left atrial appendage structure and function, *Indian Heart Journal*, **64**, 469–75 (2012).

[8] G. K. Batchelor. *An Introduction to Fluid Dynamics*, Cambridge University Press, Cambridge (2002).

[9] H. Beirão da Veiga. Time-periodic solutions of the Navier–Stokes equations in an unbounded cylindrical domains. Leray's problem for periodic flows, *Archive for Rational Mechanics and Analysis*, **178**, 301-325 (2005)

[10] F. Berntsson, A. Ghosh, V. A. Kozlov, S. A. Nazarov. A one-dimensional model of blood flow through a curvilinear artery, *Applied Mathematical Modelling*, **63**, 633-643 (2018).

[11] J. L. Blackshear, J. A. Odell. Appendage obliteration to reduce stroke in cardiac surgical patients with atrial fibrillation, *The Annals of Thoracic Surgery*, **61**, 755–9 (1996).

[12] G. M. Bosi, A. Cook, R. Rai, L. J. Menezes, S. Schievan, R. Torii, G. Burriesci. Computational Fluid Dynamic Analysis of the Left Atrial Appendage to Predict Thrombosis Risk, *Frontiers in Cardiovascular Medicine*, **5** (2018).

[13] A. Bouchnita, A. Tosenberger, V. Volpert. On the regimes of blood coagulation, *Applied Mathematical Letters*, **51**, 74-79 (2016).

[14] J. Boussinesq. *Essaii sur la Théorie des Eaux Courrantes*, in Mémoires Présentés par Divers Savants de l'Académie des Sciences de l'Institut de France Impr Nationale (1877).

[15] M. Bucelli, A. Zingaro, P. C. Africa, I. Fumagalli, L. Dede', A. Quarteroni. A mathematical model that integrates cardiac electrophysiology, mechanics, and fluid dynamics: Application to the human left heart, *Numerical Methods in Biomedical Engineering*, **39**(3), e3678 (2023).

[16] S. Čanić, A. Mikelić. Effective equations modeling the flow of a viscous incompressible fluid through a long elastic tube arising in the study of blood flowthrough small arteries, *SIAM Journal on Applied Dynamical Systems*, **2**, 431-463 (2003).

[17] S. Čanić, J. Tambača, G. Guidoboni, A. Mikelić, C. J. Hartley, D. Rosenstrauch. Modeling viscoelastic behavior of arterial walls and their interaction with pulsate blood flow, *SIAM Journal on Applied Mathematics*, **67**, 164-193 (2006).

[18] J. R. Cannon. The solution of the heat equation subject to specification of energy, *Quarterly of Applied Mathematics*, **21**, 155–160 (1963).

[19] J. R. Cannon. *The One-Dimensional Heat Equation*, Addison-Wesley, Menoro Park (1984).

[20] O. Darrigol. Between hydrodynamics and elasticity theory: the first five births of the Navier–Stokes equation, *Archive for History of Exact Sciences*, **56**(2), 95-150 (2002).

[21] C. V. De Simone, P. Gaba, J. Tri, F. Syed, A. Noheria, S. J. Asirvatham. A review of the relevant embryology, pathohistology, and anatomy of the left atrial appendage for the invasive cardiac electrophysiologist, *Journal of Atrial Fibrillation*, **8**, 81–87 (2015).

[22] B. Desjardins, M. J. Esteban, C. Grandmont, P. le Talec. Weak solutions for a fluid-structure interaction model, *Revista Matemática Complutense*, **14**, 523-538 (2001).

[23] L. Di Biase, P. Santangeli, M. Anselmino, P. Mohanty, I. Salvetti, S. Gili R. Horton, J. E. Sanchez, R. Bai, S. Mohanty, A. Pump, M. Cereceda Brantes, G. J. Gallinghouse, J. D. Burkhardt, F. Cesarani, M. Scaglione, A. Natale, F. Gaita. Does the left atrial appendage morphology correlate with the risk of stroke in patients with atrial fibrillation? Results from a multicenter study, *Journal of the American College of Cardiology*, **60**, 531-538 (2012).

[24] G. Elert. *The Physics Hypertextbook* (1998-2019), https://physics.info/.

[25] A. L. Fogelson, R. D. Guy. Platelet-wall interactions in continuum models of platelet thrombosis: Formulation and numerical solution, *Mathematical Medicine and Biology*, **21**(4), 293-334 (2004).

[26] A. Fogelson. Cell-based models of blood clotting, single-cell-based model in biology and medicine, in: A. R. A. Anderson, M. A. J. Chaplain, K. A. Rejniak (Eds.), *Mathematics and Biosciences in Interaction*, Birkhäuser Verlag, Basel, 243–269 (2007).

[27] L. Formaggia, D. Lamponi, A. Quarteroni. One-dimensional models for blood flow in arteries, *Journal of Engineering Mathematics* , **47**, 251–276 (2003).

[28] G. Gaidulis, M. Selmi, D. Zakarkaitė, A. Aidietis, R. Kačianauskas. Modelling and simulation of mitral valve for transapical surgery application, *Nonlinear Analysis: Modelling and Controle*, **24**(4), 485-502 (2019).

[29] G. P. Galdi and A. M. Robertson. The relation between flow rate and axial pressure gradient for time-periodic Poiseuille flow in a pipe, *Journal of Mathematical Fluid Mechanics*, **7**, 215-223 (2005).

[30] G. P. Galdi, T. Hishida. Attainability of time-periodic flow of a viscous liquid past an oscillating body, *Journal of Evolution Equations* (2021).

[31] G. P. Galdi. On the Self-propulsion of a Rigid Body in a Viscous Liquid by Time-Periodic Boundary Data, *Journal of Mathematical Fluid Mechanics*, **22**, 61 (2020).

[32] G. P. Galdi. On the problem of steady bifurcation of a falling sphere in a Navier–Stokes liquid, *Journal of Mathematical Physics*, **61**(8) (2020).

[33] G. P. Galdi, K. Pileckas, A. L. Silvestre. On the unsteady Poiseuille flow in a pipe, *Zeitschrift für Angewandte Matematik und Physik*, **58**, 994-1007 (2007).

[34] M. García-Villalba, L. Rossini, A. Gonzalo, D. Vigneault, P. Martinez-Legazpi, E. Duran, O. Flores, J. Bermejo, E. McVeigh, A. M. Kahn, J. C. del Álamo. Demonstration of patient-specific simulations to assess left atrial appendage thrombogenesis risk, *Frontiers in Physiology*, **12**, 596 (2021).

[35] D. Gonzalez-Casal, T. Datino, N. Soto, J. González-Panizo, D. Sánchez-Quintana, Y. Macias, J. Á. Cabrera. Anatomy of the left atrial appendage for the interventional cardiologist, *Herzschrittmachertherapie+Elektrophysiologie*, **33**, 195–202 (2022).

[36] R. P. Gilbert, A. Mikelić. Homogenizing the acoustic properties of the seabed: Part I, *Nonlinear Analysis: Theory, Methods & Applications*, **40**, 185-212 (2000).

[37] C. Grandmont, Y. Maday. Existence for an unsteady fluid-structure interaction problem, *Mathematical Modelling and Numerical Analysis*, **34**, 609-636 (2000).

[38] M. Handke, A. Harloff, A. Hetzel, M. Olschewski, C. Bode, A. Geibel. Left atrial appendage flow velocity as a quantitative surrogate parameter for thromboembolic risk: determinants and relationship to spontaneous echocontrast and thrombus formation–a transesophageal echocardiographic study in 500 patients with cerebral ischemia, *Journal of the American Society of Echocardiography*, **18**(12), 1366-1372 (2005).

[39] S. Y. Ho, J. A. Cabrera, D. Sanchez-Quintana. Left atrial anatomy revisited, *Circulation: Arrhythmia and Electrophysiology*, **5**, 220–228 (2012).

[40] S. Jacobsen, L. Haugan, T. A. Hammer, E. Kalogiannidis. Flow conditions of fresh mortar and concrete in different pipes, *Cement and Concrete Research*, **39**, 997-1006 (2009).

[41] S. W. Jordan, E. L. Chaikof. Simulated surface-induced thrombin generation in a flow field, *Biophysics Journal*, **101**, 276–286, (2011).

[42] H. Kamel, P. M. Okin, M. Elkind, C. Iadecola. Atrial fibrillation and mechanisms of stroke: time for a new model, *Stroke*, **47**(3), 895–900 (2016).

[43] N. Karim, S. Y. Ho, E. Nicol, W. Li, F. Zemrak, V. Markides, V. Reddy, T. Wong. The left atrial appendage in humans: structure, physiology, and pathogenesis, *Europace*, **22**(1), 5-18 (2020).

[44] O. A. Ladyzhenskaya. The Boundary Value Problems of Mathematical Physics, *Springer–Verlag*, New York, Berlin, Heidelberg, Tokyo (1985).

[45] P. K. Lamm. Surveys on Solution Methods for Inverse Problems, *Springer*, Vienna, New York (2000).

[46] L. D. Landau, E. M. Lifshitz. Fluid Mechanics, *Pergamon Press*, Oxford, New York, Beijing, Frankfurt, Sydney, Tokyo, Toronto (1987).

[47] J. M. Lee, J. Shim, J. S. Uhm, Y. J. Kim, H. J. Lee, H. N. Pak, M. H. Lee, B. Joung. Impact of increased orifice size and decreased flow velocity of left atrial appendage on stroke in nonvalvular atrial fibrillation, *The American Journal of Cardiology*, **113**, 963–969 (2014).

[48] A. I. Lobanov, T. K. Starozhilova. The effect of convective flows on blood coagulation processes, *Pathophysiology of Haemostasis and Thrombosis*, **34**(2–3), 121–134 (2005).

[49] I. Malakhova-Ziablova, G. Panasenko, R. Stavre. Asymptotic analysis of a thin rigid stratified elastic plate - viscous fluid interaction problem, *Applicable Analysis*, **95**, 1467-1506 (2016).

[50] E. N. Marieb, K. Hoehn. *The cardiovascular system: blood vessels. Human anatomy & physiology*, 9-th edition, Pearson Education, 712 (2013).

[51] A. Masci, L. Barone, L. Dedè, M. Fedele, C. Tomasi, A. Quarteroni, C. Corsi. The impact of left atrium appendage morphology on stroke risk assessment in atrial fibrillation: a computational fluid dynamics study, *Frontiers in Physiology*, **9**, 1938 (2019).

[52] P. K. Mason, D. E. Lake, J. P. Dimarco, J. D. Ferguson, J. M. Mangrum, K. C. Bilchick, L. P. Moorman, J. R. Moorman. Impact of the CHA2DS2-VASc score on anticoagulation recommendations for atrial fibrillation, *The American Journal of Medicine*, **125**(6), 603.e1-6 (2012).

[53] H. N. Mayrovitz. Skin capillary metrics and hemodinamics in the hairless mouse, *Microvascular Research*, **43**, 46-59 (1992).

[54] A. Mikelić, G. Guidoboni, S. Čanić. Fluid-structure interaction in a pre-stressed tube with thick elastic walls. I. The stationary Stokes problem, *Networks and Heterogeneous Media*, **2**, 397-423 (2007).

[55] A. Moorman, S. Webb, N. A. Brown, W. Lamers, R. H. Anderson. Development of the heart: (1) formation of the cardiac chambers and arterial trunks, *Heart*, **89**, 806–814 (2003).

[56] M. Nica. Eigenvalues and Eigenfunctions of the Laplacian, *The Waterloo Mathematics Review*, **1**(2) (2011).

[57] J. J. Nieto. Impulsive resonance periodic problems of first order, *Applied Mathematics Letters*, **15**(4), 489-493 (2002).

[58] M. Okada, K. Inoue, N. Tanaka, K. Tanaka, Y. Hirao, K. Iwakura, Y. Egami, M. Masuda, T. Watanabe, H. Minamiguchi, T. Oka, S. Hikoso, A. Sunaga, K. Okada, D. Nakatani, Y. Sotomi, Y. Sakata. Impact of left atrial appendage flow velocity on thrombus resolution and clinical outcomes in patients with atrial fibrillation and silent left atrial thrombi: insights from the LAT study, *EP Europace*, **26**(5), euae120, (2024).

[59] G. P. Panasenko. *Multi-Scale Modelling for Structures and Composites*, Springer, Dordrecht, 398 (2005).

[60] G. P. Panasenko, R. Stavre. Asymptotic analysis of a periodic flow in a thin channel with visco-elastic wall, *Journal de Mathématiques Pures et Appliquées*, **85**, 558-579 (2006).

[61] G. P. Panasenko, Y. Sirakov, R. Stavre. Asymptotic and numerical modeling of a flow in a thin channel with visco-elastic wall, *International Journal for Multiscale Computational Engineering*, **5**, 473-482 (2007).

[62] G. P. Panasenko, R. Stavre. Asymptotic analysis of a non-periodic flow with variable viscosity in a thin elastic channel, *Networks and Heterogeneous Media*, **5**, 783-812 (2010).

[63] G. P. Panasenko, R. Stavre. Asymptotic analysis of a viscous fluid-thin plate interaction: periodic flow, *Mathematical Methods in the Applied Sciences*, **24**, 1781-1822 (2014).

[64] G. P. Panasenko, R. Stavre. Viscous fluid-thin elastic plate interaction: asymptotic analysis with respect to the rigidity and density of the plate, *Applied Mathematical Optimization*, **81**, 141–194 (2020), DOI: 10.1007/s00245-018-9480-2.

[65] G. P. Panasenko, R. Stavre. Viscous fluid-thin cylindrical elastic body interaction: asymptotic analysis on contrasting properties, *Applicable Analysis*, **98**, 162-216 (2019).

[66] G. P. Panasenko, R. Stavre. Three dimensional asymptotic analysis of an axisymmetric flow in a thin tube with thin stiff elastic wall, *Journal of Mathematical Fluid Mechanics*, **22**, 20-35 (2020).

[67] G. Panasenko. Asymptotic expansion of the solution of Navier–Stokes equation in a tube structure, *Comptes Rendus de l'Académie des Sciences - Series IIB - Mechanics-Physics-Astronomy*, **326**(12), 867-872 (1998).

[68] G. P. Panasenko. Introduction to Multiscale Mathematical Modeling, *World Scientific* (2022).

[69] G. P. Panasenko, K. Pileckas. Asymptotic analysis of the nonsteady viscous flow with a given flow rate in a thin pipe, *Applicable Analysis*, **91**(3), 559-574 (2012).

[70] G. P. Panasenko, K. Pileckas. Asymptotic analysis of the non–steady Navier–Stokes equations in a tube structure I. The case without boundary layer-in-time, *Nonlinear Analysis: Theory, Methods & Applications*, **122**, 125-168 (2015).

[71] G. P. Panasenko, K. Pileckas. Asymptotic analysis of the non–steady Navier–Stokes equations in a tube structure II. General case, *Nonlinear Analysis: Theory, Methods & Applications*, **125**, 582-607 (2015).

[72] J. L. Poiseuille. *Recherches experimentales sur le mouvement des liquides dans les tubes de tres–petits diametres*, Academie des Sciences, Paris (1843).

[73] J. L. M. Poiseuille. *Recherches sur les Causes du Mouvement du Sang dans les Vaisseaux Capillaires*, Impr. Royale (1839).

[74] K. Pileckas, V. Keblikas. Existence of nonstationary Poiseuille solution, *Siberian Mathematical Journal*, **46**(3), 514-526 (2005).

[75] K. Pileckas. On the behavior of the nonstationary Poiseuille solution as $t \to \infty$, *Siberian Mathematical Journal*, **46**, 707-716 (2005).

[76] K. Pileckas. Existence of solutions with the prescribed flux of the Navier–Stokes system in an infinite cylinder, *Journal of Mathematical Fluid Mechanics*, **8**(4), 542-563 (2006).

[77] K. Pileckas. Chapter 8 - The Navier–Stokes system in domains with cylindrical outlets to infinity. Leray's problem, *Handbook of Mathematical Fluid Dynamics*, **4**, 445-647 (2007).

[78] K. Pileckas. Solvability in weighted spaces of the three–dimensional Navier–Stokes problem in domains with cylindrical outlets to infinity, *Topological Methods in Nonlinear Analysis*, **29**(2), 333-360 (2007).

[79] K. Pileckas. Global solvability in $W_2^{2,1}$-weighted spaces of the two–dimensional Navier–Stokes problem in domains with strip–like outlets to infinity, *Journal of Mathematical Fluid Mechanics*, **10**(2), 272-309 (2008).

[80] K. Pileckas, R. Čiegis. Existence of nonstationary Poiseuille–type solutions under minimal regularity assumptions, *Zeitschrift für angewandte Mathematik und Physik*, **71**, 192 (2020).

[81] E. A. Pogorelova, A. I. Lobanov. Influence of enzymatic reactions on blood coagulation autowave, *Biophysics*, **59**(1), 110–118 (2014).

[82] N. Roussel, M. Geiker, F. Dufour, L. Thrane P. Szabo. Computational modeling of concrete flow: General Overview, *Cement and Concrete Research*, **37**, 1298-1307 (2007).

[83] A. Şamandar, M. V. Gokçe. Study of workability of fresh concrete using high range water reducer admixtures, *International Journal of the Physical Sciences*, **7**, 1097-1104 (2012).

[84] W.W. Schmaedeke. Approximate solutions for the Volterra equations of the first kind, *Journal of Mathematical Analysis and Applications*, **23**(3), 604-613 (1968).

[85] J. M. Smit, J. Simon, M. El Mahdiui, L. Szaraz, P. J. van Rosendael, M. Kolassváry, B. Szilveszter, V. Delgado, B. Merkely, P. Maurovich-Horvat, J. J. Bax. Anatomical Characteristics of the Left Atrium and Left Atrial Appendage in Relation to the Risk of Stroke in Patients With Versus Without Atrial Fibrillation, *Arrhythmia and Electrophysiology*, **14**, e009777 (2021).

[86] S.S. Sritharan. On the acceleration of viscous fluid through an unbounded channel, *Journal of Mathematical Analysis and Applications*, **168**(1), 255-283 (1992).

[87] V. Šumskas. *Finite Volume ADI Schemes for Hybrid Dimension Heat Conduction Models*, Doctoral Dissertation, Vilnius University (2022).

[88] A. Tokarev , I. Sirakov , G. Panasenko , V. Volpert , E. Shnol , A. Butylin, F. Ataullakhanov. Continuous mathematical model of platelet thrombus formation in blood flow, *Russian Journal of Numerical Analysis and Mathematical Modelling* **27**(2), 191–212 (2012).

[89] A. A. Tokarev, Yu. V. Krasotkina, M. V. Ovanesov, M. A. Panteleev, M. A. Azhigirova, V. A. Volpert, F. I. Ataullakhanov, A. A. Butilin. Spatial dynamics of contact-activated fibrin clot formation in vitro and in silico in haemophilia B: effects of severity and Ahemphil B treatment, *Mathematical Modelling of Natural Phenomena*, **1**(2), 124–137 (2006).

[90] A. Tokarev, G. Panasenko, F. Ataullakhanov. Segregation of flowing blood: mathematical description, *Mathematical Modelling of Natural Phenomena*, **6**(5), 281-319 (2011).

[91] A. Tokarev, I. Sirakov, G. Panasenko, V. Volpert, E. Shnol, A. Butylin, F. Ataullakhanov. Continuous mathematical model of platelet thrombus formation in blood flow, *Russian Journal of Numerical Analysis and Mathematical Modelling*, **27**(2), 192-212 (2012).

[92] A. Tosenberger, F. Ataullakhanov, N. Bessonov, M. Panteleev, A. Tokarev, V. Volpert. Modelling of thrombus growth inow with a DPD-PDE method, *Journal of Theoretical Biology*, **337**, 30–41 (2013).

[93] A. Tosenberger, F. Ataullakhanov, N. Bessonov, M. Panteleev, A. Tokarev, V. Volpert. Modelling of platelet–fibrin clot formation in flow with a DPD-PDE method, *Journal of Mathematical Biology*, **72**(3), 649-681 (2016).

[94] F. G. Tricomi. Integral Equations, *Intersience*, New York (1957).

[95] S. Valvez, M. Oliveira-Santos, A. P. Pledade, L. Goncalves, A. M. Amaro. Computational flow dynamic analysis in left atrium appendage thrombus formation risk: a review, *Applied Sciences MDPI*, **13**, 8201 (2023).

[96] J. P. Veinot, P. J. Harrity, F. Gentile, B. K. Khandheria, K. R. Bailey, J. T. Eickholt, J. B. Seward, A. J. Tajik, W. D. Edwards. Anatomy of the normal left atrial appendage: a quantitative study of age-related changes in 500 autopsy hearts: implications for echocardiographic examination, *Circulation*, **96**, 3112–3115 (1997).

[97] D. Vella, A. Monteleone, G. Musotto, G. M. Bosi, G. Burriesci. Effect of the alternations in contractility and morphology produced by atrial fibrillation on the thrombosis potential of the left atrial appendage, *Frontiers in Bioengineering and Biotechnology*, **9**, 586041 (2021).

[98] S. S. Virani *et al.* Heart disease and stroke statistics-2021 update: A report from the American Heart Association, *Circulation*, **143**(10), e56-e528 (2021).

[99] J. R. Womersley. Method for the calculation of velocity, rate of flow and viscous drag in arteries when the pressure gradient is known, *The Journal of Physiology*, **127**(3), 553-563 (1955).

[100] Z. Xu, N. Chen, M. M. Kamocka, E. D. Rosen, M. Alber. A multiscale model of thrombus development, *Journal of the Royal Society Interface*, **5**(24), 705-722 (2008).

[101] S. Yaghi, A. D. Chang, R. Akiki, S. Collins, T. Novack, M. Hemendinger, A. Schomer, B. Mac Grory, S. Cutting, T. Burton, C. Song, A. Poppas, R. McTaggart, M. Jayaraman, A. Merkler, H. Kamel,

M. S. V. Elkind, K. Furie, M. K. Atalay. The left atrial appendage morphology is associated with embolic stroke subtypes using a simple classification system: A proof of concept study, *Journal of Cardiovascular Computed Tomography*, **14**(1), 27-33 (2020).

[102] A. Yazdani, H. Li, J. D. Humphrey, G. E. Karniadakis. A General Shear-Dependent Model for Thrombus Formation, *PLoS Computational Biology*, **13**(1), e1005291 (2017).

Summary (Santrauka)

Navjė ir Stokso lygčių sistema (pavadinta K. Navjė ir G. Stokso vardais), aprašanti klampaus nespūdaus skysčio tekėjimą, užrašoma taip:

$$\begin{cases} \rho \mathbf{u}_t - \mu \Delta \mathbf{u} + \rho(\mathbf{u}\cdot\nabla)\mathbf{u} + \nabla \tilde{p} &= \rho \mathbf{f}, \\ \text{div } \mathbf{u} &= 0, \end{cases}$$

čia $\mathbf{u} = \mathbf{u}(x,t) = (u_1(x,t), \ldots, u_n(x,t))$ ir $\tilde{p} = \tilde{p}(x,t)$ – atitinkamai skysčio greičio vektorius ir slėgis, $\mathbf{f} = \mathbf{f}(x,t) = (f_1(x,t), \ldots, f_n(x,t))$ – skystį veikiančios išorinės jėgos vektorius, $x = (x_1, ..., x_n)$ – erdvės kintamieji, t – laikas, ρ – skysčio tankis, μ – dinaminė skysčio klampa.

Laikydami, kad $p = \frac{\tilde{p}}{\rho}$, laiko atžvilgiu periodinį Navjė ir Stokso uždavinį srityje Ω užrašykime tokiu būdu:

$$\begin{cases} \mathbf{u}_t - \nu \Delta \mathbf{u} + (\mathbf{u}\cdot\nabla)\mathbf{u} + \nabla p &= \mathbf{f}, \\ \text{div } \mathbf{u} &= 0, \\ \mathbf{u}|_{\partial\Omega} &= 0, \\ \mathbf{u}(x,0) &= \mathbf{u}(x,T), \quad 0 < T < \infty, \end{cases}$$

čia $\nu = \frac{\mu}{\rho}$ – kinematinė skysčio klampa.

Niutoninio skysčio tekėjimas, aprašomas Navjė ir Stokso lygtimis begaliniame cilindre su pastoviu skerspjūviu, yra vienas iš pagrindinių ir labiausiai nagrinėjamų hidrodinamikos uždavinių. Vienas iš svarbiausių yra vadinamasis Puazeilio tekėjimas. Kaip žinoma, šis tekėjimas apibūdinamas greičio vektoriaus lauku, turinčiu tik vieną nenulinę komponentę, nukreiptą išilgai vamzdžio ašies ir priklausančią tik nuo skerspjūvio taškų koordinačių ir dažnai nuo laiko. Atitinkamas slėgis yra aprašomas (nenuliniu) ašiniu gradientu dar vadinamu slėgio nuolydžiu, kuris priklauso tik nuo laiko. Puazeilio tekėjimą galima aprašyti dviem būdais: arba nurodant slėgio nuolydį, arba srautą. Antruoju atveju dažnai neturima duomenų apibrėžtų glodžiosiomis

funkcijomis, todėl svarbu išnagrinėti nestacionarųjį Puazeilio tipo sprendinį turint minimalų duomenų reguliarumą. Šioje disertacijoje mes įrodome periodinio laiko atžvilgiu Navjė ir Stokso uždavinio sprendinio egzistavimą ir vienatį esant minimaliai reguliariam srautui.

Be to, hemodinamikoje skysčio tekėjimo sritis (pvz. arterijos *lumenas*) būna apsupta elastinga sienele (pvz. arterijos *tunica*). Tuomet nagrinėjamas FSI (*angl.* Fluid Structure Interaction) uždavinys (žr. pvz. [54]), kai skystis sąveikauja su sienele. Šioje disertacijoje iš FSI modelio [66] pasiūlyto G. Panasenko ir R. Stavre išvedama ketvirtosios eilės supaprastinta diferencialinė lygtis dalinėmis išvestinėmis priklausanti tik nuo laiko ir vieno erdvės kintamojo ir aprašanti skysčio tekėjimą cilindre su elastinga sienele. Toliau atliekamas palyginimas tarp apskaičiuotų iš išvestos lygties ir pilnojo Navjė ir Stokso (su FSI) modelio vidutinių greičių dviejose geometrijose: vamzdyje ir Y-formos cilindrų tinkle.

Galiausiai, panaudojus pilnąjį FSI modelį su Navjė ir Stokso lygčių sistema apskaičiuojamas kraujo tekėjimo greitis žmogaus širdies kairiojo prieširdžio apendikse. Manoma, kad mažesnis kraujo tekėjimo greitis šioje srityje skatina trombų susidarymą (žr. [47]). Taigi, šioje disertacijoje sukuriamas modelis, leidžiantis apskaičiuoti konkretaus paciento kraujo tekėjimo greitį bet kuriame kairiojo prieširdžio apendikso taške, tokiu būtu aptinkant stagnacijos zonas.

Tyrimo objektas

Šioje disertacijoje nagrinėjami trys uždaviniai: įrodomi laiko atžvilgiu periodinio Puazeilio tipo Navjė ir Stokso lygčių sistemos sprendinio su minimalaus reguliarumo srautu egzistavimas ir vienatis, atliekama Puazeilio tipo sprendinio aproksimacija tekant skysčiui vamzdyje su elastinga sienele, bei sukonstruojamas modelis, leidžiantis apskaičiuoti kraujo tekėjimo greitį žmogaus širdies kairiojo prieširdžio apendikse.

Mokslinės problemos istorija ir aktualumas

Kaip minėta, Puazeilio tekėjimą galima aprašyti dviem būdais: arba nurodant slėgio nuolydį, arba srautą. Antruoju atveju, kai yra užduodamas

skysčio srautas, uždavinys gali būti interpretuojamas kaip atvirkštinis uždavinys. Pavyzdžiui, 2005 metais G. P. Galdi ir A. M. Robertson nagrinėjo periodinį laiko atžvilgiu Navjė ir Stokso skysčio tekėjimą uždaro begalinio cilindro skerspjūvyje ir įrodė sprendinio egzistavimą ir vienatį (žr. [29]). Čia srautas buvo apibrėžtas sąlyga $F(t) \in W^{1,2}(0;2\pi)$. Tačiau, žinoma, kad Navjė ir Stokso lygčių sistemos taikymuose srautas ne visada apibrėžiamas glodžiosiomis funkcijomis, todėl K. Pileckas ir R. Čiegis 2020 metais įrodė Puazeilio tipo sprendinio egzistavimą ir vienatį, kai srautas priklauso tik $L^2(0,T)$ (žr. [80]). Šioje disertacijoje pastarasis rezultatas praplečiamas, t.y. mes įrodome Puazeilio tipo sprendinio egzistavimą ir vienatį periodiniu laiko atžvilgiu atveju toje pačioje funkcijų klasėje, kaip nagrinėta [80]. Nauja tendencija sprendžiant tokius uždavinius yra susijusi su hibridinių matmenų modelių kūrimu, derinant vienmačius modelius įprastose srities vietose (pavyzdžiui, tiesiose kraujagyslėse) su trimačiais priartinimais išskirtinio elgesio srities zonose (pavyzdžiui, kraujagyslių išsišakojimuose, krešulių susidarymo vietose). Vienmačiams uždaviniams yra svarbūs Puazeilio sprendiniai, o trimačiai uždaviniai modeliuojami Navjė ir Stokso lygtimis. Šis skirtingų matmenų derinimo metodas leidžia gauti griežtai pagrįstus iš dalies supaprastintus modelius, išlaikant labai aukštą aproksimacijos tikslumą. Be to, tokiems hibridinių matmenų modeliams reikalingi reikšmingai mažesni skaičiavimo ištekliai.

Šiuolaikiniame pasaulyje matematinis modeliavimas vis daugiau naudojamas fiziologijoje ir medicinoje, padėdamas pasirinkti optimalią gydymo strategiją. Svarbi matematinio modeliavimo dalis susijusi su sąveikos tarp skysčio ir standžios struktūros, dar vadinamo FSI. Šioje disertacijoje nagrinėjamas 2019-2020 metais pasiūlytas G. Panasenko ir R. Stavre modelis [65] ir [66], ir iš jo išvedama ketvirtosios eilės diferencialinė lygtis dalinėmis išvestinėmis aprašanti skysčio tekėjimą vamzdžiu su elastinga sienele. Pastarosios lygties skaitiniam sprendimui sudaroma neišreikštinė baigtinių skirtumų schema (panaudota V. Šumsko disertacijoje [87]). Tuomet atliekamas gauto sprendinio palyginimas su pilnu Navjė ir Stokso lygčių sistemos modeliu dviejose geometrijose: cilindre ir trijų cilindrų Y-formos tinkle su judančia sienele. Svarbu, kad išvestajai ketvirtosios eilės diferencialinei lygčiai dalinėmis išvestinėmis reikalingi žymiai mažesni skaičiavimo resursai, nei

pilnajam Navjė ir Stokso medeliui.

Sąveikos tarp skysčio ir standžios struktūros uždavinius galima spręsti sudėtingesnėse, nei cilindras arba jų tinklas, geometrijose. Šioje disertacijoje nagrinėjamas skysčio (mūsų atveju kraujo) tekėjimas žmogaus širdies kairiajame prieširdyje. Santariškių klinikų medikai teigia, kad esant prieširdžių virpėjimui, mažesnis kraujo tekėjimo greitis kairiojo prieširdžio apendikse didina trombo susidarymo jame tikimybę (tai patvirtina daug šaltinių, pvz. [47]). Be to, M. García-Villalba *ir kt.* tvirtina, kad stagnacijos zonų nustatymui kairiojo prieširdžio apendikse gali būti skaičiuojama kraujo tekėjimo kinetinė energija (žr. [34]), kuri, kaip žinia, priklauso nuo skysčio tekėjimo greičio kvadrato. Be to, [12], [42], [51], [95], [97] kraujo tekėjimo kairiajame prieširdyje skaičiavimai atliekami esant kietajai (nejudančiai) sienelei. D. Vella *ir kt.* modelyje kairiojo prieširdžio geometrija supaprastina (žr. [97]), [12] skaičiavimai stabilizuojasi tik po 10 širdies ciklų, o [34] - netgi po 20. Šioje disertacijoje sukurtas modelis įtraukia Navjė ir Stokso lygčių sistemos bei kevalo (*angl.* Shell) teorijos lygčių taikymą hemodinamikos modeliavime, o sienelė juda, kas labiau atitinka tikrovę bei skaičiavimai stabilizuojasi po 3 širdies ciklų. Gaunamas dviejų pacientų kraujo tekėjimo greitis jų kairojo prieširdžio apendikse esant prieširdžių virpėjimui. Pasirodo, kad paciento, kurį ištiko insultas, kraujo tekėjimo greitis kairiojo prieširdžio apendikse buvo mažesnis, negu kito paciento, kurio insultas neištiko.

Disertacijos tikslai

Šioje disertacijoje nagrinėjami keli reikalingi hemodinamikos taikymuose uždaviniai, ir kiekvienam iš jų keliami skirtingi tikslai:

I. Įrodyti laiko atžvilgiu periodinio Navjė ir Stokso uždavinio sprendinio egzistavimą ir vienatį begaliniame cilindre, kai užduotas srautas $F(t) \in L^2(0,T)$ esant minimaliam duomenų reguliarumui.

II. Supaprastinti sąveikos tarp skysčio ir standžios struktūros (FSI) modelį iki ketvirtosios eilės diferencialinės lygties dalinėmis išvestinėmis. Apskaičiuoti kraujo tekėjimo greitį cilindre ir Y-formos cilindrų tinkle dviem būdais: taikant FSI modelį sudarytą iš skaitinio Navjė ir Stokso uždavinio sprendimo su elastinga sienele ir taikant išvestą ketvirtosios eilės diferencialinę lygtį dalinėmis išvestinėmis;

palyginti gautus rezultatus tarpusavyje.

III. Trečioji tikslų dalis susijusi su modeliu, skirtu kraujo tekėjimo greičiui žmogaus širdies kairiajame prieširdyje, apskaičiuoti:
   a) Darbas su grafika, skaičiavimo srities konstravimas ir kraštinių sąlygų formulavimas.
   b) Kraujo tekėjimo kairiajame prieširdyje modelio sudarymas.
   c) Kraujo tekėjimo greičio apskaičiavimas kairiojo prieširdžio apendikse.

Disertacijos struktūra ir apimtis

Disertacija prasideda nuo įvado (1 skyrius) ir pagrindinių žymėjimų (2 skyrius).

Trečiajame skyriuje nagrinėjamas periodinis laiko atžvilgiu Puazeilio tipo Navjė ir Stokso lygčių sprendinys su minimalaus reguliarumo srautu, įrodomas sprendinio egzistavimas ir vienatis.

Ketvirtajame skyriuje atliekama Puazeilio tipo sprendinio aproksimacija tekant skysčiui vamzdyje su elastinga sienele.

Penktajame skyriuje taikydami Navjė ir Stokso lygčių ir kevalo sąveikos modelį mes patikriname šią medikų hipotezę: mažas kraujo tekėjimo greitis kairiojo prieširdžio apendikse didina trombo susidarymo tikimybę.

Paskutiniai skyriai – tai išvados, literatūros sąrašas ir santrauka.

Disertacijoje gautų rezultatų apžvalga

Laiko atžvilgiu periodinis Puazeilio tipo sprendinys su minimalaus reguliarumo srautu

Puazeilio srautas begaliniame tiesiajame cilindre $\Pi = \{x = (x', x_n) \in \mathbb{R}^n : x' \in \sigma \subset \mathbb{R}^{n-1}, -\infty < x_n < \infty, n = 2, 3\}$ su pastoviu skerspjūviu σ buvo atrastas J. L. Puazeilio 1841 metais (žr. [72], [8], [46]). Puazeilio srautas aprašomas skysčio greičio lauku, turinčiu tik vieną nelygią nuliui komponentę $U(x')$, kurios kryptis sutampa su cilindro Π ašimi x_n, o slėgis $p = p(x_n)$ yra tiesinis. Mes nagrinėjame periodinį laiko atžvilgiu Navjė ir Stokso uždavinį, aprašantį klampaus nespūdaus skysčio tekėjimą aukščiau aprašytame

cilindre Π:

$$\begin{cases} \mathbf{u}_t - \nu\Delta\mathbf{u} + (\mathbf{u}\cdot\nabla)\mathbf{u} + \nabla p &= 0, \quad (x,t) \in \Pi \times (0,2\pi), \\ \text{div } \mathbf{u} &= 0, \quad (x,t) \in \Pi \times (0,2\pi), \\ \mathbf{u}|_{\partial\Pi\times(0,2\pi)} &= 0, \\ \mathbf{u}(x,0) &= \mathbf{u}(x,2\pi), \end{cases} \tag{S.1}$$

čia $\mathbf{u}$ yra skysčio greitis, p – slėgį aprašanti funkcija ir $\nu > 0$ pastovi skysčio kinematinė klampa.

Ieškosime (S.1) sprendinio $\mathbf{u}$ tenkinančio papildomą užduoto srauto $F(t)$ sąlygą:

$$\int_\sigma u_n(x,t)\,\mathrm{d}x' = F(t),$$

čia $F(0) = F(2\pi)$. Nemažindami bendrumo, galime laikyti, kad periodas lygus 2π.

Uždavinio (S.1) sprendinys $\big(\mathbf{u}(x,t), p(x,t)\big)$ užrašomas pavidalu

$$\mathbf{u}(x,t) = (0,\ldots,0,U_n(x',t)), \qquad p(x,t) = -q(t)x_n + p_0(t), \tag{S.2}$$

čia $p_0(t)$ – laisvai pasirenkama funkcija. Įrašę (S.2) į (S.1) gausime tokį uždavinį skerspjūvyje σ:

$$\begin{gathered} U_t(x',t) - \nu\Delta' U(x',t) = q(t), \\ U(x',t)\big|_{\partial\sigma} = 0, \quad U(x',0) = U(x',2\pi), \end{gathered} \tag{S.3}$$

čia $U(x',t) = U_n(x',t)$ ir $q(t)$ yra nežinomos funkcijos, Δ' yra Laplaso operatorius pagal x'. Netiesinio nario nelieka dėl Puazeilio srauto (žr. S.2).

Kaip žinia, Puazeilio srautas gali būti apibrėžtas vieninteliu būdu užduodant slėgio gradientą $q(t)$ arba srautą $F(t)$. Pirmu atveju uždavinys supaprastinamas iki standartinės periodinės laiko atžvilgiu šilumos laidumo lygties su nežinomu greičiu $U = U(x',t)$ ir laiko atžvilgiu periodiniu $q(t)$. Šio tipo uždaviniai plačiai išnagrinėti [44]. Tačiau, praktiniuose taikymuose slėgis nežinomas, o turime tik skysčio tekėjimo srautą. Tokiu atveju, turime nagrinėti Puazeilio srautą su užduotu $F(t)$:

$$\int_\sigma U(x',t)\,\mathrm{d}x' = F(t), \quad F(0) = F(2\pi). \tag{S.4}$$

Tuomet uždavinio (S.3), (S.4) sprendinys – tai funkcijų $(U(x',t), q(t))$ pora, kuriai galime suformuluoti sudėtingesnį *atvirkštinį* parabolinį uždavinį:

duotajam $F(t)$ *apskaičiuoti funkcijų* $(U(x',t),q(t))$ *porą išsprendus* (S.3) *su* $U(x',t)$ *tenkinančiu srauto sąlygą* (S.4).

Taigi, antru atveju sąryšis tarp $q(t)$ ir $F(t)$ priklauso nuo atvirkštinio uždavinio sprendinio (stacionariuoju atveju srautas F ir slėgio gradientas q proporcingi, taigi uždavinys yra trivialus). Periodinio laiko atžvilgiu uždavinio sprendinio egzistavimas ir vienatis su prielaida, kad srautas $F(t)$ yra iš Sobolevo erdvės $W^{1,2}(0,2\pi)$ buvo įrodytas H. Beirão da Veiga [9], be to, G. P. Galdi ir A. M. Robertson rado sąryšį tarp $q(t)$ ir $F(t)$ (žr. [29]). Tačiau, taikymuose ir skaitiniuose skaičiavimuose dažniausiai duomenys nereguliarūs. Todėl, norėdami pagerinti [9] ir [29] rezultatą šioje disertacijoje mes nagrinėjame uždavinį (S.3), (S.4) laikydami **tik**, kad $F \in L^2(0,2\pi)$, t.y. glodumas nežinomas.

Uždavinys (S.3), (S.4) gali būti supaprastintas iki atvejo, kai visos reikalingos funkcijos turi vidurkius lygius nuliui. Toliau žymėsime funkcijos H vidurkį tokiu būdu: $\bar{H} = \frac{1}{2\pi}\int_0^{2\pi} H(t)\mathrm{d}t$. Tegul $(\bar{U},\bar{q})$ yra uždavinio

$$\begin{cases} -\nu\Delta'\bar{U}(x') &= \bar{q}, \\ \bar{U}(x')|_{\partial\sigma} &= 0, \\ \displaystyle\int_\sigma \bar{U}(x')\mathrm{d}x' &= \bar{F}. \end{cases}$$

sprendinys skerspjūvyje σ (stacionarusis Puazeilio sprendinys atitinka srautą $\bar{F}$). $\bar{U}(x')$ gali būti užrašytas pavidalu $\bar{U}(x') = \dfrac{\bar{F}}{\kappa_0}U_0(x')$, čia

$$\begin{cases} -\nu\Delta' U_0(x') &= 1, \\ U_0(x')|_{\partial\sigma} &= 0, \end{cases}$$

ir

$$\bar{q} = \frac{\bar{F}}{\kappa_0}, \quad \kappa_0 = \int_\sigma U_0(x')\mathrm{d}x' = \nu\int_\sigma |\nabla' U_0(x')|^2\mathrm{d}x' > 0.$$

Ieškome sprendinio (U,q) pavidalu

$$U(x',t) = V(x',t) + \bar{U}(x'), \quad q(t) = s(t) + \bar{q}.$$

Tuomet akivaizdu, kad $\bar{V}(x') = 0$, $\bar{s} = 0$ ir (V,s) yra uždavinio

$$\begin{cases} V_t(x',t) - \nu\Delta' V(x',t) &= s(t), \\ V(x',t)|_{\partial\sigma} &= 0, \\ V(x',0) &= V(x',2\pi), \\ \displaystyle\int_\sigma V(x',t)\mathrm{d}x' &= \widetilde{F}(t), \end{cases} \tag{S.5}$$

sprendinys, čia $\widetilde{F}(t) = F(t) - \bar{F}$. Vadinasi, $\bar{\widetilde{F}} = 0$, be to, laikysime benduoju atveju, kad $\bar{F} = 0$.

Silpnojo sprendinio apibrėžimas. *Tegul* $F \in L^2_\sharp(0,2\pi)$. *Uždavinio* (S.5) *silpnuoju sprendiniu laikysime porą* (V,s) *tokią, kad* $V \in L^2_\sharp(0,2\pi;L^2(\sigma))$, $s \in W^{-1,2}_\wp(0,2\pi)$. $V(x',t)$ *tenkina srauto sąlygą*

$$\int_\sigma V(x',t)\mathrm{d}x' = F(t)$$

ir pora (V,s) tenkina integralinę tapatybę

$$\begin{aligned}\int_0^{2\pi}\int_\sigma V(x',t)\eta_t(x',t)\mathrm{d}x'\mathrm{d}t + \nu\int_0^{2\pi}\int_\sigma \nabla' S_V(x',t)\cdot\nabla'\eta_t(x',t)\mathrm{d}x'\mathrm{d}t \\ = \int_0^{2\pi} S_s(t)\int_\sigma \eta_t(x',t)\mathrm{d}x'\mathrm{d}t\end{aligned} \tag{S.6}$$

su bet kuria testine funkcija $\eta \in L^2_\wp(0,2\pi;\mathring{W}^{1,2}(\sigma))$ tokią, kad $\eta_t \in L^2_\sharp(0,2\pi;W^{1,2}(\sigma))$.

Pastaba. Čia norėdami pabrėžti, kad funkcijos periodiškai pratęstos $\mathbb{R}^1$ naudojame žymėjimą $L^2_\wp(0,2\pi)$.

Tegul $L^2_\sharp(0,2\pi) = \{h \in L^2_\wp(0,2\pi) : \int_0^{2\pi} h(t)\mathrm{d}t = 0\}$. Žinoma, $L^2_\sharp(0,2\pi)$ yra $C^\infty_\sharp(0,2\pi) = \{h \in C^\infty_\wp(0,2\pi) : \int_0^{2\pi} h(t)\mathrm{d}t = 0\}$ uždarinys $L^2(0,2\pi)$ normoje ir yra $L^2_\wp(0,2\pi)$ poerdvis. $W^{1,2}_\wp(0,2\pi)$ yra aibės $C^\infty_\wp(0,2\pi)$ uždarinys $W^{1,2}(0,2\pi)$ normoje. $W^{-1,2}_\wp(0,2\pi)$ yra jungtinė $W^{1,2}_\wp(0,2\pi)$, t.y., $W^{-1,2}_\wp(0,2\pi) = \left(W^{1,2}_\wp(0,2\pi)\right)^*$.

$\forall$ funkcijai $f \in L^2_\wp(0,2\pi)$ žymime $S_f(t)$ jos pirmykštę:

$$S_f(t) = -\int_t^{t_0+2\pi} f(\tau)\mathrm{d}\tau, \quad \text{čia } t_0 \in [0,2\pi), t \in [t_0, t_0+2\pi].$$

Reguliariajam sprendiniui (V,s) laikant, kad $\nabla V = (\nabla S_V)_t$, $s = S'_s$, tapatybė (S.6) gaunama dauginant lygtį $(\mathrm{S.5})_1$ iš η, integruojant srityje σ intervale $(0,2\pi)$, o paskui integruojant dalimis pagal x' ir pagal t. Iš kitos pusės, kadangi silpnasis sprendinys vienintelis (V,s) (žr. Teoremą*), išplaukia, kad srautui $F \in W^{1,2}_\sharp(0,2\pi)$ sprendinys (V,s) sutampa su reguliariuoju, t.y. $V \in L^2_\sharp(0,2\pi;\mathring{W}^{1,2}(\sigma)\cap W^{2,2}(\sigma))$, $V_t \in L^2_\sharp(0,2\pi;L^2(\sigma))$, $s \in L^2_\sharp(0,2\pi)$. Todėl siūlomas apibrėžimas yra silpnųjų sprendinių koncepcijos pratęsimas.

Teorema***.** *Tegul* $F \in L^2_\sharp(0,2\pi)$. *Tuomet uždavinys* (S.5) *turės vienintelį silpnąjį sprendinį* (V,s). *Be to, galioja įvertis*

$$\int_0^{2\pi}\int_\sigma |V(x',t)|^2 \mathrm{d}x'\mathrm{d}t + \int_0^{2\pi}\int_\sigma \left|\nabla' S_V(x',t)\right|^2 \mathrm{d}x'\mathrm{d}t + \int_0^{2\pi} |S_s(\tau)|^2 \mathrm{d}\tau \leqslant c\int_0^{2\pi} |F(\tau)|^2 \mathrm{d}\tau,$$

čia konstanta c priklauso tik nuo σ.

Puazeilio tipo srauto aproksimacija ploname cilindre padengtame patvaria elastinga sienele

Šiame skyrelyje nagrinėjamas FSI uždavinys cilindre ir Y-formos cilindrų tinkle su elastinga sienele. Imamas modelis (S.7) pasiūlytas G. Panasenko ir R. Stavre (žr. [65], [66]) ir iš jo išvedama ketvirtosios eilės supaprastinta diferencialinė lygtis dalinėmis išvestinėmis, kuri priklauso tik nuo vieno erdvės kintamojo ir laiko.

$$\begin{cases}
\omega_\rho \rho_e \dfrac{\partial^2 \mathbf{u}}{\partial t^2} - \omega_E L\mathbf{u} = \varepsilon^{-1}\mathbf{g} & \text{iš } L^e_\varepsilon \times (0,T), \\
\begin{cases} \rho_f \dfrac{\partial \mathbf{v}}{\partial t} - 2\nu \mathrm{div}_c D_c(\mathbf{v}) + \nabla p = \mathbf{f} \\ \mathrm{div}_c \mathbf{v} = 0 \end{cases} & \text{iš } L^f \times (0,T), \\
v_r = 0 & \text{iš } F^0 \times (0,T), \\
\begin{cases} \dfrac{\partial u_3}{\partial r} + \dfrac{\partial u_r}{\partial x_3} = 0 \\ \lambda(1)\dfrac{\partial u_3}{\partial x_3} + (\lambda(1)+2\mu(1))\dfrac{\partial u_r}{\partial r} \\ \quad + \dfrac{\lambda(1)}{\varepsilon_1+\varepsilon} u_r = 0 \end{cases} & \text{iš } F^{\varepsilon_1+\varepsilon} \times (0,T), \\
\begin{cases} \mathbf{v} = \dfrac{\partial \mathbf{u}}{\partial t} \\ \nu\left(\dfrac{\partial v_3}{\partial r} + \dfrac{\partial v_r}{\partial x_3}\right) = \omega_E \mu(0)\left(\dfrac{\partial u_3}{\partial r} + \dfrac{\partial u_r}{\partial x_3}\right) \\ -p + 2\nu \dfrac{\partial v_r}{\partial r} = \omega_E\Big(\lambda(0)\dfrac{\partial u_3}{\partial x_3} + (\lambda(0) \\ \quad + 2\mu(0))\dfrac{\partial u_r}{\partial r} + \dfrac{\lambda(0)}{\varepsilon_1} u_r\Big) \end{cases} & \text{iš } F^{\varepsilon_1} \times (0,T), \\
\mathbf{u}, \mathbf{v}, p & 1-\text{periodinės } x_3, \\
\mathbf{u}(0) = \dfrac{\partial \mathbf{u}}{\partial t}(0) = \mathbf{0} & \text{iš } L^e_\varepsilon, \\
\mathbf{v}(0) = \mathbf{0} & \text{iš } L^f,
\end{cases} \tag{S.7}$$

čia ρ_e yra sienelės tankis, ω_ρ yra jo eilė, ω_E - Jungo modulio eilė, ρ_f - skysčio tankis, ν - jo dinaminės klampos koeficientas ε - sienelės storis, ε_1 - vamzdžio neįskaitant sienelės spindulys, $\mathbf{u}$ - sienelės poslinkis, $\mathbf{v}$ - skysčio greitis, p - slėgis, $\mathbf{g}$ ir $\mathbf{f}$ - išorinės jėgos veikiančios atitinkamai sienelę ir skystį, λ ir μ - Lamė parametrai. Taip pat (S.7) modelyje naudojami šie žymejimai:

— tiesinis elastingumo operatorius

$$L\mathbf{u}\cdot\mathbf{e}_3 = \frac{\partial}{\partial x_3}\left((\lambda+2\mu)\frac{\partial u_3}{\partial x_3}+\lambda\left(\frac{\partial u_r}{\partial r}+\frac{1}{r}u_r\right)\right) + \frac{\partial}{\partial r}\left(\mu\left(\frac{\partial u_3}{\partial r}+\frac{\partial u_r}{\partial x_3}\right)\right)+\frac{\mu}{r}\left(\frac{\partial u_3}{\partial r}+\frac{\partial u_r}{\partial x_3}\right),$$

$$L\mathbf{u}\cdot\mathbf{e}_r = \frac{\partial}{\partial x_3}\left(\mu\left(\frac{\partial u_3}{\partial r}+\frac{\partial u_r}{\partial x_3}\right)\right)+\frac{\partial}{\partial r}\left(\lambda\left(\frac{\partial u_3}{\partial x_3}+\frac{1}{r}u_r\right) +(\lambda+2\mu)\frac{\partial u_r}{\partial r}\right)+\frac{2\mu}{r}\left(\frac{\partial u_r}{\partial r}-\frac{1}{r}u_r\right),$$

— divergencijos operatorius atitinkamai vektorinei ir tenzorinei funkcijoms

$$\mathrm{div}_c\mathbf{u} = \frac{\partial u_3}{\partial x_3}+\frac{\partial u_r}{\partial r}+\frac{1}{r}u_r,$$

$$\mathrm{div}_c S = \left(\frac{\partial S_{33}}{\partial x_3}+\frac{1}{r}\frac{\partial}{\partial r}(rS_{r3})\right)\mathbf{e}_3 + \left(\frac{\partial S_{3r}}{\partial x_3}+\frac{1}{r}\frac{\partial}{\partial r}(rS_{rr})-\frac{S_{\theta\theta}}{r}\right)\mathbf{e}_r,$$

— gradiento operatorius vektorinei funkcijai

$$\nabla_c\mathbf{u} = \begin{pmatrix} \frac{\partial u_3}{\partial x_3} & 0 & \frac{\partial u_3}{\partial r} \\ 0 & \frac{1}{r}u_r & 0 \\ \frac{\partial u_r}{\partial x_3} & 0 & \frac{\partial u_r}{\partial r} \end{pmatrix},$$

— deformacijos greičio tenzorius

$$D_c(\mathbf{u}) = \frac{1}{2}\left(\nabla_c\mathbf{u}+(\nabla_c\mathbf{u})^T\right).$$

Be to, (x_3, r, θ) - tai cilindrinės koordinatės, $\mathbf{e}_3$ ir $\mathbf{e}_r$ vienetiniai atitinkamai Ox_3 ir Or ašių vektoriai $\mathbf{u}$ - vektorinė funkcija, S - tenzorinė funkcija. Sritys naudojamos (S.7): $L^f = \{(x_3, r) \in \mathbb{R}^2 : x_3 \in \mathbb{R}, r \in (0, \varepsilon_1)\}$ - skysčio sritis, $L^e_\varepsilon = \{(x_3, r) \in \mathbb{R}^2 : x_3 \in \mathbb{R}, r \in (\varepsilon_1, \varepsilon_1+\varepsilon)\}$ - elastingos sienelės sritis, $F^0 = \{(x_3, 0) : x_3 \in \mathbb{R}\}$ - vamzdžio simetrijos ašis, $F^{\varepsilon_1} = \{(x_3, \varepsilon_1) : x_3 \in \mathbb{R}\}$ -

kraštas tarp skysčio ir vidinės sienelės dalies, $F^{\varepsilon_1+\varepsilon} = \{(x_3, \varepsilon_1+\varepsilon) : x_3 \in \mathbb{R}\}$ - išorinis sienelės kraštas.

Tuomet iš (S.7) išvedama ketvirtosios eilės diferencialinė lygtis dalinėmis išvestinėmis užrašoma tokiu pavidalu:

$$\begin{cases} C_1\dfrac{\partial^2 Q(x_3,t)}{\partial t^2} + C_2\dfrac{\partial^4 Q(x_3,t)}{\partial x_3^2 \partial t^2} + C_3\dfrac{\partial Q(x_3,t)}{\partial t} + C_4\dfrac{\partial^3 Q(x_3,t)}{\partial x_3^2 \partial t} \\ + C_5\dfrac{\partial^4 Q(x_3,t)}{\partial x_3^4} + C_6\dfrac{\partial^2 Q(x_3,t)}{\partial x_3^2} + C_7 Q(x_3,t) = 0, \\ Q(0,t) = g_{in}(t),\ Q(1,t) = g_{out}(t), \\ \dfrac{\partial Q(0,t)}{\partial x_3} = \dfrac{\partial Q(1,t)}{\partial x_3} = 0, \\ Q(x_3,0) = \dfrac{\partial Q(x_3,0)}{\partial t} = 0. \end{cases} \tag{S.8}$$

Norėdami atlikti palyginimą tarp lygties (S.8) ir Navjė ir Stokso modelio su elastinga sienele, į abu modelius įrašome vienodus fizikinius dydžius. Skaičiuodami skysčio vidutinį greitį Q matuojamą m/s esant Jungo moduliui $E = 10^6$ Pa, Puasono santykiui $\hat{\nu} = 0.35$, vamzdžio ilgiui 10^{-3} m, spinduliui $5 \cdot 10^{-5}$ m, elastingos sienelės storiui $\varepsilon = 2 \cdot 10^{-5}$ m ir kraujo dinaminės klampos koeficientui $\nu = 4 \cdot 10^{-3}$ Pa·s, lygčiai (S.8) gauname šias konstantas C_i:

$$C_1 = 9.2287 \cdot 10^{-38},\ C_2 = -2.0734 \cdot 10^{-42},\ C_3 = 4.1667 \cdot 10^{-2},$$
$$C_4 = -1.7904 \cdot 10^{1},\ C_5 = 7.1615 \cdot 10^{1},\ C_6 = -6.2500 \cdot 10^{-2},\ C_7 = 4.000 \cdot 10^{-4}.$$

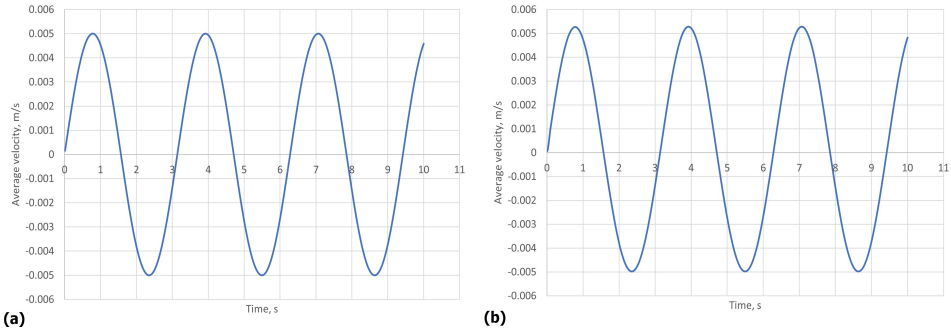

1 pav. – (a) vidutinis skysčio tekėjimo greitis gautas iš (S.8) laike, (b) vidutinis skysčio tekėjimo greitis gautas iš pilnojo Navjė ir Stokso modelio laike. Abiem atvejais, $g_{in} = 0.005\sin(2t)$, $g_{out} = 0.005\sin(2t + 0.02)$ ir sprendinys buvo paimtas iš vamzdžio skerspjūvio per vidurį.

Sprendinių palyginimui imame kelis cilindro arba Y-formos cilindrų tinklo skerspjūvius ir juose matuojame apskaičiuotą kraujo tekėjimo vidutinį greitį.

Kaip matome 1 pav., esant nedideliam skirtumui tarp „įtekėjimo“ į cilindrą ir „ištekėjimo“ iš cilindro (arba Y-formos cilindro tinklo) sąlygų, skirtumas tarp išvestos ketvirtosios eilės diferencialinės lygties dalinėmis išvestinėmis ir pilnojo Navjė ir Stokso lygčių su elastinga sienele modelių yra nereikšmingas.

Kraujo tekėjimo greičio skaičiavimas kairiajojo prieširdžio apendikse: Praktiniai taikymai

Šioje dalyje skaičiuojamas kraujo tekėjimo greitis žmogaus širdies kairiojo prieširdžio apendikse. Skaičiavimas atliekamas dviem žingsniais: pirmajame skaičiuojame kraujo greitį kairiajame prieširdyje su kieta sienele, o apskaičiuotą greitį naudojame antrajame žingsnyje, kuriame sienelė yra judanti.

Keturios plaučių venos laikomos „įtekėjimo“ sritimi, „ištekėjimo“ sritis - mitralinio vožtuvo zona, skysčio tekėjimo sritis G atitinka kairįjį prieširdį. Srities G kraštas yra trijų dalių sąjunga: kairiojo prieširdžio lateralinė sienelė Γ_1, keturi plaučių venų $\Gamma_2 = \cup_{i=1}^{4}\gamma_2^{(i)}$ skerspjūviai $\gamma_2^{(1)}, ..., \gamma_2^{(4)}$ ir mitralinio vožtuvo skerspjūvis Γ_3 (žr. 2 pav.).

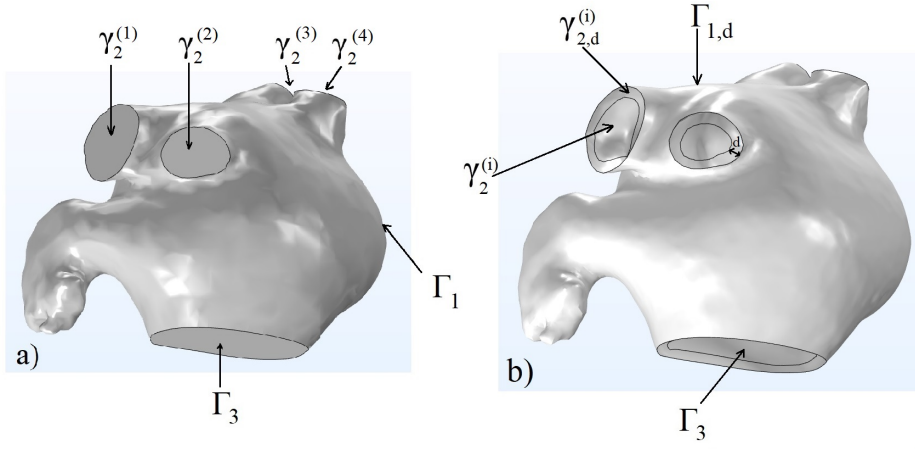

2 pav. – Keturios plaučių venos („įtekėjimo“ sritis), mitralinio vožtuvo zona („ištekėjimo“ sritis) geometrijoje: a) Skysčio tekėjimo sritis; b) Skysčio tekėjimo sritis su kevalu.

Miokardas (sienelė) - tai plonas elastingas kevalas (*angl.* Shell) G_d, d yra jo storis. Kevalas formuojamas tarp paviršių Γ_1 ir $\Gamma_{1,d}$ atstumu d nuo Γ_1 išorinės normalės kryptimi. Lateralinis sienelės kraštas $\partial G_d \backslash (\Gamma_1 \cup \Gamma_{1,d})$ statmenas Γ_1 ir sudarytas iš penkių dalių. Keturios iš jų atitinka venų sienelių skerspjūvius $\gamma_{2,d}^{(1)}, ..., \gamma_{2,d}^{(4)}$. Penkta atitinka Γ_3 ir žymima $\gamma_{3,d}$. Elastinga sienelė tarp paviršių Γ_1 ir $\Gamma_{1,d}$ juda. Skysčio tekėjimo lygtys yra nuo laiko priklausančioje srityje G^t tarp Γ_2 ir Γ_3. Sienelės poslinkio vektorius $\mathbf{u}(x,t)$, čia $x \in G_d$, taigi judanti krašto dalis $\Gamma_1^t = \{x + \mathbf{u}(x,t) \ : x \in \Gamma_1\}$.

Srityje G^t kraujo tekėjimą aprašo Navjė ir Stokso lygčių sistema

$$\begin{cases} \rho_f \mathbf{v}_t - \mu_f \Delta \mathbf{v} + \rho_f (\mathbf{v} \cdot \nabla)\mathbf{v} + \nabla p &= 0, \\ \text{div } \mathbf{v} &= 0, \end{cases} \tag{S.9}$$

čia $\mathbf{v}$ yra kraujo tekėjimo greitis, p - slėgio funkcija, $\rho_f > 0$ kraujo tankis, $\mu_f > 0$ kraujo dinaminės klampos konstanta, pradinė sąlyga

$$\mathbf{v}(x,0) = 0. \tag{S.10}$$

Toliau išvardinamos kraštinės sąlygos ant Γ_1, Γ_2 ir Γ_3.

$$\mathbf{v}(x,t)|_{\Gamma_2} = \mathbf{g}(x,t), \tag{S.11}$$

Kiekvienoje Γ_2 komponentėje $\gamma_2^{(i)}$ funkcija $\mathbf{g}$ apibrėžiama tokiu būdu:

Tegul $\tilde{x}_1, \tilde{x}_2$ - lokaliosios $\gamma_2^{(i)}$ koordinatės plokštumoje, tegul pora $(v_{P,i}(\tilde{x}_1, \tilde{x}_2, t), q(t))$ yra atvirkštinio šilumos laidumo uždavinio sprendinys srityje $\gamma_2^{(i)} \times (0, +\infty)$:

$$\rho_f \frac{\partial v_{P,i}}{\partial t}(\tilde{x}_1, \tilde{x}_2, t) - \mu_f \Delta v_{P,i}(\tilde{x}_1, \tilde{x}_2, t) = q(t),$$
$$v_{P,i}|_{\partial \gamma_2^{(i)}} = 0, \quad v_{P,i}|_{t=0} = 0,$$

$$\int\limits_{\gamma_2^{(i)}} v_{P,j}(\tilde{x}_1, \tilde{x}_2, t) \mathrm{d}\tilde{x}_1 \mathrm{d}\tilde{x}_2 = \Phi(t) \frac{\text{mes } \gamma_2^{(i)}}{\sum_{j=1}^4 \text{mes } \gamma_2^{(j)}},$$

čia $\Phi(t)$ - visas „įtekėjimo“ srautas (žr. [76], [74]).

Tangentinės $\mathbf{g}$ komponentės lygios nuliui, o normalioji komponentė $g_n(\tilde{x}_1, \tilde{x}_2, t)$ ant $\gamma_2^{(i)}$ apibrėžta tokiu būdu:

$$g_n(\tilde{x}_1, \tilde{x}_2, t) = v_{P,i}(\tilde{x}_1, \tilde{x}_2, t).$$

Ši „įtekėjimo“ greičio struktūra atitinka nestacionarų Puazeilio tekėjimą su duotu nuo laiko priklausančiu srautu begaliniame cilindre, kurio skerspjūvis $\gamma_2^{(i)}$. Taip aprašomas kraujas įtekantis į plaučių venas. Tada greičio vidurkis (srautas padalintas iš skerspjūvio ploto) yra vienodas visose keturiose plaučių venose ir lygus $F(t)$, pavaizduotas 3 pav. Čia $F(t) = \Phi(t)(\sum_{j=1}^{4} \text{mes } \gamma_2^{(j)})^{-1}$.

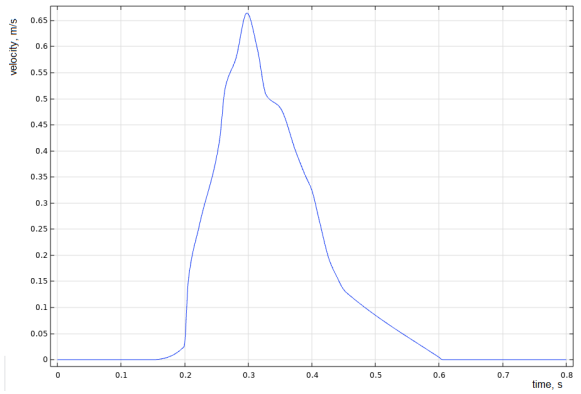

3 pav. – „Įtekėjimo“ greičio vidurkis $F(t)$ esant prieširdžių virpėjimui.

„Ištekėjimo“ srityje Γ_3 kraštinės sąlygos suformuluojamos tokiu būdu:

$$\mathbf{v}_\tau(x,t)|_{\Gamma_3} = 0, \quad p(x,t)|_{\Gamma_3} = 0. \tag{S.12}$$

Čia $\mathbf{v}_\tau$ yra tangentinis greitis ant krašto. Kraštinė sąlyga $p(x,t)|_{\Gamma_3} = 0$ išplaukia iš bendrojo atvejo, kai normalioji įtempių komponentė lygi nuliui:

$$\Big(-pI + \mu_f (\nabla \mathbf{v} + (\nabla \mathbf{v})^T) \mathbf{n} \Big) \cdot \mathbf{n} = 0.$$

Laikydami, kad $\text{div}\mathbf{v} = 0$ ir kai $\mathbf{v}_\tau = 0$, gauname, kad $p = 0$ ant Γ_3.

Krašto ∂G dalis Γ_1 yra tarp skysčio tekėjimo srities ir sienelės. Sienelės judėjimas aprašomas netiesinėmis elastingumo lygtimis esant nežinomam poslinkiui $\mathbf{u}(x,t)$, $x \in G_d$:

$$\rho \frac{\partial^2 \mathbf{u}}{\partial t^2}(x,t) - \nabla \cdot (J\sigma \boldsymbol{F}^{-T})^T = 0, \tag{S.13}$$

čia $\rho > 0$ - sienelės medžiagos tankis, $\mathbf{F} = I + \nabla \mathbf{u}$ - deformacijos gradientas, $J\sigma \boldsymbol{F}^{-T}$ yra 1-asis Piola ir Kirchofo įtempis, $J = \det \boldsymbol{F}$ Jakobiano determinantas, σ_{ij} įtempių tenzorius tenkinantis tiesinį Huko dėsnį (žr. [68]):

$$\sigma_{ij} = \lambda \sum_{k=1}^{3} \varepsilon_{kk}\delta_{ij} + 2\mu\varepsilon_{ij}, \tag{S.14}$$

čia λ ir μ yra Lamė parametrai, o δ_{ij} - Kronekerio delta:

$$\delta_{ij} = \begin{cases} 0 & \text{if } \ i \neq j \\ 1 & \text{if } \ i = j, \end{cases}$$

ir

$$\varepsilon_{ij} = \frac{1}{2}\Big(\frac{\partial u_i}{\partial x_j} + \frac{\partial u_j}{\partial x_i} + \sum_{k=1}^{3} \frac{\partial u_k}{\partial x_i}\frac{\partial u_k}{\partial x_j}\Big)$$

yra deformacijos tenzorius. Tuomet linearizuodami gausime

$$\varepsilon_{ij} = \frac{1}{2}\Big(\frac{\partial u_i}{\partial x_j} + \frac{\partial u_j}{\partial x_i}\Big),$$

Lamė parametrus galime išreikšti per Jungo modulį E ir Puasono santykį ν, $E > 0,\ -1 < \nu < 1/2$:

$$\lambda = \frac{E\nu}{(1+\nu)(1-2\nu)}, \quad \mu = \frac{E}{2(1+\nu)}. \tag{S.15}$$

Šiai sistemai reikalingos dvi pradinės sąlygos $\mathbf{u}$:

$$\mathbf{u}(x,0) = 0, \quad \frac{\partial \mathbf{u}}{\partial t}(x,0) = 0, \quad x \in G_d, \tag{S.16}$$

kraštinės salygos ant $\partial G_d \backslash (\Gamma_1 \cup \Gamma_{1,d})$ (užspausti galai):

$$\mathbf{u}(x,t) = 0, \quad x \in \partial G_d \backslash (\Gamma_1 \cup \Gamma_{1,d}), \tag{S.17}$$

kraštinės sąlygos ant $\Gamma_{1,d}$ (taikomas slėgis $p_{\text{wall}}(t)$ vaizduojantis sienelės susitraukimus pavaizduotas 4 pav.):

$$(J\sigma \boldsymbol{F}^{-T})^T \mathbf{n} = -p_{\text{wall}}(t)\mathbf{n}, \quad x \in \Gamma_{1,d}, \tag{S.18}$$

ir galiausiai sujungimo sąlygos ant judančio krašto Γ_1:
greičio tolydumas:

$$\mathbf{v}(x + \mathbf{u}(x,t), t) = \frac{\partial \mathbf{u}}{\partial t}(x,t), \quad x \in \Gamma_1, \tag{S.19}$$

ir įtempių tolydumas:

$$-(J\sigma \boldsymbol{F}^{-T})^T \mathbf{n} = (-pI + \mu_f(\nabla \mathbf{v} + (\nabla \mathbf{v})^T))\mathbf{n}, \quad x \in \Gamma_1, \tag{S.20}$$

u yra išorinė G normalė. Dešiniąją (S.20) pusę galime pakeisti $-p\mathbf{n}$.

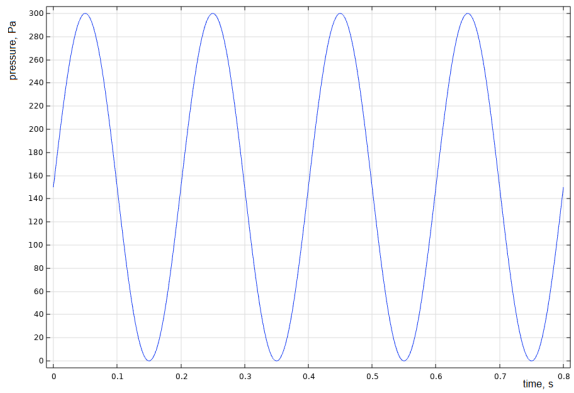

4 pav. – Slėgis $p_{\text{wall}}(t)$ ant kevalo esant prieširdžių virpėjimui.

Modeliui pritaikyti parametrai: $d = 2.5 \cdot 10^{-3}$ m , $\rho_f = \rho = 1050$ kg/m^3, $\mu_f = 3.5 \cdot 10^{-3}$ Pa$\cdot$s, $\nu = 0.47$, E yra intervale $[4 \cdot 10^4, 8 \cdot 10^5]$ Pa. Jungo modulis priklauso nuo laiko, t.y. $p_{\text{wall}}(t)$:

$$E(t) = 4 \cdot 10^4 + p_{\text{wall}}(t)(8 \cdot 10^5 - 4 \cdot 10^4)/\max p_{\text{wall}},$$

kadangi širdies raumuo (miokardas) kietėja periodiškai.

Šiam uždaviniui išspręsti skaitiniais metodais takome COMSOL programą. Plonas sluoksnis G_d buvo aproksimuojamas naudojantis Ufliando ir Mindlino kevalo modeliu, kuriame poslinkio vektorius **u** užrašomas pavidalu

$$\mathbf{u}(\tilde{x}_1, \tilde{x}_2, \tilde{x}_3, t) = \boldsymbol{\eta}(\tilde{x}_1, \tilde{x}_2, t) + \tilde{x}_3 \boldsymbol{\zeta}(\tilde{x}_1, \tilde{x}_2, t), \tag{S.21}$$

čia $\tilde{x}_1$ ir $\tilde{x}_2$ yra plokštumos lokaliosios kevalo koordinatės, $\tilde{x}_3 \in [-d/2, d/2]$ yra normalioji koordinatė, lygi nuliui paviršiaus viduryje $\Gamma_{1,d/2}$ (esančiu atstumu $d/2$ nuo Γ_1 ir nuo $\Gamma_{1,d}$, žr. 5 pav.).

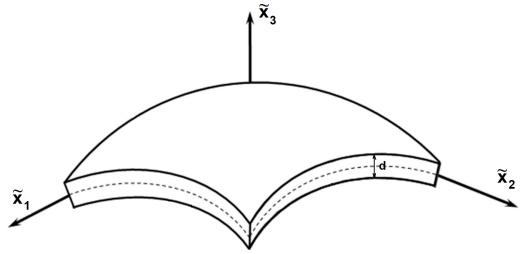

5 pav. – Kevalo lokaliosios koordinatės

Tegul $\boldsymbol{\eta}(\tilde{x}_1,\tilde{x}_2,t)$ yra kevalo poslinkio vektorius, o $\boldsymbol{\zeta}(\tilde{x}_1,\tilde{x}_2,t)$ - kevalo normalės kampinio poslinkio vektorius ($\boldsymbol{\zeta}\cdot\mathbf{n}=0$). Toliau, kevalo lygčių teorijoje $\Gamma_{1,d/2}$ pakeičiamas (aproksimuojamas) Γ_1.

Tuomet pirmoji (greičio tolydumo) salyga užrašoma pavidalu:

$$\mathbf{v}(x+\boldsymbol{\eta}(\tilde{x}_1,\tilde{x}_2,t),t)=\frac{\partial\boldsymbol{\eta}}{\partial t}(\tilde{x}_1,\tilde{x}_2,t),$$

Antroji sąlygą sieja nežinomąsias funkcijas $\boldsymbol{\eta},\boldsymbol{\zeta}$ ir slėgį p lygčių sistema, aprašančia kevalo judėjimą. Ši sistema sudaroma iš dviejų lygčių, kuriose $\boldsymbol{\eta},\boldsymbol{\zeta}$ antrosios eilės išvestinės laiko atžvilgiu yra kairėje pusėje (žr. (S.22)). Taške $\tilde{x}$ ant krašto Γ_1 šioms lygtims gauti išskleiskime $\nabla\cdot((J\sigma\boldsymbol{F}^{-T})^T)$ pakeisdami $\mathbf{u}(\tilde{x}_1,\tilde{x}_2,\tilde{x}_3,t)$ suma (S.21) pirmosios eilės Teiloro formule (pagal normalųjį kintamąjį $\tilde{x}_3$):

$$\nabla\cdot((J\sigma\boldsymbol{F}^{-T})^T)=\boldsymbol{\Phi}[\boldsymbol{\eta},\boldsymbol{\zeta}](\tilde{x}_1,\tilde{x}_2,t)+\tilde{x}_3\boldsymbol{\Psi}[\boldsymbol{\eta},\boldsymbol{\zeta}](\tilde{x}_1,\tilde{x}_2,t)+o(\tilde{x}_3),$$

čia $\boldsymbol{\Phi}[\boldsymbol{\eta},\boldsymbol{\zeta}],\boldsymbol{\Psi}[\boldsymbol{\eta},\boldsymbol{\zeta}]$ yra išraiškos, sudarytos iš funkcijų $\boldsymbol{\eta},\boldsymbol{\zeta}$ ir jų pirmosios ir antrosios eilės išvestinių erdvės atžvilgiu. Tuomet antrąją sąlygą galime užrašyti pavidalu:

$$\begin{cases}\rho\dfrac{\partial^2\boldsymbol{\eta}}{\partial t^2}(\tilde{x}_1,\tilde{x}_2,t)=\boldsymbol{\Phi}[\boldsymbol{\eta},\boldsymbol{\zeta}](\tilde{x}_1,\tilde{x}_2,t)+d^{-1}(-p_{\text{wall}}+p)\mathbf{n},\\ \rho\dfrac{\partial^2\boldsymbol{\zeta}}{\partial t^2}(\tilde{x}_1,\tilde{x}_2,t)=\boldsymbol{\Psi}[\boldsymbol{\eta},\boldsymbol{\zeta}](\tilde{x}_1,\tilde{x}_2,t).\end{cases}\tag{S.22}$$

Antroji sistemos lygtis atitinka momentų balansą.

Pradinės sąlygos kevalui:

$$\begin{gathered}\boldsymbol{\eta}(\tilde{x}_1,\tilde{x}_2,0)=0,\quad\frac{\partial\boldsymbol{\eta}}{\partial t}(\tilde{x}_1,\tilde{x}_2,0)=0,\quad\boldsymbol{\zeta}(\tilde{x}_1,\tilde{x}_2,0)=0,\\ \frac{\partial\boldsymbol{\zeta}}{\partial t}(\tilde{x}_1,\tilde{x}_2,0)=0,\quad\tilde{x}_1,\tilde{x}_2\in\Gamma_1.\end{gathered}\tag{S.23}$$

Parenkame kraštines sąlygas kevalui:

$$\boldsymbol{\eta}(\tilde{x}_1,\tilde{x}_2,t)=0,\quad\boldsymbol{\zeta}(\tilde{x}_1,\tilde{x}_2,t)=0,\quad\tilde{x}_1,\tilde{x}_2\in\partial\Gamma_2\tag{S.24}$$

$$\begin{gathered}\boldsymbol{\eta}(\tilde{x}_1,\tilde{x}_2,t)=0,\quad M_{nn}(\tilde{x}_1,\tilde{x}_2,t)=0,\\ M_{n\tau}(\tilde{x}_1,\tilde{x}_2,t)=0,\quad\tilde{x}_1,\tilde{x}_2\in\partial\Gamma_3,\end{gathered}\tag{S.25}$$

čia M_{nn} yra normalusis momentas ant Γ_3 krašto, o τ - tangentinė kryptis (pavyzdžiui, kai x_1 yra normalioji kryptis, tai $M_{11}(\tilde{x}_1, \tilde{x}_2, t) = 0, M_{21}(\tilde{x}_1, \tilde{x}_2, t) = 0$).

Momentai apibrėžiami formule $M = \int_{-d/2}^{d/2} \tilde{x}_3 J\sigma \boldsymbol{F}^{-T} \mathrm{d}\tilde{x}_3$ (pagrindinė Teiloro skleidinio dalis).

Svarbu pažymeti, kad tiesioginiai šio modelio COMSOL skaičiavimai blogai konverguoja. COMSOL kode naudojamos neišreikštinės skaitinės schemos, kuriose kiekviename laiko žingsnyje reikia spręsti didelę netiesinę lygčių sistemą. Skaičiuoklė remiasi Niutono metodu, kuris yra labai jautrus pradinės aproksimacijos pasirinkimui. Todėl mes sprendžiame FSI uždavinį dviem žingsniais: pirmajame žingsnyje sprendžiame Navjė ir Stokso sistemą (S.9) su nejudančia sienele, t.y. srityje G su pradine sąlyga (S.10) ir kraštinėmis sąlygomis (S.11) ant Γ_2 ir (S.12) ant Γ_3, kuomet kraštinės sąlygos ant Γ_1 pakeičiamos

$$\mathbf{v} = 0, \quad x \in \Gamma_1.$$

Konvergavimui gauti antrajame žingsnyje sprendžiamas FSI uždavinys naudojant pirmajame žingsnyje gautas pradines aproksimacijas.

Pritaikę aprašytą modelį ir apskaičiavę dviejų pacientų kraujo tekėjimo greičius kairiojo prieširdžio apendiksuose (žr. 6 pav.), matome, kad Paciento **A**, kurį ištiko insultas, kraujo tekėjimo greitis kairiojo prieširdžio apendikse yra mažesnis, negu neištikto insulto Paciento **B**, nors abiem pacientams buvo diagnozuotas prieširdžių virpėjimas.

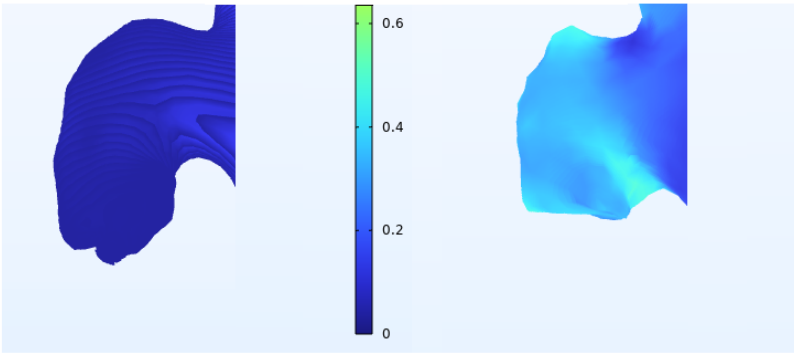

6 pav. – Pacientų **A** (kairėje) ir **B** (dešinėje) apskaičiuotas kraujo tekėjimo greitis kairiojo prieširdžio apendikse. Tamsiai mėlyna spalva atitinka mažą greitį, žydra - didelį greitį (skalėje nurodytas kraujo tekėjimo greičio modulis, m/s).

Išvados

Šioje disertacijoje buvo išnagrinėti trys uždaviniai:

I. Įrodytas laiko atžvilgiu periodinio Navjė ir Stokso uždavinio begalinia-me cilindre su užduotu srautu $F(t) \in L^2(0,T)$ sprendinio egzistavimas ir vienatis esant minimaliam duomenų reguliarumui.

II. FSI modelis supaprastintas iki ketvirtosios eilės diferencialinės lygties dalinėmis išvestinėmis. Atlikti kraujo tekėjimo greičio skaičiavimai cilindre ir Y-formos cilindrų tinkle taikant du būdus: Sudaromas pilnas FSI modelis (nestacionarioji Navjė ir Stokso lygčių sistema su judančia sienele) ir gauta supaprastinta diferencialinė lygtis dalinėmis išvestinėmis. Pastaroji reikalauja mažesnių resursų, o gaunami rezultatai skiriasi nereikšmingai.

III. Pristatytas FSI modelis, pritaikytas konkretaus paciento kraujo tekėjimo greičiui kairiajame prieširdyje apskaičiuoti. Modeliavimas įtraukia vaizdo generavimą, segmentaciją, valymą (triukšmų mažinimą), skaičiavimo srities sudarymą. Modelio validavimas pagrįstas palyginimu su Doplerio matavimais kairiojo prieširdžio apendikso ostiume. Išnagrinėta koreliacija tarp stagnacijos zonų (ne)buvimo ir insulto rizikos. COMSOL skaičiavimai, pritaikyti FSI modeliui, kelia iššūkių ir dažnai tiesioginis kodo taikymas neduoda konvergavimo. Paaiškinta, kad tokiu atveju skaičiavimai dviem žingsniais (su kietąja sienele pirmajame žingsnyje, ir FSI antrajame) suteikia modelio konvergavimą.

Nikolajus Kozulinas

Curriculum Vitae

ASMENINĖ INFORMACIJA

Telefono numeris	(370) 5-219-5017
El. pašto adresas	nikolajus.kozulinas@mif.vu.lt

IŠSILAVINIMAS

Matematikos doktorantūra 2019-2023

Vilniaus universitetas

Matematikos magistras 2017-2019

Vilniaus universitetas

Biochemijos bakalauras 2004-2009

Vilniaus universitetas

Vidurinis išsilavinimas 1993-2004

Vilniaus Naujamiesčio vidurinė mokykla

DARBO PATIRTIS

Jaunesnysis asistentas 2019-dabar

Vilniaus universitetas, Matematikos ir informatikos fakultetas

Jaunesnysis mokslo darbuotojas 2019-2023

Vilniaus universitetas, Matematikos ir informatikos fakultetas

Matematikos korepetitorius 2017-2020

Individuali veikla

Projektų vadovas 2016-2017

UAB Leddex

Pardavimų grupės vadovas 2010-2016

UAB Big Trans, UAB Eurasia Logistics

Transporto vadybininkas 2008-2010

UAB Big Trans, UAB Eurasia Logistics

ASMENINIAI GEBĖJIMAI

Kalbos	Anglų, Rusų - **C2**; Italų, Lenkų, Ukrainiečių - **B1**
IT gebėjimai	Microsoft Office, LaTeX, COMSOL Multiphysics

Publications by author

1. K. Kaulakytė, N. Kozulinas, K. Pileckas. Time-periodic Poiseuille-type solution with minimally regular flow rate. *Nonlinear Analysis: Modelling and Control*, **26**(5) (2021)
   https://doi.org/10.15388/namc.2021.26.24502
2. N. Kozulinas, G. Panasenko, K. Pileckas, V. Šumskas. Numerical study of the equation on the graph for the steady state non-Newtonian flow in thin tube structure. *Mathematical Modelling and Analysis*, **28**(4), 581–595 (2023)
   https://doi.org/10.3846/mma.2023.18311
3. K. Kaulakytė, N. Kozulinas, G. Panasenko, K. Pileckas, V. Šumskas. Poiseuille-Type Approximations for Axisymmetric Flow in a Thin Tube with Thin Stiff Elastic Wall. *Mathematics*, **11**(9), 2106 (2023)
   https://doi.org/10.3390/math11092106
4. A. V. Belyaev, A. Bouchnita, N. Kozulinas, G. Panasenko, V. Volpert. Multiphase Patient-specific Simulations to Study Fibrillation-induced Thrombosis in the Left Atrial Appendage. *Physics of Fluids*, **36**(7), 071912 (2024)
   https://doi.org/10.1063/5.0216196

Vilnius University Press
9 Saulėtekio Ave., Building III, LT - 10222 Vilnius
Email: info@leidykla.vu.lt, www.leidykla.vu.lt
bookshop.vu.lt, journals.vu.lt
Print run of 20 copies

Acknowledgment. The work has received funding from European Social Fund (project No 09.3.3-LMT-K-712-17-0003) under grant agreement with the Research Council of Lithuania (LMTLT).